# SYNTHESIS, CHARACTERIZATION, AND APPLICATION OF SILICA-BASED NANOPARTICULATE PLATFORMS FOR THE DELIVERY OF PHOTOSENSITIZERS IN THE USE OF PHOTODYNAMIC THERAPY FOR CANCER TREATMENT

by

Zachary K. Lyles

A dissertation submitted to the faculty of
University of North Carolina at Charlotte
in partial fulfillment of the requirements for
the degree of Doctor of Philosophy in
Nanoscale Science

Charlotte

2018

Approved By:

_____
Dr. Juan Vivero-Escoto

_____
Dr. Craig Ogle

_____
Dr. Michael Walter

_____
Dr. Nathaniel Fried

_____
Dr. Tom Schmedake

# ABSTRACT

ZACHARY K. LYLES

Synthesis, characterization, and application of silica-based nanoparticulate platforms for the delivery of photosensitizers in the use of photodynamic therapy for cancer treatment

(Under the direction of Dr. JUAN VIVERO-ESCOTO)

Triple negative breast cancer (TNBC) is a subtype of breast cancer which lacks expressions of hormonal receptors (ER/PR/HER2) and other meaningful targets. TNBC is characterized by intra-tumoral heterogeneities, high proliferative activity, poor prognosis, aggressive relapse, and distant metastasis to lungs and brain, making the disease clinically challenging to treat. Approximately 50% of the patients diagnosed with early-stage TNBC experience recurrence and 37% die within the first 5 years after surgery. Due to the aggressive nature of TNBC, novel therapeutic alternatives are of interest to improve clinical outcome of this deadly disease. Photodynamic therapy (PDT) is a promising non-toxic, minimally invasive light-based therapy which causes cell death and triggers anti-tumor immune response. Photodynamic therapy (PDT) combats many negative side effects associated with more commonly used treatments such as chemotherapy and radiation therapy. PDT provides benefits, as it is minimally invasive, produces minor damage to healthy tissue, and does not require long therapeutic follow-ups, making it a patient-friendly therapeutic modality. This Ph.D. thesis is aimed to develop and evaluate the phototherapeutic effects of three independent strategies for the treatment of highly aggressive TNBC; 1) a novel redox-responsive polysilsesquioxane-based nanoparticle system for the delivery of photosensitizer (PS) protoporphyrin IX (PpIX) (PpIX-PSilQ NPs), 2) Mesoporous silica nanoparticle-based PDT platform for the combinatorial delivery of PS chlorin e6 and chemotherapy agent cisplatin, Ce6-cisPt-

MSN, 3) PpIX-PSilQ NPs based platform for the delivery of PpIX, a multitargeting agent (curcumin) and siRNA. Each of the nanoplatforms were synthesized, characterized and their phototherapeutic properties were evaluated in TNBC cell lines and *in vivo* orthotopic TNBC models.

## ACKNOWLEDGEMENTS

It is said that “it takes a village to raise a child”, it takes a lot more than a village to raise a PhD student. I would never have been in this position if it wasn’t for the support of my family and friends. After 10 years I am concluding my time at UNCC. When you have been in a place this long and worked this much, the people you work with become your friends, and those friends become your family. Thank you to everyone who has helped make this possible.

Table of Contents

List of Figures

# List of Tables

# List of Abbreviations

µg: microgram

µL: microliter

µm: micrometer

$^1O_2$ : Singlet oxygen

AAS: Atomic absorption spectroscopy

ADPA: 9,10-anthracene dipropionic acid

ALA: 5-aminolevulinic acid

AOT: Aerosol OT

APTES: (3-aminopropyl) trihydroxysilane

ATCC: American Type culture collection

BC: Breast cancer

BMA: Brust-Mucin antigen

bPS: biotinylated photosensitizer

Ce6: Chlorin e6

cisPt: cisplatin

CLSM: Confocal laser scanning microscopy

cm: centimeter

CTAB: Hexadecyltrimethylammoinum bromide

Cur: Curcumin

DCF-DA: 2',7'-dichlorodihydrofluorescein diacetate

DCM: Dichloromethane

Dh: hydrodynamic diameter

DIPEA: di-isopropyl ethyl amine

DLS: Dynamic light scattering

DMF: Dimethyl formamide

DMSO: Dimethysulfoxide

DPBF: 1,3-diphenylisobenzofuran

DPDS: 2,2'-dipyridyldisulfide

DTT: Dithiothreitol

EDC: 1-ethyl-3-(3-dimethylaminopropyl) carbodiimide

EDTA: Ethylene diamine tetra acetic acid

EPR: Enhanced permeability and retention effect

ER: Endoplasmic reticulum

ER: Estrogen receptor

FACS: Fluorescence-activated cell sorting

FBS: Fetal bovine serum

FITC:

FRET: Förster resonance energy transfer

g: gram

GFP: Green fluorescence protein

GSH: Glutathione

H&E: Hematoxylin and eosin

HER2: Human epidermal growth factor 2

Hp: Hematoporphyrin

IC50: 50 % inhibitory concentration

ICP-MS: Inductively coupled plasma Mass spectrometry

IR: Infrared

L: liter

LED:

M: molar

mAbs: Monoclonal antibodies

mg: milligram

mL: milliliter

mm: millimeter

mM: millimolar

MO: molecular orbital

mPEG: methoxy poly(ethylene) glycol

MPS: Mononuclear phagocyte system

MPTES: mercaptopropyltriethoxysilane

MSN: Mesoporous silica nanoparticles

mW: milliwatt

MW: Molecular weight

NaOH: sodium hydroxide

NEAA: Non-essential amino acids

ng: nanogram

NHS: N-hydroxysuccinimide

NIR: Near infrared

nm: nanometer

nM: nanomolar

NPe6: mono-N-aspartyl chlorin e6

NPs: Nanoparticles

NSG: NOD SCID gamma

ORMOSIL: Organically modified silica

PANAM: polyamidoamine

PBS: phosphate buffer solution

PCI: Photochemical internalization

PDT: Photodynamic therapy

PEG: Poly(ethylene) glycol

PEI: Polyethylene imine

pg: picogram

PLGA: poly(lactic-co-glycolic acid)

PNps: Polymeric nanoparticles

PpIX: Protoporphyrin IX

PpIX-Cys: protoporphyrin IX-cysteine

PpIX-SE: protoporphyrin IX succinimide ester

PR: Progesterone receptor

PS: photosensitizer

PSilQ: polysilsesquioxane

PTT: Photothermal therapy

r.o: retro orbital

ROS: reactive oxygen species

SEM: Scanning electron microscopy

siRNA: small interfering ribonucleic acid

SOSG: Singlet oxygen sensor green

t1/2: half-life

TEA: Triethylamine

TEM: Transmission electron microscopy

TEOS: Tetraethyl orthosilicate

TESPIC: triethoxysilylpropylisocyanate

TGA: thermogravimetric analysis

THF: Tetrahydrofuran

TNBC: Triple negative breast cancer

TOAB: tetraocylammonium bromide

TX 100: 1% triton X 100

UCNPs: Up-conversion nanoparticles

UHPLC: ultra-high performance liquid chromatography

UV-vis: Ultra-violet visible spectroscopy

L2K: Lipofectamine

# CHAPTER 1
# INTRODUCTION

## 1.1. Cancer is a major epidemic of the 21st century.

Cancer is a major health problem worldwide and is the second largest cause of death in the United States. In 2018, there are an estimated 1.7 million new cancer cases diagnosed and 609,640 deaths in the US, which translates to 1,670 deaths per day.[1] Cancer is a group of diseases characterized by uncontrolled growth and spread of abnormal cells. Current options for the management of cancer are surgical removal of tumors, chemotherapy, radiotherapy or a combination of them. These treatment options suffer from disadvantages like toxic effects to healthy organs, as well as development of resistance to chemotherapeutic agents and radiation.

### *1.1.1. Triple Negative Breast Cancer (TNBC).*

Breast cancer (BC) is the most frequently diagnosed cancer in women and remains one of the leading causes of cancer-related mortality of women in the United States. Despite tremendous advances in diagnosis and treatment, there has been a sharp increase in the BC incidence and mortality in recent years. In 2018, the American Cancer Society estimates that 268,670 new cases of BC will be diagnosed for both women (266,120) and men (2,550), with an estimated deaths of 41,400 women and 480 men.[2] Currently, BC is divided into subtypes based on the molecular heterogeneity: estrogen/progesterone receptor, HER2 receptor, luminal A, luminal B and triple negative breast cancer (TNBC). These receptors serve as markers for diagnosis and targets for hormonal therapies.[3] TNBC subtype is characterized by the lack of these receptors, which

accounts for about 10-20% of the newly diagnosed cases and is more prevalent in younger women (<40 years) and women of African and Hispanic descent.[4,5] Overall, TNBC is characterized by intra-tumoral heterogeneities, high proliferative activity, poor prognosis, high risk of relapse, and metastasis to lungs and brain.[6] Approximately 50% of the patients diagnosed with early-stage TNBC experience recurrence and 37% die within the first 5 years after surgery.[5] Moreover, patients with metastatic TNBC have high frequency of progression and low overall survival.[7,8] As TNBC lack targetable receptors, patients with TNBC are treated with conventional chemotherapy and radiotherapy, which are associated with toxic side effects and development of resistance leading to aggressive relapse and distant metastasis.[9]

***1.1.2. Challenges associated with current therapeutic options of TNBC.***

Challenges in managing TNBC patients clinically are extensive, such as the inter/intra-tumoral heterogeneities, resistance to systemic therapies, high frequency of progression, distant metastasis, and lethal relapse.[7,10] Treatment methods for TNBC currently consists of surgery, chemotherapy and radiation therapy that are associated with negative side effects such as tissue mutilation, nausea, violent vomiting, and long-term neuropsychological impacts.[11,12] Though most tumors initially respond to chemotherapeutics, often they become refractory resulting in relapsed tumors, which are typically resistant and more aggressive. In addition, distant recurrences are more common than local recurrences, further leading to metastatic disease associated with much lower survival.[8,10,13] TNBC patients treated with chemotherapy exhibit poor outcomes with only 30-45% achieving a complete response and relapse occurs usually within 3-5 years of

diagnosis.[10] Though multidrug combinations are beneficial compared to single agents, they are often accompanied with high toxicity profiles. These dismal outcomes show the ever-growing need for exploring new therapeutic technologies to treat TNBC and allow more options for the patients.

Non-traditional approaches such as photodynamic therapy (PDT) and photothermal therapy (PTT) are being evaluated as promising options for TNBC.[14] PDT is a non-toxic, minimally invasive light-based therapy which is currently approved for the treatment of numerous human malignancies including lung, esophageal, head and neck, and cervical cancers.[14–16] PDT combats many of the negative side effects that occur with more commonly used treatments such as chemotherapy and radiation therapy.[15,17,18] Additional evidence suggests that PDT induces an immune response creating immune memory which works towards destruction of metastases distant from the treated sites and against recurrence.[14,19] PDT provides advantages compared to other therapies such as it is minimally invasive, it produces minor damage to the healthy tissue, and it does not require long therapeutic follow-ups, making it a patient-friendly therapeutic modality.[20,21] Currently in clinic, PDT is generally applied as an adjuvant therapy to kill residual tumor cells after surgery in solid tumors as well as before surgery to shrink the tumors.[22–24] In the case of breast cancer, the first clinical application for PDT was in the treatment of skin metastases in chest wall recurrence.[21,25]

## 1.2. Basic principles of Photodynamic Therapy.

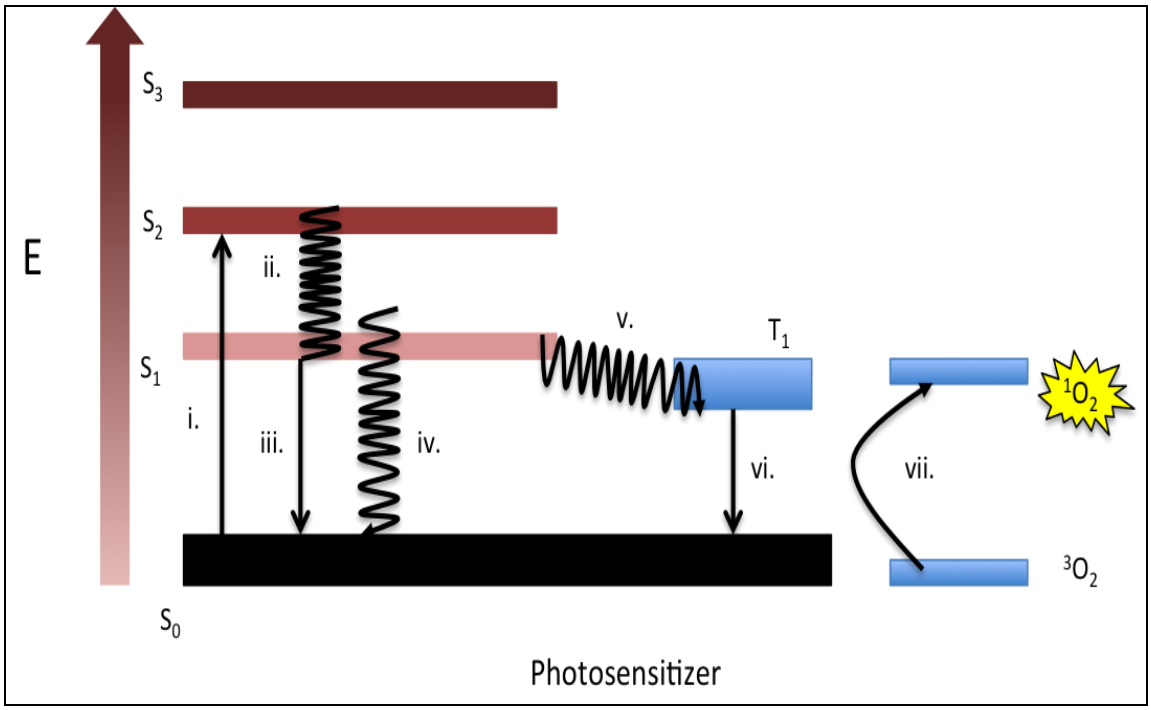


*Figure 1. Jablonski diagram shows the excitation of the electron from light source to the singlet oxygen. Light absorption and excitation (i), internal conversion (ii), fluorescence of energy (iii), radiation-less transitions (iv), intersystem transition (v), phosphorescence (vi), energy transfer to create ROS (vii).*[15]

PDT uses the combination of three components, light, oxygen, and a photosensitizer (PS), to cause cell death. For the ideal treatment using PDT, a photosensitizer is administered in the body and will passively accumulate in tumor tissue. When the tumor tissue is irradiated with light to specific wavelength, and the photosensitizer will absorb light and an electron is excited from the valence band to the conduction band (Figure 1(i)). Once in the excited state the energy can undergo different transitions: 1) A photon can be produced during relaxation back to the ground state (Figure 1(iii)), which would be observed as fluorescence; 2) the energy can be released

through vibrational energy (phonon) (Figure 1(iv)) called radiation-less transition (heat), and 3) the energy can be transferred from a singly degenerate state to a triplet degenerated state through intersystem crossing (Figure 1(v)).[15,18,26]

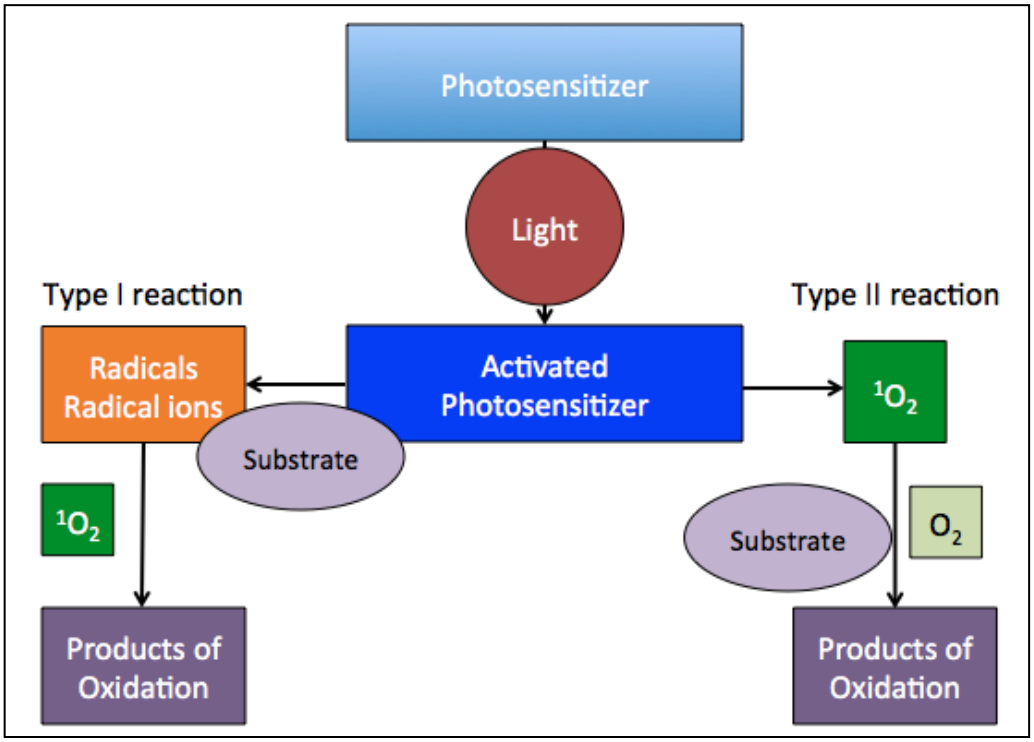


*Figure 2. There are two types of reactions in PDT. As the PS absorbs light it becomes activated and can undergo either type of the reactions. The activated PS can react directly with a substrate (Type I Reaction) transferring the energy to a cell membrane, or molecule, directly forming radicals. The other possibility is that the PS transfers its energy directly to oxygen (Type II Reaction), which will oxidize the surrounding substrates.*

Once in the triplet excited state, there are two relaxation modes that can occur: [18,27] 1) the energy can be released through the release of a photon (Figure 1(vi)), which is observed as phosphorescence and 2) the energy transfer can occur through a type I or type II interaction with oxygen (Figure 1(vii), Figure 2).[27,28] Type I energy release occurs when the triplet excited state transfers its energy to directly produce reactive oxygen

species (ROS). Type I is not commonly found in PDT but is the way singlet oxygen is produced in photodynamic inactivation (PDI) (Figure 2). Type II energy transfer occurs when the energy is transferred from the triplet-excited state of the PS to an oxygen molecule.

### *1.2.1. Light.*

Current methods of light administration in PDT are performed using lasers, which are delivered through fiber optics, and occasionally through filtered lamps for superficial lesions.[27,29] Lasers afford wavelength specificity, as well as high intensity photons focused in one area. Light penetration remains one of the largest limitations for PDT.[16,30] Human tissue absorbs, reflects, and scatters light leading to penetration problems. Pigment rich tissue is, therefore, less suitable for PDT as the light penetration will be diminished even further as it is absorbed by the tissue upon irradiation. Longer wavelength light (600-750 nm) is commonly used, as it tends to penetrate deep tissue.[27,28] However, the light is still only able to penetrate a few hundred micrometers into skin.[31] Infrared (IR) wavelengths (750-1400 nm) are capable of penetrating further into the skin but do not carry sufficient energy to excite a PS in an efficient manner. The penetration depth of light is one of the main reasons for limited application of PDT as the primary treatment. Light fluence and fluence rate are also very important aspects of PDT.[27,28,32,33] Light fluence deals with the power density of light as it is measured in energy per unit area ($J/cm^2$). Fluence rate is the energy irradiated per rate of time in a specific area ($W/cm^2$).[33] Fluence rate is usually increased to the maximum possible value to decrease

the time of irradiation. The drawback of increased fluence rate is depletion of oxygen, which further limits the efficiency of PDT.

### *1.2.2. Oxygen.*

Oxygen is a key component for the PDT process. Singlet oxygen ($^1O_2$) and ROS are the active cell killing agents.[34–36] Oxygen receives the energy directly from the PS, that forms singlet oxygen, which can then produce ROS. The singlet oxygen is more reactive than triplet oxygen and can be explained by molecular orbital theory (MO). Two states of singlet oxygen can be produced, see molecular orbitals A and B in Figure 3. Molecular orbital A (MO-A) is significantly less stable than MO-B, and both forms are less stable compared to triplet oxygen (MO-C).[35,36]

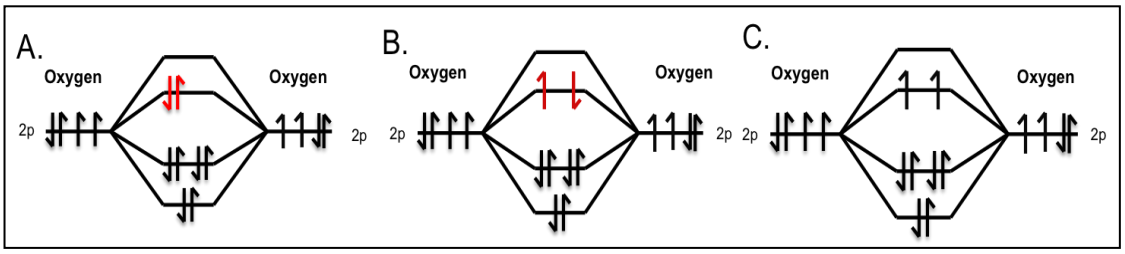


*Figure 3. The three molecular orbitals for oxygen are shown. A and B are the two MO diagrams for singlet oxygen. A is the least stable form of singlet oxygen and will quickly separate the two electrons to each occupy an orbital in opposite spin, B, which is the common form of singlet oxygen found in PDT. The stable form of molecular oxygen, the triplet state, is shown on the right, C.*[36]

The reactivity of singlet oxygen also leads to the specificity of PDT.[15,30] Singlet oxygen has highly unstable energy which leads to rapid interaction with its surroundings and energy release (1-3 μs). This short time does not allow for singlet oxygen to transfer from one cell to another. Singlet oxygen has been shown to only travel a distance of 45

nm inside the cellular cytoplasm. Considering eukaryotic cells are in the range of 1-100 μm, singlet oxygen will stay inside of the cell, not affecting the cells around it.[15,34]

### *1.2.3. Photosensitizers.*

Photosensitizers (PSs) are one of the most important aspects of PDT. PSs are synthetically tuned to have particular biological and photophysical features, such as low dark toxicity, and long wavelength absorption. Moreover, PS agents should to be able to absorb light efficiently at the longer wavelengths in the red or IR region of the electromagnetic spectrum. Despite development of many PSs, very few PSs have entered clinical trials due to lack of selectivity to the target tissue as compared to healthy tissue, low extinction coefficients, and accumulation in the skin leading to prolonged light sensitivity.[15,30]

Below is the list of ideal properties for an efficient photosensitizer agent:[15,16,30]

- Stable chemical composition
- Easy synthesis
- Minimal self-aggregation
- No dark toxicity
- Photostability
- Long wavelength absorption
- Target specificity
- Rapid clearance from the body

## 1.3. Development of Photosensitizers.

Hermann von Tappeiner first introduced the concept of PDT in 1903. A student of von Tappeiner, Oscar Raab, noticed that using certain synthetic dyes with the combination of light produced a toxic effect on skin tissue.[15] Von Tappeiner then coined the term "photodynamic action" when he put a therapeutic protocol together with a dye, light, and oxygen. The development of PSs through history can be divided into three different generations.[16]

### *1.3.1. 1st Generation Photosensitizers.*

Hematoporphyrin (Hp) was the first PS discovered in 1816 (Figure 4). However, the photophysical properties of Hp were not fully characterized for 25 years.[15,37,38] One major issue with Hp is the large dose requirement to reach a therapeutic effect, which is caused by a decrease in its absorption once inside the cell. In 1955, it was discovered that there were multiple components to Hp all of which showed decreased localization in tumor cells. This led researchers to investigate on new versions of Hp, hematoporphyrin derivatives (HpD), which allowed for increased cellular uptake. Researchers have shown that HpD is successful in treating breast, colon, prostate, and melanoma cancer.[15,39,40]

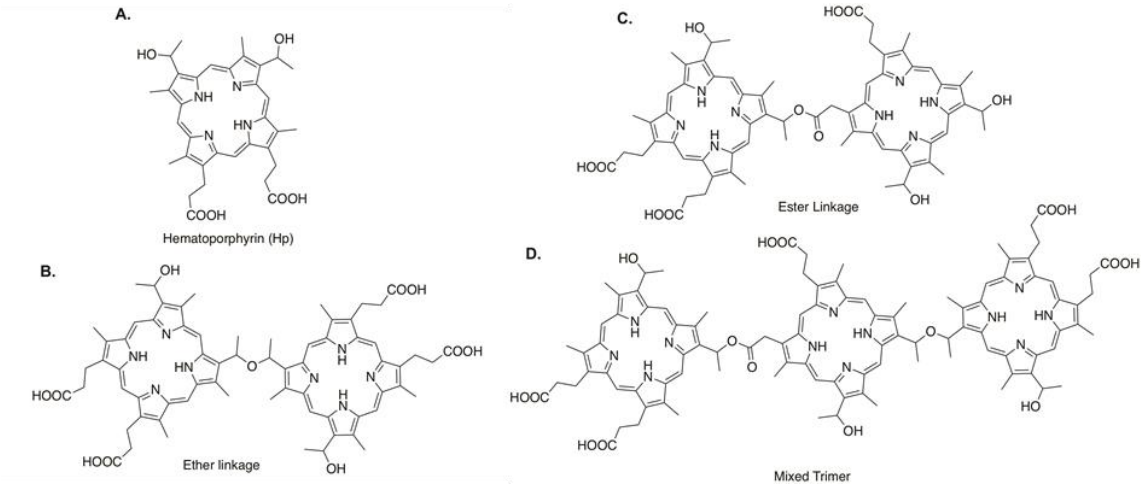


*Figure 4. A. Hematoporphyrin was the first PS discovered. B-D. The three primary components of Hp that have been isolated and used as the more effective HpD.*

HpD was further improved through purification, resulting in a PS formulation with increased efficacy called Photofrin.[15] Despite the improvements, Photofrin still has a low molar absorption coefficient, which reduces the phototherapeutic efficacy. Photofrin is biologically compatible; however, its half-life in the body of approximately 19 days which causes prolonged photosensitivity in the patients. Although Photofrin produces ROS efficiently to afford cell death in tumor tissue, it is still far from ideal when it comes to the desired features of a PS agent listed above. Photofrin is a mixture of monomers and oligomers of porphyrin derivatives. Purification techniques have shown that Photofrin has over 60 different components and there is no single active agent[15,41,42]. Photofrin has several limitations such as lack of selectivity for tumor tissue at normal dosing concentrations, prolonged photosensitivity, and purity.[15,18,30] These limitations led investigators to design second generation PSs.

### *1.3.2. 2nd Generation Photosensitizers.*

Scientists have explored the synthesis of other PSs to overcome some of the limitations observed with Photofrin. Due to the tunability of their photophysical properties porphyrins and porphyrin derivatives, such as Tookad, Levulan, and Chlorin e6 have been investigated as promising 2nd generation PSs (Figure 5). 2nd generation PSs are synthetically tuned through modification of the electronic structure of these molecules. Porphyrins, for example, can be reduced at one β-pyrrole position (structure of a chlorin) which increases red light absorption.[43] Porphyrins can also take advantage of the heavy atom effect, which utilizes high atomic number atoms to increase the efficiency of intersystem crossing and increase $^1O_2$ production.[44,45]

Tookad is a palladium centered porphyrin derivative[16,30] (Figure 5A), which has a high molar absorption coefficient, specifically in the near infrared (NIR) region of the spectrum.[15] The absorption in the NIR region affords deeper penetration of light and therefore allowing the treatment of deep tissue tumors as compared to 1st generation PSs (~4 mm as compared to ~1.5 mm).[15] Tookad is also quickly cleared from the circulatory system, having shown to be cleared from mice in 15 minutes. Quick clearance prevents accumulation in healthy tissue, which is a primary cause of dark toxicity and prolonged sensitivity to light. Tookad primarily targets the vasculature of tumor tissue causing both apoptotic and necrotic cell death. *In vivo* studies have shown that Tookad is quickly excreted from the human body after 2 hours.

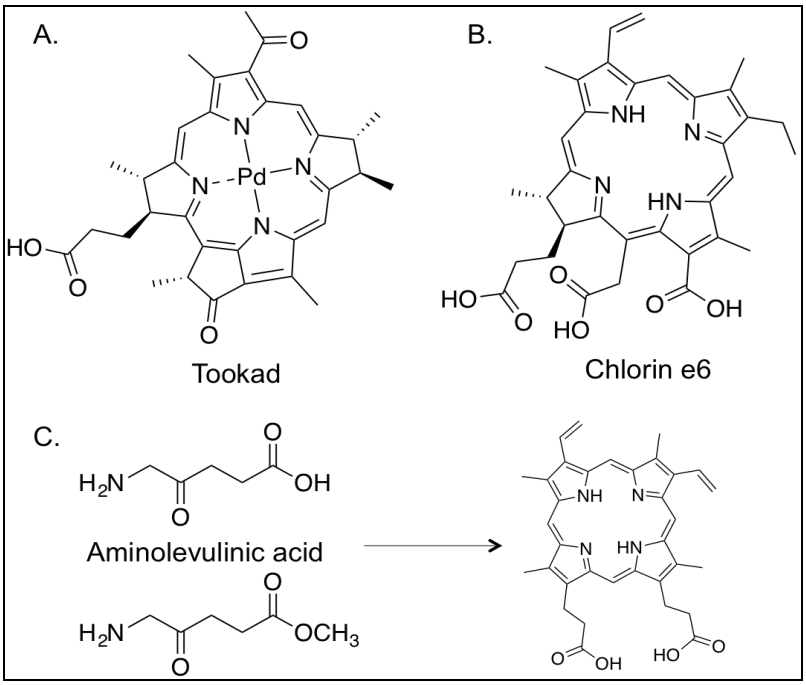


*Figure 5. Second generation photosensitizers are designed to increase the light absorption in longer wavelengths (550-700 nm). A. Tookad is a palladium centered pheophorbide porphyrin derivative. B. Chlorin e6 is a porphyrin derivative. Aspartyl residues are commonly added to increase hydrophilicity. C. Aminolevulinic acid (Levulan) is an amino acid that is metabolized to afford protoporphyrin IX (PpIX) inside cells. When PpIX is produced faster than it is converted to Heme it will be toxic when irradiated.*[15]

Levulan, which is the amino acid known as 5-aminolevulinic acid (ALA), is another example of second-generation PS. Once inside the cell, ALA is metabolized to protoporphyrin IX (PpIX), which can be later transformed into hemoglobin. PpIX is produced by the body naturally but is quickly turned into heme for hemoglobin. ALA causes an overproduction of PpIX that is used to kill the cells after light irradiation.[15] Interestingly, there is a further increase of PpIX (2-10x) with inoculation of ALA in cancer cells as compared to normal cells inoculated with ALA. In clinical applications, PpIX is commonly irradiated in the red wavelengths (620-640 nm) to enhance the light penetration depth. In the case of Levulan, there is normally 1-8 h window of waiting time

after its administration before light irradiation, which allows for maximum PpIX production and accumulation. PpIX is usually cleared in 24-48 h after administration. The first Levulan treatment for cancer was performed over 25 years ago with nearly 90% success, sparking the interest in this form of PS.[15,42,46] Currently, Levulan is primarily used to treat skin cancer through topical administration. Several studies have shown that administering Levulan in the presence of dimethylsulfoxide (DMSO) and ethylene diamine tetra acetic acid (EDTA) exhibits an increased efficacy.[15] The major drawback of Levulan is the decreased skin penetration depth to cause the overproduction of PpIX.[15]

Chlorins differ from porphyrins by the reduction of one β-pyrrole position on the tetra pyrrolic ring. This changes the symmetry, saddling the porphyrin and allowing for greater absorption in longer wavelengths (630-670 nm).[47] Chlorin e6 (Ce6) is considered a second-generation photosensitizer. Ce6 is chemically conjugated with an aspartyl residue to increase hydrophilicity (NPe6) and is administered following purification of the chlorin.[15,30] NPe6 has shown an optimal effect after irradiation at 2-4 h post administration with almost no phototoxicity after 12 h post administration. NPe6 is a promising 2$^{nd}$ generation PS that has undergone Phase III clinical trials for hepatocellular carcinoma.[15,42]

### *1.3.3. 3$^{rd}$ Generation Photosensitizers.*

3$^{rd}$ generation PSs are designed to increase both the circulation time and accumulation in target tissue compared to the 2$^{nd}$ generation PSs.[15,16,26,30,37] They can also undergo two photon up conversion. Monoclonal antibodies (mAbs) can be used to take advantage of the different surface antigens that are expressed on cancer cells. One

example of this active targeting is the use of the avidin-biotin binding to target labeled cancer cells. Wöhle et al. conjugated biotin to a zinc phthalocyanine through a reaction involving sulfochloride groups on the PS and biotin cadaverin.[48] Once the biotinylated PS (bPS) was purified, the phototoxicity was studied on an avidin tagged cell line (T47D with Brust-Mucin antigen (BMA)) and without avidin (SW 122 without BMA). The bPS showed a decrease in viability by 90% in the T47D cell line after irradiation with light at 5 J/cm$^2$, and 45% decrease in viability in the SW 122 cell line.[48] The increased phototoxicity shows a proof of concept for increasing localization of PSs using mAbs.

***1.3.4. Limitations of Photosensitizers.***

PSs are generally hydrophobic molecules which limits their solubility and causes aggregation in physiological conditions. Aggregation can result in fast excretion from the blood stream, which limits the circulation of PS and their accumulation in the tumor tissue. PSs also have a limited targeting ability. Once administered the PSs will disperse and accumulate in tissue throughout the whole body as opposed to the localized area of the tumor. To have the most effective treatment, a high concentration of PSs is desired in the tumor tissue. These limitations have led to the need of using nanoparticle delivery vehicles for PSs.

**1.4. Nanoparticles are promising PSs delivery systems to improve PDT.**

One of the main issues of PDT is the decreased accumulation of PSs at the optimal concentration and in the target tissue. Nanoparticles (NPs) present attractive features to be used as PS delivery vehicles.[49–54] NPs can encapsulate hydrophobic molecules to improve their pharmacokinetics and bioavailability. They are also able to

accumulate in tumor tissue both passively and actively, protect the payload of the PSs while traveling through the body, and can be synthesized to have a triggered release to increase localization.[52,55,56] Passive targeting is the process of NPs accumulation in cancer tissue without any added moiety to increase localization. The ability of NPs to passively accumulate in cancer tissue is called the enhanced permeability and retention effect (EPR) which is a result of leaky vasculature formed by the tumor tissue.[57,58]

Another reason nanoparticles have been researched for PDT is their ability to actively target the tumor tissue.[53] The surface of nanoparticles can be chemically modified after the nanoparticle has been synthesized. Post synthetic functionalization of nanoparticles with different targeting groups such as folic acid, antibodies, polysaccharides (pectin, amylose, inulin, dextran) has already been shown in the literature.[56] Folic acid is one moiety that is commonly used to target cancer cells.[59] Folate is a vitamin that aids in cell growth, therefore certain cancer lines overexpress folate receptors on their surface. The internalization of the folate-modified nanoparticle is increased by binding to these receptors on the surface of the cells.[59]

The surface of the nanoparticle can be designed to have a specific charge. The membrane of mammalian cells exhibits a negative charge from the phosphate groups that form the phospholipid bilayer. Therefore, negatively charged particles have shown less uptake into cells than neutral or positively charged particles.[60,61] However, a positive surface charge can also decrease the circulation time of nanoparticles in the body. As nanoparticles travel through the body, the mononuclear phagocyte system (MPS) will attach proteins (opsonins) to the surface of the particle. These proteins are then used to

filter particles out of the blood through the hepatic system. The MPS system acts as a barrier for the nanoparticle drug delivery systems. To increase the circulation time inside the body, a hydrophilic polymer (poly(ethylene) glycol [PEG], chitosan, inulin, etc.) can be attached to the surface of the nanoparticles.[62,63] These polymers prevent opsonins from binding to the surface allowing for longer blood circulation and increasing the passive accumulation in cancer tissue. Nanoparticles are also capable of protecting the drug from deactivation in the bloodstream and systemic leakage of drugs. Out of the plethora of nanoparticles being investigated, they can be divided into three primary categories: organic nanoparticles, inorganic nanoparticles, and hybrid nanoparticles. Each of the different vectors will be discussed showing their advantages and disadvantages.

### *1.4.1. Organic Nanoparticles.*

Organic nanoparticles can be described as particles ranging between 10 nm and 1000 nm consisting of primarily polymers and lipids.[64] Organic nanoparticles include liposomes, polymeric nanoparticles, dendrimers, and solid lipid nanoparticles. Liposomes are one type of organic nanoparticle which have been extensively used to deliver PSs.[59,65] Liposomes consist of a lipid bilayer shell and a hollow core as represented in Figure 6A. Liposomes can transport both hydrophobic and/or hydrophilic drugs due to this structure where the hydrophobic drugs can be incorporated into the lipid membrane, while hydrophilic drugs can be encapsulated in the hollow core.[66] Liposomes can be tuned to have different structural properties by changing the lipids that make up the particle and are also able to deliver therapeutics inside the cell in an efficient manner. Liposomes exhibit high biocompatibility due to the fact that the lipid bilayer is usually made of

natural lipids.[65,66] PSs can be loaded in the hydrophilic core, or they can be intercalated in the lipid bilayer of the liposome. This allows PS agents to be delivered inside the cells resulting in increased apoptosis and a decreased necrosis as compared to PSs that do not undergo complete cellular uptake.[65] If PSs are not fully internalized by the cell, then membrane damage will occur leading to necrosis, which is the undesired form of cell death due to inflammation of the tissue.

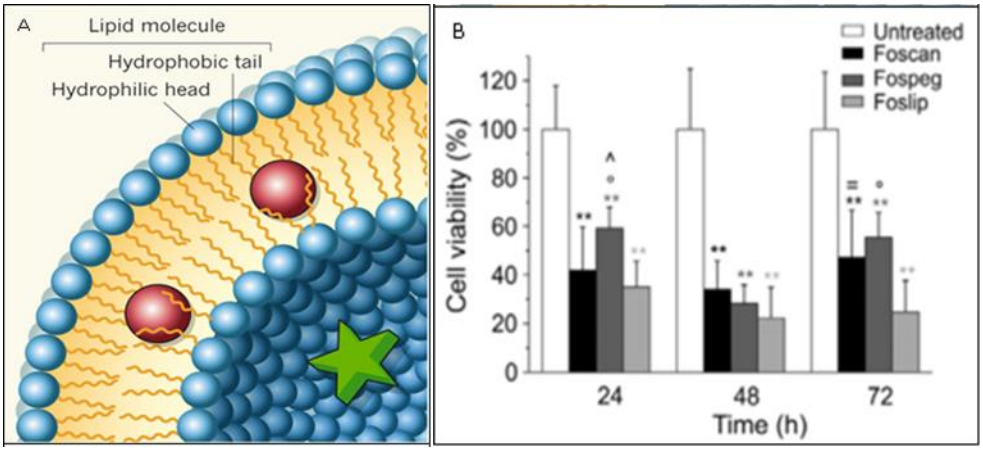


*Figure 6. A. General structure of a liposome. The phospholipid bilayer is capable of intercalating hydrophobic PSs, while hydrophilic PSs can be encapsulated in the core of the particle.[66] B. Foscan®, Foslip®, and Fospeg® were used to treat HeLa cell spheroids. Foscan is a second-generation PS, which is encapsulated in the membrane of a liposome (Foslip®). The liposome is then conjugated with PEG to increase biocompatibility and circulation time (Fospeg®). After irradiation, it was shown that the Foslip® and Fospeg® have a phototoxic effect similar to that of Foscan®.[67]*

The company Biolitec has designed two liposomal systems for the PS delivery; Foslip® and Fospeg®. In these liposomes, the PS, temoporfin (Foscan®), is incorporated in the phospholipid bilayer of the liposome. Foslip® is a formulation of a conventional liposome. Meanwhile, Fospeg® is a liposome coated with PEG to increase the biocompatibility of the nanoparticle system. Gaio et al. used each of the particles, along with Foscan® to determine the phototoxicity in multicellular spheroids of HeLa cells.[67]

The spheroids were grown to 200 μm before being incubated for 24 h with the three different therapeutics. The cells were irradiated with 22.5 J/cm$^2$ of red light, and the viability was assessed using an MTS assay at 24, 48, and 72 h after irradiation. The results showed that the particles were able to increase the phototoxicity when compared to Foscan®, as shown in Figure 6. Although liposomes have been used extensively, there is the drawback of quenching when loading a high concentration of PS molecule. When PSs are in close proximity to each other, the energy is transferred to other PS molecules instead of being transferred to oxygen to afford singlet oxygen, therefore reducing the final therapeutic effect.[27]

Polymeric nanoparticles (PNps) are another type of organic platform recently used to deliver PS agents.[49] PNps are able to degrade, either through pH responsive polymers (poly(lactic-co-glycolic acid), PLGA)[68] or through redox responsive bonds[50,69], allowing for the release of free PSs when inside the cell exhibiting high phototoxicity upon irradiation. The length of the polymer can be used to tune PNp size and control polydispersity. The polymers used are naturally hydrophilic, such as polyamidoamine (PAMAM), PEG, or PLGA, and therefore tend to aggregate less under physiological conditions. Oh et al. designed a PNp that used a glycol-chitosan polymer to incorporate the PS pheophorbide A.[69] The glycol-chitosan polymer was conjugated with redox-responsive disulfide bonds allowing the particle to degrade under highly reducing conditions. It has been shown that cancer cells have a higher reducing environment in the cytoplasm than healthy cells.[70,71] Quenching was observed when the PSs were in the particle form, however, when the particle was exposed to a reducing environment the

particle degraded and free PS was released, causing high phototoxicity upon irradiation. The particles were tested on a xenograft tumor model using HT-29 colorectal cancer cells in nude mice. When the tumors reached appropriate volume, the particles were injected in the tail vein. At 6 h post injection, the tumor was irradiated with 633 nm red light (225 $mW/cm^2$ for 30 minutes). The tumor volume was monitored for 8 days after the treatment to determine the therapeutic efficacy. The tumor volume decreased following treatment with the disulfide linkage, showing that the redox responsive particle was able to degrade and improve therapeutic efficacy as shown in Figure 7.[69]

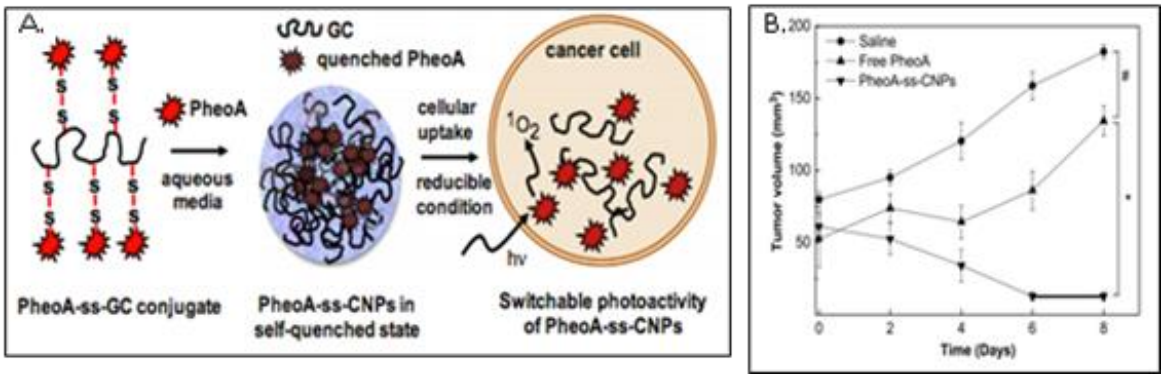


*Figure 7. A glycol-chitosan (GC) PNp was designed with disulfide linkages. The disulfide linkages are redox-responsive and the degradation of the particle will increase inside of cancer cells. Pheophorbide was bound to the GC. When the particle was formed quenching occurred, but upon degradation, the PS is released restoring efficacy. B. The PNps were tested in vivo with HT-29 xenograft tumor models. The redox responsive particles showed a decrease in tumor volume due to the release of free PS.*[69]

Despite the biocompatibility of the hydrophilic polymers, it has been shown that the polymer can act as a barrier for molecular oxygen to interact with the PS.[49] The polymer prevents molecular oxygen from reaching the PS, which prevents singlet oxygen from being produced. PNps have also shown to leak PS when physically encapsulated in the polymer. Systemic leakage will not only result in decreased amount of PS delivered

to the tumor tissue, but also cause PS accumulation in undesired tissues leading to photosensitivity.

### *1.4.2. Inorganic Nanoparticles.*

Inorganic nanoparticles are particles that are engineered using metal and metal oxides to form structures between 10 and 1000 nm.[72] Gold nanoparticles have been extensively used for imaging and as a delivery vehicle.[55,73,74] PSs can be bound to the surface of the gold nanoparticle and photoactivated when they are irradiated with light.[75] Wieder et al. has reported the attachment of a phthalocyanine to the surface of a gold nanoparticle.[75] The size of the particle after being capped during synthesis with the PS was 2-4 nm in diameter. The PS showed an increase in singlet oxygen production when bound to the gold nanoparticle as compared to the free molecular form of PS. It is thought to be due to the presence of the phase transfer agent tetraoctylammonium bromide (TOAB), as TOAB is known to increase the triplet energy transfer from a PS to molecular oxygen.[75] This was confirmed by the increase in cell phototoxicity by 43%. This study shows that inorganic metallic nanoparticles could potentially be an effective delivery vehicle for photosensitizers.

Up-conversion nanoparticles (UCNPs) are another inorganic platform that has received a lot of attention recently.[76] UCNPS combine $NaYF_4$ along with a lanthanide metal, such as $Er^{3+}$, $Tm^{3+}$, and $Yb^{3+}$, to undergo a two-photon up-conversion from IR or NIR light to visible light. Once a PS is chemically attached to the up-conversion particle the energy absorbed and upconverted by the nanoparticle can undergo Förster resonance energy transfer (FRET) to produce singlet oxygen. Zhang et al. reported an up-conversion

nanoparticle coated with silica and a zinc phthalocyanine.[77] The particle was irradiated with 980 nm light and was able to continuously produce singlet oxygen under these conditions.

Organically modified silica (ORMOSIL) nanoparticles are a third type of inorganic platform that has been used for PS delivery. Prasad et al. has designed a stable ORMOSIL particle that was able to encapsulate a pyropheophorbide.[78] It was shown that the covalent attachment reduced the leaking of PS. Moreover, the ORMOSIL system showed a high phototoxicity *in vitro* when irradiated with light.

### *1.4.3. Hybrid Nanoparticles.*

Hybrid nanoparticles are particles that contain organic and inorganic components in the same platform.[45,50,63,79–82] These nanoparticles combine the benefits of both materials.[62,80] Two hybrid silica-based platforms that have been recently explored in our lab are polysilsesquioxane nanoparticles (PSilQ NPs)[50,81–85] and mesoporous silica nanoparticles (MSNs).[51,80,86–89] PSilQ NPs have a unique design that allow for the incorporation of the therapeutic molecule into the matrix of the particle itself. This allows for a high amount of payload inside of the PSilQ material.[50,81–84] The PSilQ platform has been used for several biomedical applications including, imaging, chemotherapy, and PDT. Lin et al. first used PSilQ nanoparticles to deliver a high concentration of the chemotherapeutic drug cisplatin. Cisplatin was incorporated into the PSilQ NPs as a disuccinato prodrug form.[82,83] The prodrug was then conjugated with a silane derivative and allowing for condensation into a PSilQ NP. These particles were decorated with PEG

and used *in vivo* on xenograft mouse models using lung cancer cells A549 and H460. The tumor volume decreased significantly during the treatment using the cisplatin PSilQ NP.

In a recent study in our lab, PpIX molecules were incorporated into a PSilQ platform through a stimuli-responsive linker containing a disulfide bond to afford a biodegradable delivery system. This disulfide bond is broken inside cancer cells due to their high reducing environment. This approach affords the release of PpIX as individual units inside of the cells to avoid the self-quenching effect, which negatively impacts the phototherapeutic outcome. The PpIX PSilQ NPs cellular uptake and phototoxicity were studied using HeLa cells, where confocal microscopy showed the cellular uptake of these nanoparticles. The PSilQ NPs were incubated for 24 h then irradiated with white light. An increased phototoxic effect was observed for the PpIX PSilQ NPs containing the disulfide bond, as seen in Figure 8. To demonstrate that the PpIX molecule is indeed released inside of cancer cells, a double-labeled silica nanoparticle was designed and synthesized. In this platform, FITC was co-condensated into the silica matrix while the redox responsive PpIX monomer was grafted onto the surface of the nanoparticle. The increased phototoxicity was again seen in the presence of the disulfide bond over the control without the redox responsive bond, as seen in Figure 9.[81,90] In addition, confocal microscopy was performed to confirm the cleavage of the disulfide bond and the release of PpIX inside the cells. The FITC silica particles fluoresce in the green region of the visible and were seen clearly separated from the PpIX molecules, which fluoresce in the red region, shown in Figure 9. This proved that the disulfide bond had been cleaved and that was one cause of the increased phototoxicity. Vivero-Escoto et al. have synthesized a

PSilQ NP for the delivery of PSs.[50,81] A tetracarboxyphenyl porphyrin was made allowing for four different silane groups to be added to the ends of the porphyrin. These silane groups were then condensed to form the PSilQ Np, resulting in a higher concentration of loading of the PS molecule (11.3% wt of porphyrin).[50] These particles were tested *in vivo* with HeLa cells and were shown to have increased phototoxicity due to the high concentration of porphyrin when irradiated with red light (630-700 nm, 89 mW/cm$^2$ for 20 min).

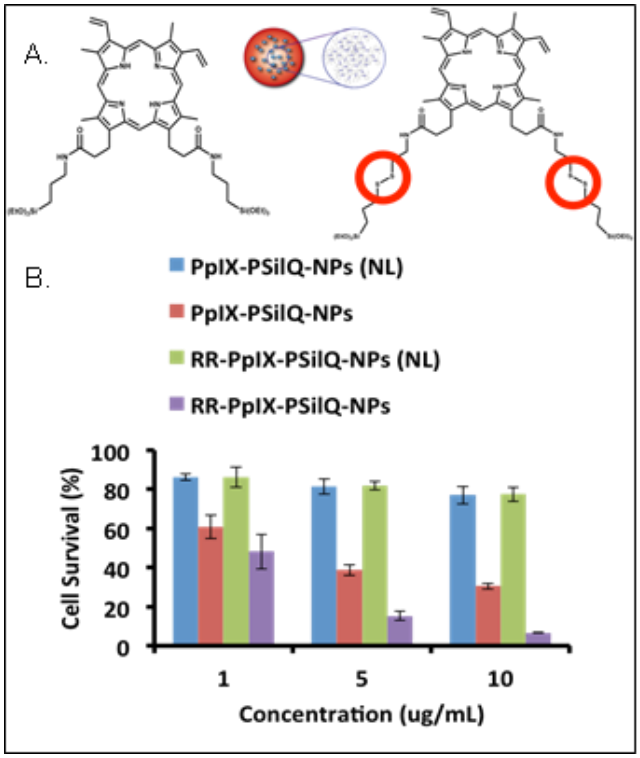


*Figure 8. A. The two PpIX molecules used in the PpIX-PSilQ-NPs and the RR-PpIX-PSilQ NPs are shown. The PpIX molecule that was functionalized with the disulfide bond is highlighted. B. The increased phototoxicity between the RR-PSilQ-NPs (purple) and PpIX-PSilQ-NPs (red) when irradiated with white light. The particles show limited toxicity when in the dark (blue and green, NL).*[81]

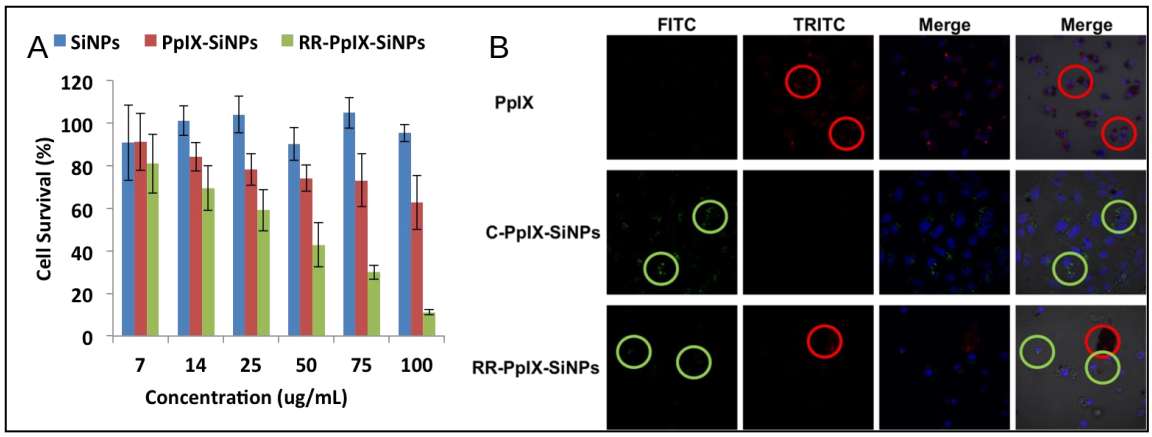


*Figure 9. A. the confocal microscope images can be seen where the silica particle can be seen in the FITC channel, and the PpIX can be seen in the TRITC channel.*

Another type of hybrid nanoparticle system is mesoporous silica nanoparticles (MSNs). This platform has been explored extensively as a drug delivery vehicle due to its high porosity, high surface area, and ability to modify its exterior and interior surface. MSNs are able to attach PS molecules to both the surface as well as inside the pores, which afford a higher amount of PS loading.[91] Mou et al. used PpIX to decorate the pores of the MSN through the bioconjugation reaction of an amine functional group.[92] The MSN was then used *in vitro* to determine the phototoxicity of the platform against HeLa cells. The cells were incubated for 2 h with the particle before being irradiated with white light. The MSN performed well producing a high phototoxic effect.

**1.5. Combination Therapy.**

One of the distinctive advantages of nanoparticles is their ability to carry more than one therapeutic agent and/or imaging agent in the same material. A devoted effort has been put forth in designing particles that are capable of carrying and delivering multiple therapeutics.[32,86,93–99] Due to the structural and chemical features of the MSN

platform, this delivery system is very attractive to develop combination therapy. MSNs have been used to combine both PDT along with chemotherapy to enhance the efficacy of the treatment.[97,100] Recently Mao et al. used an MSN that was co-loaded with Ce6 and a cisplatin prodrug to overcome platinum resistance in lung cancer (A549R).[97] The MSN was conjugated with the Ce6 (2.4% wt/wt) and cisplatin (4% wt/wt) post synthesis. The particles were incubated for 24 h before being irradiated with a low intensity light (10 $mW/cm^2$). The $IC_{50}$ values went from 25.1 μM for cisplatin to 1.16 μM with the MSN in the dark and 0.53 μM with the combined therapy of the particles. The $IC_{50}$ values show that there is a synergistic effect when cells are exposed to particles capable of delivering both PDT and cisplatin. The platinum content in the cells after incubation with nanoparticles was determined using Inductively coupled Plasma Mass spectrometry (ICP-MS) and showed that cells inoculated with MSNs that underwent both PDT and cisplatin treatment had a 7-9 times higher concentration of platinum when compared to just the cisplatin treatment.

Chen et al. also used MSNs to deliver a chemotherapeutic as well as a PS agent.[101] Firstly, doxorubicin was loaded into the pores; subsequently, histidine was added to the surface of the MSN to cap the pores. A zinc porphyrin was then attached to the histidine. The zinc porphyrin had a PEG chain attached through an aconitic anhydride intermediate yielding a pH responsive system. When the particle came in contact with the extracellular conditions of a cancer cell (pH 6.8), the aconitic anhydride would degrade releasing the PEG chain. After cellular uptake, the histidine residue would release the porphyrin and open the pores releasing the doxorubicin.[102] The cells were incubated

under light irradiation for 24 and 48 h before cell viability was calculated. The dual pH responsive particles showed a synergistic effect when both therapeutics were present.

**1.6. Summary/Outline of the Dissertation.**

This Ph.D. dissertation is organized into four chapters. Chapter 1 describes an overview of the field of PDT and nanoparticles for PS and combination drug delivery. Chapter 2 describes design, synthesis and therapeutic evaluation of the redox-responsive polysilsesquioxane nanoparticles for the delivery of PpIX (PpIX-PSilQ NPs). Chapter 3 describes synthesis, characterization and therapeutic phototoxicity of the Mesoporous silica nanoparticle-based PDT platform for the combinatorial delivery of PS, chlorin E6 and a chemotherapy agent, cisplatin. Chapter 4 is a collaborative project between the V-Lab and Dr. Afonin's lab using PSilQ NPs as a carrier for multiple therapeutics.

Naturally degrading NPs are a critical in the field of drug delivery. Chapter 2 describes the work done with redox-responsive PSilQ NPs using the PS PpIX. This chapter discusses the detailed synthesis and characterization of starting PpIX ligand used for particle synthesis and the PpIX PSilQ nanoparticles. The PpIX PSilQ NPs were then tested against triple negative breast cancer cells to determine their cellular uptake, ROS production, and phototoxicity. Finally, they were used for *in vivo* studies in orthotopic TNBC mice model to determine the phototherapeutic efficacy.

Combination therapy is one of the leading uses of nanoparticles and MSNs are an ideal system for combination therapy. Chapter 3 discusses the use of an MSN to deliver the PS chlorin E6 as well as a chemotherapy agent cisplatin. The synthesis,

characterization and drug loading of cisPt-Ce6-MSNs are discussed. Once again, the platform was tested towards TNBC cell lines and *in vivo* in orthotopic TNBC mice.

PpIX PSilQ NPs are a promising platform due to their abilities to load high concentrations of PS and have tunable surface properties. In Chapter 4, the different combinations of PpIX PSilQ NPs with chemotherapy, and gene therapy are explored. Chapter 5 describes conclusions for each project. It also addresses future work, and directions each project may be taken.

# CHAPTER 2
# BIODEGRADABLE PROTOPORPHYRIN IX LOADED SILICA-BASED NANOPARTICLES FOR IMPROVED PHOTODYNAMIC THERAPY OF TRIPLE-NEGATIVE BREAST CANCER

## 2.1. Introduction to the Project.

In this project, we synthesize and characterize a porphyrin ligand for the synthesis of polysilsesquioxane nanoparticles containing protoporphyrin-IX (PpIX), a photoactive molecule, and disulfide bonds, as redox responsive linkers (PpIX PSilQ NPs). This design affords a novel nanoplatform that allows for degradability inside the body, while also overcoming quenching that is often associated with the delivery of a high concentration of PSs. The high reducing environment found inside of cancer cells, more specifically highly aggressive types of cancers such as TNBC, is capable of cleaving the disulfide bond and releasing a PpIX derivative. The PpIX can then be utilized for PDT followed by excretion, avoiding chronic toxicity of the PpIX PSilQ NPs. The PpIX PSilQ NPs are tested *in vitro*, where the cellular uptake and phototoxicity was determined in the TNBC cell line MDA-MB-231. The phototoxicity was also studied in MDA-MB-453 and murine 4T1 cells, which both show TNBC properties. We envision that this novel PpIX PSilQ nanoplatform may enhance the phototherapeutic effect of photodynamic therapy for cancer treatment with its superior ability to deliver PSs to the tumor cells and avoid systemic toxicities.

## 2.2. Materials and methods.

### *2.2.1. Materials.*

Protoporphyrin IX was purchased from Frontier Scientific, 1-ethyl-3-(3-dimethylaminopropyl) carbodiimide (EDC) was purchased from Oakwood Chemical. Cell Titer© was purchased from Promega. BD Pharmingen™ Annexin V-FITC Apoptosis Detection Kit was purchased from BD Biosciences. *In situ* Apoptosis Detection Kit (ab206386) was purchased from Abcam Co LTD (USA). The other reagents were purchased from Sigma-Aldrich and were used without further purification. Thermogravimetric analysis (TGA) was determined using a Mettler Toledo TGA/SDTA851 instrument (Mettler-Toledo AG Analytical, Schwersenbach, Switzerland) with a platinum pan and a heating rate of 1.0 °C/min from 25.0 to 800.0 °C under a nitrogen atmosphere. The sample was held at 800.0 °C for 3 h to make sure that all the organic material had been calcined. A Raith 150 Field Emission Scanning Electron Microscope (SEM) (Raith America Inc., New York, NY, USA) was utilized to measure the particle size and shape of the materials. Nanoparticle samples were suspended in methanol in preparation for the SEM. Dynamic light scattering (DLS) and ζ-potential measurements were carried out using a Malvern Instrument Zetasizer Nano (red laser 633 nm) (Malvern Instrument Ltd., Malvern, UK). The amount of Protoporphyrin IX (PpIX) molecules loaded into the PSilQ NPs was quantified by UV-vis spectroscopy (Varian, Cary 300 Bio UV/vis spectrometer) (Varian, Sydney, Australia). The photophysical properties of PpIX PSilQ NPs were determined using UV-vis and fluorescence (Varian, Cary Eclipse fluorescence). A BD LSRFortessa™ cell analyzer was used for the

fluorescence-activated cell sorting (FACS) experiments. An Olympus Fluoview FV 1000 confocal fluorescence microscope system was used for the LCSM experiments. The IVIS Imaging system was used to determine the fluorescence of the NPs for the *in vivo* studies. The excitation/emission was performed at 605/680 and 745/820 nm to image PpIX and NIR dye, respectively. LINCE light was used for irradiation for the *in vivo* studies. Organs were homogenized using an IKA® high speed digital homogenizer. All tissue slides were visualized using an Olympus IX71 fluorescence microscope.

### *2.2.2. Experimental methods.*

#### *2.2.2.1. Synthesis of PpIX ligand and PpIX PSilQ nanoparticles.*

##### *2.2.2.1.1. Synthesis of Protoporphyrin IX-N-Succinimide Ester (2).*

The synthesis of protoporphyrin IX succinimide ester (PpIX-SE) was carried out by placing 0.889 mmol (500.00 mg) of protoporphyrin IX (PpIX) (**1**) in a round bottom flask containing 20 mL of dimethyl sulfoxide (DMSO) and 70 mL of dichloromethane (DCM). To this solution, 2.226 mmol (272.00 mg) of 4-dimethyl amino pyridine was added along with a solution of 5.320 mmol (1.02 g) of 1-ethyl-3-(3-dimethylaminopropyl)carbodiimide (EDC) hydrochloride in 20 mL of DMSO. The flask was then placed in an ice bath and stirred for 10 min. To this mixture, 5.326 mmol (613.00 mg) of N-hydroxysuccinimide (NHS) was added to the flask and was kept in an ice bath for 3 h with stirring. The ice bath was removed, and the solution was stirred for another 45 h at room temperature. A diluted ethanolic solution in water (100 mL, 25% vol./vol.) was added to the flask to afford precipitation of the product. PpIX-SE was then

collected through suction filtration and washed with ethanol before being dried in a lyophilizer. Yield: 506.00 mg (76 %wt.); $^{1}$H NMR (300MHz, DMSO-$d_6$, ppm): δ 3.59-3.72 (dd, 13H), 4.41 (d, 4H), 8.15-8.46 (m, 2H), 10.25 (d, 4H); FT-IR ($cm^{-1}$): 3503 (N-H), 2915 (C-H), 1808 (C=O), 1778 (C=O), 1732 (C=O), 1627 (C-N); MALDI-MS (m/z): Calculated: $[M]^+$ = 754.30, $[M+1]^+$ = 755.30; Observed: $[M+1]^+$ = 755.32, $[M+2]^+$ = 756.31. UV-Vis (DMF, nm): 404 (S-band), 623, 576, 542, 506 (Q-bands). Molar extinction coefficient (λ = 404 nm; DMF; mol $L^{-1}$ $cm^{-1}$): 195,800.

*2.2.2.1.2. Synthesis of Protoporphyrin IX-Cysteine (3).*

To synthesize protoporphyrin IX-cysteine (PpIX-Cys), 0.464 mmol (350.00 mg) of PpIX-SE (**2**) was added to 25 mL of DMSO. To this solution, cysteine hydrochloride (1.142 mmol, 180.00 mg), which was previously dissolved in 3 mL of $H_2O$, was added along with di-isopropyl ethyl amine (DIPEA) (2.01 mmol, 350 $\mu$L). The reaction was heated and stirred at 120 ºC for 72 h. Dilute ethanol in water (300 mL, 20% vol./vol.) was added to the reaction with 200 μL of concentrated HCl to precipitate the product. The product was collected through gravity filtration and washed with water before being dried in vacuum. Yield: 176.00 mg (49 %wt.); $^{1}$H NMR (300MHz, DMSO-$d_6$, ppm): δ 3.37-3.72 (m, 10H), 6.86 (s, 1H), 7.03 (s, 1H), 7.20 (s, 1H), 8.02 (s, 1H), 10.25 (d, 4H); FT-IR ($cm^{-1}$): 2921 (C-H), 1709 (C=O), 1649 (N-H), 1535 (C-C); UV-Vis (DMF, nm): 404 (S-band); 628, 575, 540, 506 (Q-bands). Molar extinction coefficient (λ = 404 nm; DMF; mol $L^{-1}$ $cm^{-1}$): 73,200.

*2.2.2.1.3. Synthesis of Protoporphyrin IX-Pyridine-Disulfide-Cysteine (4).*

The thiol group of PpIX-Cys was activated using 2,2'-dipyridyldisulfide (DPDS). This reaction proceeded by dissolving PpIX-Cys (**3**) (0.130 mmol, 100.00 mg) in 10 mL of DMSO. In a separate vial, DPDS (0.522 mmol, 115.00 mg) was dissolved in 1 mL of DMSO. This solution was added to the PpIX-Cys solution followed by the addition of 25 μL of acetic acid. The final mixture was stirred for 24 h at 120 ºC. After that, an ethanolic solution in water (200 mL of 25% vol./vol.) was added along with 250 μL of hydrochloric acid to afford precipitation. The product was filtered before drying in a lyophilizer overnight. Yield: 62.30 mg (48.6 %wt.); FT-IR ($cm^{-1}$): 3301 (N-H), 2917 (C-H), 1707 (C=O), 1648 (C-N); UV-Vis (DMF, nm): 409 (S-Band), 633, 577, 539, 504 (Q-bands). Molar extinction coefficient ($\lambda$ = 409 nm; DMF; mol $L^{-1}$ $cm^{-1}$): 77,800.

*2.2.2.1.4. Synthesis of Protoporphyrin IX-Mercaptopropyl-Triethoxy silane (5).*

The PpIX-Cys silane precursor was synthesized by reacting a solution of compound (**4**) (0.10 mmol, 100.00 mg) in 10 mL of DMSO with 75 $\mu$L (0.10 mmol) of 3-mercaptopropyltriethoxysilane (MPTES) for 48 h at room temperature. After that, an ethanolic solution (200 mL of 25% vol./vol.) and 200 $\mu$L of HCl conc. (37%) were added to afford a precipitate. The final product was filtered and dried overnight in a lyophilizer. Yield: 79.00 mg (63 %wt.); FT-IR ($cm^{-1}$): 3299 (N-H), 2917 (C-H), 1651 (C-N), 1228 (Si-C), 1012 (Si-O); UV-Vis (DMF, nm): 409 (S-Band), 633, 577, 540, 506 (Q-bands). Molar extinction coefficient ($\lambda$ = 409 nm; DMF; mol $L^{-1}$ $cm^{-1}$): 59,500.

*2.2.1.5. Synthesis of Methoxy-Poly(ethyleneglycol)-Amine (MeO-PEG-$NH_2$).*

To synthesize MeO-PEG-$NH_2$, a method previously reported in literature was used,[103] mPEG-OH (MW = 2K Da; 1 mmol, 2.00 g) was heated to 90 ºC under vacuum overnight. Dry THF (10 mL) was added along with methyl sulfonyl chloride (19.38 mmol, 1.5 mL). The solution was transferred to an ice bath and DIPEA (17.22 mmol, 3.0 mL) was added dropwise over a period of 30 min. After that, the solution was stirred overnight at room temperature. Nanopure water was added to dissolve any solid that has formed, followed by the addition of sodium bicarbonate solution (1 N, 2 mL) and sodium azide (23.08 mmol, 1.50 g). THF was removed by rotary evaporation. After that, the aqueous layer was refluxed overnight. The mPEG-$N_3$ product was extracted with dichloromethane (DCM, 5x15 mL), and washed with brine solution. Magnesium sulfate was used to dry the solution and was filtered out before removal of the DCM by rotary evaporation. Triphenyl phosphine (6.3 molar equivalents) was added to the product and dissolved in dry THF (12 mL) under nitrogen atmosphere. The solution was stirred overnight. Nanopure water (1.4 mL) was added and the solution was again stirred overnight. THF was removed by rotary evaporation and ~20 mL of $H_2O$ was added. The precipitate was filtered out of solution, and the product was dried by rotary evaporation and placed in a lyophilizer. Yield: 1.28 g (64 %wt.); $^1$H NMR (300MHz, $CDCl_3$, ppm): δ (t, 6H, 2.65-3.01), (s, 3H, 3.31-3.41), (m, 180H, 3.55-3.65); FT-IR ($cm^{-1}$): 3401 (N-H), 2986 (C-H), 1665 (C-N), 1107 (C-O).

*2.2.2.1.6. Synthesis of PpIX PSilQ and mPEG PpIX PSilQ Nanoparticles.*

The synthesis of PSilQ nanoparticles was carried out through a reverse-microemulsion method.[50,81] An organic phase was prepared by mixing 7.08 g (6.6 mL) of Triton-X100, 6.4 mL of hexanol, and 30 mL of cyclohexane. At the same time, an aqueous solution containing 8.00 mg of the PpIX silica precursor (**5**), 5.6 mL of $H_2O$ and 1 mL of $NH_4OH$ was prepared and added dropwise to the organic solution. The emulsion was stirred for 24 h at room temperature. Afterwards, the PpIX PSilQ NPs were obtained by crashing out the material with the addition of EtOH (40 mL). The material was separated from the solution by centrifugation and washed twice with EtOH to get rid of any starting reagents. The final product was stored in EtOH.

10 mg of PpIX PSilQ NPs were dispersed in 10 mL of DMF. EDC (0.13 mmol, 25 mg) and 50 mg of mPEG-$NH_2$ was added. The solution was allowed to stir for 48 hrs at RT. The mPEG PpIX PSilQ NPs were collected by centrifugation and stored in ethanol. For the NIR derivative, 50 mg of NIR mPEG was used in the same procedure.

*2.2.2.2. Photophysical characterization of PpIX PSilQ nanoparticles.*

*2.2.2.2.1. Determination of Singlet Oxygen ($^1O_2$) generated by PpIX and PpIX-Cys molecules.*

To measure the amount of $^1O_2$ generated by PpIX and PpIX-Cys, 40 µL of the singlet oxygen probe 1,3-diphenylisobenzofuran (DPBF) from a stock solution (8 mM, DMF) was diluted in 4 mL of a DMF solution containing the equivalent amount of 5 µM of either PpIX or PpIX-Cys. The solution was irradiated with white light (400–700 nm, 9 mW/cm$^2$) at different times (10, 20 and 30 s). The absorbance at 419 nm was measured of

each solution using a UV-vis spectrophotometer after illumination. Moreover, control experiments were run in the absence of light. In addition, experiments were carried out using red light (570–690 nm, 14 mW/cm$^2$) following the same protocol. All the experiments were run in triplicate. The decrease from the original amount of DPBF was used to calculate the concentration of $^1O_2$ produced.

*2.2.2.2.2. Determination of Singlet Oxygen ($^1O_2$) generated by PpIX PSilQ NPs.*

To measure the amount of $^1O_2$ generated by PpIX PSilQ NPs, 40 µL of DPBF from a stock solution (8 mM, DMF) were diluted in 4 mL of a DMF dispersion of PpIX PSilQ NPs containing 5 µM of PpIX (46.88 µg/mL). The solution was irradiated with white light (400–700 nm, 9 mW/cm$^2$) at different times (60 and 120 s). The absorbance at 419 nm of these solutions was measured using a UV-vis spectrophotometer after illumination. Moreover, control experiments were run in the absence of light. In addition, experiments were carried out using red light (570–690 nm, 14 mW/cm$^2$) following the same protocol. All the experiments were run in triplicate. The decrease in absorption by DPBF was used to calculate the concentration of $^1O_2$ produced.

*2.2.2.2.3. Photophysical Characterization of PpIX, PpIX-Cys molecules, PpIX PSilQ, and mPEG PpIX PSilQ NPs.*

A Cary 300 Bio UV/vis (Varian, Sidney, Australia) and a Cary Eclipse fluorescence spectrometers (Varian, Sidney, Australia) were used to determine the absorption and fluorescence emission of PpIX, PpIX-Cys molecules, PpIX PSilQ NPs, and mPEG PpIX PSilQ NPs, respectively. The PpIX derivatives were prepared in a DMF solution of 0.333 µM. The nanoparticles were dispersed in DMF to result in a PpIX

concentration of 5 µM. To quantify the amount of PpIX loaded in the PpIX PSilQ NPs, the absorbance of a dispersion of NPs in DMSO (0.5 mg/mL; 3 mL) was measured using the UV-vis spectrometer. The amount of PpIX was calculated using a calibration curve of PpIX in DMSO.

*2.2.2.2.4. PpIX release from PpIX PSilQ NPs under high reducing environment.*

To determine the release of the PpIX compound under simulated reducing conditions, the reducing agent dithiothreitol (DTT) was used. The PpIX PSilQ NPs were washed several times (a minimum of five times) with DMF to eliminate any physiosorbed porphyrin. The nanoparticles were redispersed in 10 mL of DMF with a concentration of 0.5 mg/mL. The dispersion was stirred for 19 h total under $N_2$ atmosphere to determine the amount of background PpIX release. After the background was determined, DTT was dissolved in the dispersion to get a 10 mM final concentration of DTT. Aliquots were taken at different time points, NPs were removed by centrifugation, and the UV-vis absorption of the supernatant was measured to determine the amount of PpIX molecules released. A similar procedure was followed for the control PpIX PSilQ NPs that were only stirred in DMF (no addition of DTT).

*2.2.2.3. In vitro studies.*

TNBC cells like MDA-MB-231 and MDA-MB-453, BC cells like MCF-7 and normal mammary epithelial cells (MCF-10a) were used for the cellular uptake of PpIX PSilQ NPs, phototoxicity studies, and evaluation of ROS production in cells.

*2.2.2.3.1. Cellular uptake analysis of PpIX PSilQ NPs using confocal Microscopy.*

MDA-MB-231 cells were seeded at a concentration of $5 \times 10^4$ cells/well on a glass cover slip in a 6 well plate with 2 mL of complete RPMI-1640 media. After 24 hours, the cells were inoculated with PpIX PSilQ NPs and mPEG PpIX PSilQ NPs at a concentration of 50 μg/mL in RPMI-1640 media for 24 h. The cells were then washed with PBS and the glass cover slip was placed on a microscope slide for examination using an Olympus FluoView FV 1000 confocal microscopy instrument.

*2.2.2.3.2. Cellular uptake analysis of PpIX PSilQ NPs using Fluorescence-activated Cell Sorting (FACS).*

MDA-MB-231 cells were seeded at a concentration $1 \times 10^5$ cells/well in a 6 well plate with 2 mL of complete RPMI-1640 media. The cells were allowed to attach for 24 h and inoculated with PpIX PSilQ NPs and mPEG PpIX PSilQ NPs at a concentration of 50 μg/mL in RPMI-1640 media for 48 h. The cells were subsequently washed with PBS, trypsinized, and collected through centrifugation. The cells were redispersed in 0.5 mL of RPMI-1640 complete media and 100 μL of trypan blue was added. The cells were analyzed using a BD LSR Fortessa flow cytometer instrument. Statistical analysis: Experiments were run by triplicate and the statistical differences were determined using ANOVA.

*2.2.2.3.3. Evaluation of phototoxicity of PpIX PSilQ NPs in TNBC cells.*

MDA-MB-231 (TNBC), MDA-MB-453 (TNBC), MCF-7 (BC) and MCF-10a (mammary) cells were used to assess the phototoxicity. MDA-MB-231 and MCF-7 were cultured in RPMI 1640 with 10% FBS and 1% penicillin/streptomycin. MDA-MB-453

cells were cultured in DMEM with 10% FBS, 1% penicillin/streptomycin, 1% GlutaMAX, and 1% NEAAs. MCF-10a were cultured in MEBM supplemented with cholera toxin. MDA-MB-231, MDA-MB-453, MCF-7, and MCF-10a cells were seeded at a concentration of $5 \times 10^3$ cells/well in a 96 well plate with 100 μL of media. Once seeded, the cells were allowed to attach for 24 h before inoculation with PpIX, PpIX PSilQ NPs, or mPEG PpIX PSilQ NPs at concentrations ranging from 0.1-5 μM of PpIX for 72 h. The cells were washed twice before irradiation with a Biotable power source and RGB LED array (MM Optics, University of Sao Paulo/Sao Carlos, Brazil) at 620-630 nm for 20 min at 24.5 mW/cm$^2$ (30 J/cm$^2$) in PBS. After irradiation, the PBS was removed, and fresh media was replaced. Irradiation was performed a second and third time at 4 h and 8 h after the first wash for a total fluence of 90 J/cm$^2$. 24 h after the first irradiation, the cells were washed again with PBS before adding 120 μL of a 17% Cell Titer® solution in RPMI-1640 where they were placed back in the incubator for 3 h. Absorption of the MTS assay was taken at 490 nm 3 h later to determine phototoxicity.

*2.2.2.3.4. Determination of in vitro ROS generation by PpIX PSilQ NPs.*

MDA-MB-231 cells were seeded in a 6-well plate at a concentration of $2 \times 10^5$ cells per well. The cells were allowed to attach for 24 h before inoculation with the PpIX PSilQ NPs and mPEG PpIX PSilQ NPs (16.5 μg/mL; 2 μM PpIX). The cells were washed twice with PBS 24 h after inoculation. A 10 μM solution of 2',7'-dichlorodihydrofluorescein diacetate (DCF-DA) in serum free media was added for 30 minutes and the cells were washed with PBS after treatment with DCF-DA. Fresh PBS was placed on the cells before irradiation with red light (BioTable, 620–630 nm) for 20

min at 24.5 mW/cm$^2$ (29.4 J/cm$^2$). The PBS was removed and stored to keep any live cells that were detached during the washing procedure. The cells were then trypsinized, the previous PBS washing was added and cells were centrifuged down. The cells were resuspended in 500 μL of serum free media and were analyzed using a BD LSR Fortessa flow cytometer instrument [FITC channel]. Statistical analysis: Experiments were run by triplicate and the statistical differences were determined using ANOVA.

*2.2.2.3.5. Determination of apoptotic cells using Annexin-V assay.*

MDA-MB-231 cells were seeded in a 6-well plate at a concentration of 2 × 10$^5$ cells per well. The cells were allowed to attach for 24 h before inoculation with the PpIX PSilQ NPs and mPEG PpIX PSilQ NPs (16.5 μg/mL; 2 μM PpIX). The cells were then washed twice with PBS 24 h after inoculation. Fresh PBS was placed on the cells before irradiation with red light (BioTable, 620–630 nm) for 20 min at 24.5 mW/cm$^2$ (30 J/cm$^2$). The PBS was removed and stored to keep any live cells that were detached during the washing procedure. The cells were then trypsinized, the previous PBS washing was added, and cells were centrifuged down. The cell pellet was then washed with 1 mL of 1X binding buffer provided with the Annexin V kit assay. The cells were resuspended in 100 μL of binding buffer before 5 μL of Annexin V-FITC solution was added. The cell suspensions were stored for 15 min in the dark and transferred to a 15 mL centrifuge tube. Later, 2 mL of binding buffer was added, and the cells were centrifuged, and the supernatant was discarded. The cells were resuspended in 200 μL of binding buffer and 5 μL of propidium iodide staining solution and transferred to flow cytometry tubes. The

solution was incubated for 15 min in the dark before being analyzed using a BD LSR Fortessa flow cytometer instrument.

*2.2.2.4. In vivo studies.*

*2.2.2.4.1. Biodistribution and biocompatibility.*

C57/BL mice (n=3) were intravenously (retro orbital, *r.o.*) injected with a range of concentrations (20, 40, and 60 mg/Kg) of NIR grafted PEG PpIX PSilQ NPs. NIR 797 was attached to diamino PEG through an EDC coupling reaction. The NIR-PEG was immediately conjugated to the surface using the same synthesis as previously described. The mice were imaged using the IVIS imaging system prior to injection and at the following time points post injection: 5 min, 30 min, 1 h, 4 h, 24 h, 48 h, 96 h. The mice were sacrificed 10 days after the administration of NPs and the organs were collected and imaged for *ex vivo* fluorescence. The imaging using IVIS instrument was performed at 605/680 and 745/820 nm (excitation/emission) to image PpIX and NIR dye, respectively.

*2.2.2.4.2. Determination of PpIX content in organs.*

The lungs, liver, and kidneys were weighed and placed in an extraction solution of 1% SDS in methanol:1N perchloric acid (1:1 v:v) where they were each homogenized using an IKA® T-25 high speed digital homogenizer until no solid pieces remained.[104] The homogenized organ solution was left for 24 h to extract PpIX from the tissue. After 24 h, the solution was centrifuged, and the supernatant was collected and fluorescence measurements (Ex/Em: 407/620 nm) were taken in a 96 well plate. The concentration was determined through a calibration curve at 620 nm. The PpIX content was also analyzed in the phototherapeutic efficacy groups. The liver, lungs, and tumor were

homogenized using the same method. Again, after 24 h the solution was centrifuged, and the supernatant was collected, and fluorescence was measured in a 96 well plate.

*2.2.2.4.3. Evaluation of targeting ability of PpIX PSilQ nanoparticles.*

An orthotopic xenograft tumor model was used to determine the targeting ability of the PpIX PSilQ NPs. The mouse (NOD SCID gamma, NSG) was injected with $1x10^6$ MDA-MB-231 cells (100 μL of 1:1 growth factor reduced matrigel/PBS) in the right flank of the mouse. Once the tumor reached ~400 $mm^3$ $\left(\frac{l \times w^2}{2}\right)$, the mouse was injected with 50 mg/Kg of NIR-PEG conjugated PpIX PSilQ NPs (prepared in the same manner as previously described). The mouse was imaged prior to injection and imaged at the following time points post injection: 5 min, 30 min, 1 h, 4 h, 24 h, 48 h. The mouse was sacrificed at 48 h post injection and the major organs were harvested and imaged. The excitation/emission was performed at 605/680 and 745/820 nm to image PpIX and NIR dye, respectively.

*2.2.2.4.4. Evaluation of phototherapeutic efficacy of PpIX PSilQ nanoparticles.*

An orthotopic xenograft mouse model was used to determine the phototherapeutic efficacy. The mice (NOD SCID gamma, NSG) were injected with $5x10^5$ MDA-MB-231 cells (100 μL of 1:1 growth factor reduced matrigel/PBS) into the $4^{th}$ mammary fat pad. Once the tumor reached ~100 $mm^3$ $\left(\frac{l \times w^2}{2}\right)$, the mice were randomly divided into following groups (n=3): phosphate buffer solution (PBS), PpIX with red light, mPEG PpIX PSilQ NPs, and mPEG PpIX PSilQ NPs with red light. The treatment consisted of

total 5 injections in alternating eyes (*r.o.*) with an interval of four days between injections. Following each injection, there were three irradiations using the LINCE instrument at 24 h, 30 h, and 48 h post injection with red light (125 mW/cm$^2$, 12 min, 90 J/cm$^2$).[29] The irradiation conditions were performed to prevent the formation of hypoxic environment. The tumor sizes were monitored using a digital caliper every other day until 7 days after the final injection when the mice were euthanized. Blood was collected for toxicity testing, the tumor was excised, weighed and the tumor and all major organs were collected and fixed for further analysis.

*2.2.2.4.5. Hematoxylin and eosin (H&E) staining for toxicity evaluation.*

Tumors and major organs were fixed using a buffered 10% formalin solution for 24 h before being transferred to 70% ethanol. The organs were paraffin-embedded, sectioned (4 μm thick), and stained with H&E. Histopathological changes were observed using a fluorescent microscope (IX71, Olympus).

*2.2.2.4.6. Apoptosis Staining.*

Parafin-embedded tumor tissue (10 μm thick) was stained using the Abcam Co LTD. (USA) "*In situ* Apoptosis Detection Kit (ab206386)" as per manufacturer's instructions. The staining was observed using a fluorescent microscope (IX71, Olympus).

## 2.3. Results and discussion.

### *2.3.1. Synthesis and characterization of redox-responsive PpIX silane ligand.*

The synthesis of the redox-responsive PpIX silane ligand was performed through a series of sequential reactions as shown in **Figure 10**. First, the carboxylic acid groups in the PpIX molecule were activated using N-hydroxy succinimide (NHS) through a

coupling reaction mediated by 1-ethyl-3-(3'-dimethylaminopropyl)carbodiimide (EDC) to afford PpIX-SE (**2**).[105] Compound **2** was reacted with cysteine hydrochloride in the presence of diisopropylethylamine (DIPEA) affording PpIX-Cys (**3**). The thiol group in compound **3** was modified by a disulfide exchange reaction using dipyridine disulfide (DPDS) to afford **4**.[50] DPDS acted as an activating group for the next reaction between compound **4** and 3-mercaptopropyltriethoxysilane (MPTES) through another disulfide exchange reaction to produce the final redox-responsive PpIX silane ligand (**5**).

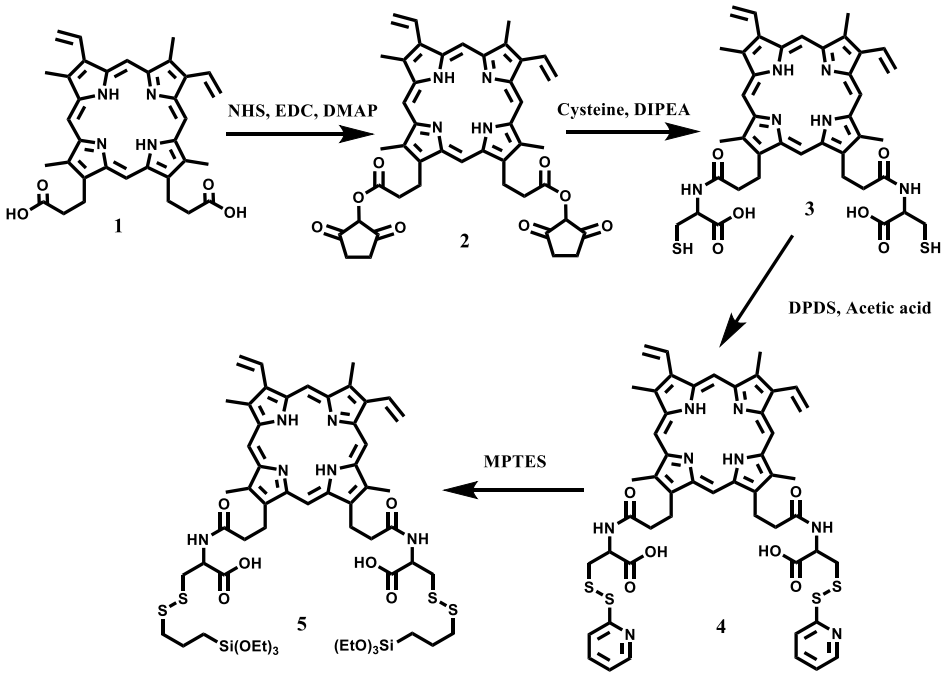


*Figure 10. Schematic representation of the synthesis of the redox responsive PpIX silane ligand. The carboxylic acid groups were activated through an EDC/NHS coupling reaction. Following activation, cysteine was added as a trifunctional linker. The thiol group on cysteine was modified using dipyridine disulfide and finally, the mercaptopropyl silane group was attached through a disulfide exchange reaction.*

The photophysical properties of compounds **1-4** were characterized by UV-vis absorption and fluorescence spectroscopy. The UV-Vis spectrum of each of the ligands **1-4** were measured in solutions prepared in DMSO. All the compounds show the

characteristic Soret-band and the four Q-bands of a porphyrin molecule (**Figure 11a**).[17,27] The fluorescence spectra of the PpIX derivatives show two emission peaks at 630 and 700 nm (**Figure 11b**), which is characteristic of the $^1(\pi \leftarrow \pi^*)$ transition and the tautomerism of hydrogens on the inner macrocyclic ring of the porphyrin.[17,106] The decrease in absorption and fluorescence for **3** and **4** can be attributed to differences in solubility leading to an increase in aggregation of the molecules in DMSO, and hence the compound **5** was not characterized.[107]

It has been extensively confirmed that $^1O_2$ is essential for the photodynamic process to kill cancer cells.[39] The generation of singlet oxygen ($^1O_2$) from PpIX and compound **3** was further investigated using red light (570-690 nm). These are the two possible PS that will be released from the PpIX PSilQ NPs after either hydrolysis of the amide bond or cleavage of the disulfide bond under high reducing conditions (Figure 10).[50,69,108] The $^1O_2$ probe, diphenylisobenzofuran (DPBF), was used to determine $^1O_2$ production. The production of $^1O_2$ decomposes DPBF through an endoperoxide to yield 1,2-dibenzoylbenzene, reducing the absorption of the solution, which is inversely proportional to the amount of $^1O_2$.[36,109] The generation of $^1O_2$ in DMF was tested using three radiant exposures, 0.14, 0.28 and 0.42 J/cm$^2$ (570–690 nm, 14 mW/cm$^2$). PpIX shows higher production of $^1O_2$ compared with compound **3**, most likely due to differences in the solubilities (**Figure 11c**).[110]

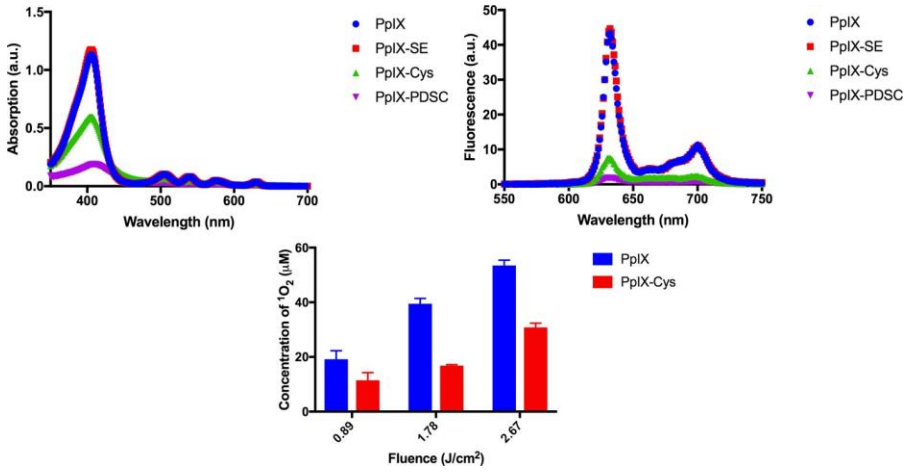


*Figure 11. UV-vis absorption spectrum for PpIX (blue), and compounds 2 (red), 3 (green) and 4 (purple). Fluorescence emission spectrum for PpIX (blue), and compounds 2 (red), 3 (green) and 4 (purple). Generation of $^1O_2$ measured by DPBF for PpIX (red) and compound **3** (blue). Error bars represent the standard deviation of three independent experiments.*

### *2.3.2. Synthesis and characterization of redox-responsive PpIX polysilsesquioxane nanoparticles (PpIX PSilQ NPs).*

The synthesis of PpIX PSilQ NPs was performed using a reverse micro-emulsion technique.[80] We used a four-component approach including Triton™ X-100 and hexanol as surfactant and co-surfactant, which were dispersed in cyclohexane as the organic solvent, and water as the aqueous phase. Redox-responsive PpIX silane derivative **5** was dissolved in water in the presence of ammonium hydroxide. The use of the base has two purposes; first, to solubilize compound **5** in water by forming the carboxylate version and increase the rate of hydrolysis and condensation of **5** to afford the desired PpIX PSilQ NPs (**Figure 12**).[111,112] The surface of PpIX PSilQ NPs was further functionalized with MeO-PEG-$NH_2$ (MW = 2KDa) by a coupling reaction with the carboxylic acid groups exposed on the surface of the nanoparticles to afford mPEG PpIX PSilQ NPs.

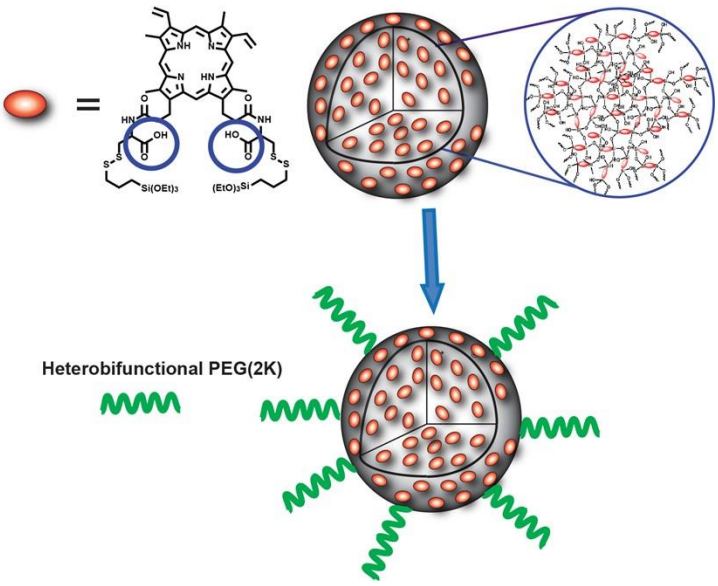


*Figure 12. Schematic representation for the fabrication of PpIX PSilQ and mPEG PpIX PSilQ NPs. PpIX PSilQ NPs were synthesized by a reverse microemulsion approach. The NPs were further modified with PEG by a coupling reaction using the chemically available carboxylic acid groups from* ***5*** *(blue circles).*

The structural properties of PpIX PSilQ and mPEG PpIX PSilQ NPs were characterized through scanning electron microscopy (SEM), dynamic light scattering (DLS), ζ-potential, and thermogravimetric analysis (TGA). SEM images show PpIX PSilQ NPs with diameters in the range of 40 ± 10 nm (**Figure 13**). DLS and ζ-potential measurements were performed to determine the hydrodynamic diameter ($D_h$) and surface charge of the particles, respectively. The DLS and ζ-potential measurements were carried out in 1 mM phosphate buffer solution (PBS). PpIX PSilQ NPs have a $D_h$ of 120 ± 50 nm with a surface charge of -36 ± 0.5 mV (n=5). The Dh of the nanoparticles are larger than the diameter found by SEM due to swelling of the PSilQ particles in solution.[113] The negative charge on the surface of the PpIX PSilQ NPs is a clear indication of the presence of carboxylate groups, which are produced after deprotonation, under physiological pH,

of the carboxylic acid moieties in compound **5**. After modification with PEG chains, the surface charge increased to -11 ± 4 mV (n=3) due to the presence of the polymer. The colloidal stability of the PpIX PSilQ and mPEG PpIX PSilQ platforms was evaluated in cell media containing fetal bovine serum during 24 h (**Figure 13a**). The stability plots showed an increase in the Dh up to 450 nm for both materials in the presence of serum, slightly lower for the PEGylated nanoparticles, most likely due to the formation of protein corona.[114] Nevertheless, after few hours and slight decrease of the Dh for both materials, the Dh kept fairly constant for PpIX PSilQ (~405-355 nm) and mPEG PpIX PSilQ NPs (~330-280 nm) during the rest of the experiment. Despite that the Dh for this system may be larger than expected due to some aggregation; our *in vivo* experiments described below, fully demonstrated that this platform has remarkable features for the delivery of PpIX.

The loading of PpIX molecules in the PpIX PSilQ and mPEG PpIX PSilQ NPs was determined through UV-Vis spectroscopy (**Figure 13c**). The amount of PpIX in the PpIX PSilQ and mPEG PpIX PSilQ NPs was determined to be 5.7 ± 2.2 and 4.2 ± 0.4 wt. %, respectively (n=5). The UV-vis spectra of both the PpIX PSilQ and mPEG PpIX PSilQ NPs showed the characteristic S-band and the four Q-bands associated to PpIX. The fluorescence of the PpIX PSilQ NPs drastically decreased when compared to the PpIX or compound **3** (**Figure 13d**), which can be associated to the self-quenching effect occurring due to the close proximity of the PpIX molecules inside of the nanoparticles.[69] A similar effect was also observed during the production of $^1O_2$. At a light fluency of 0.27 J/cm$^2$ with red light, PpIX and compound **3** produces 53.5 and 31 μM of $^1O_2$,

respectively; whereas the PpIX PSilQ NPs, with a similar amount of PpIX content, produce only 11 μM of $^1O_2$ (**Figure 13e**) a five- and three-fold reduction on the generation of $^1O_2$ compared with PpIX and **3**. Our group has used this self-quenching effect approach using PSilQ platform to rationally design stimuli-responsive systems where once the PS agent is encapsulated in the nanoparticle, the generation of $^1O_2$ is dramatically reduced; however, once the PSilQ NPs have been degraded to release PS as individual molecule, the $^1O_2$ production is restored.[69]

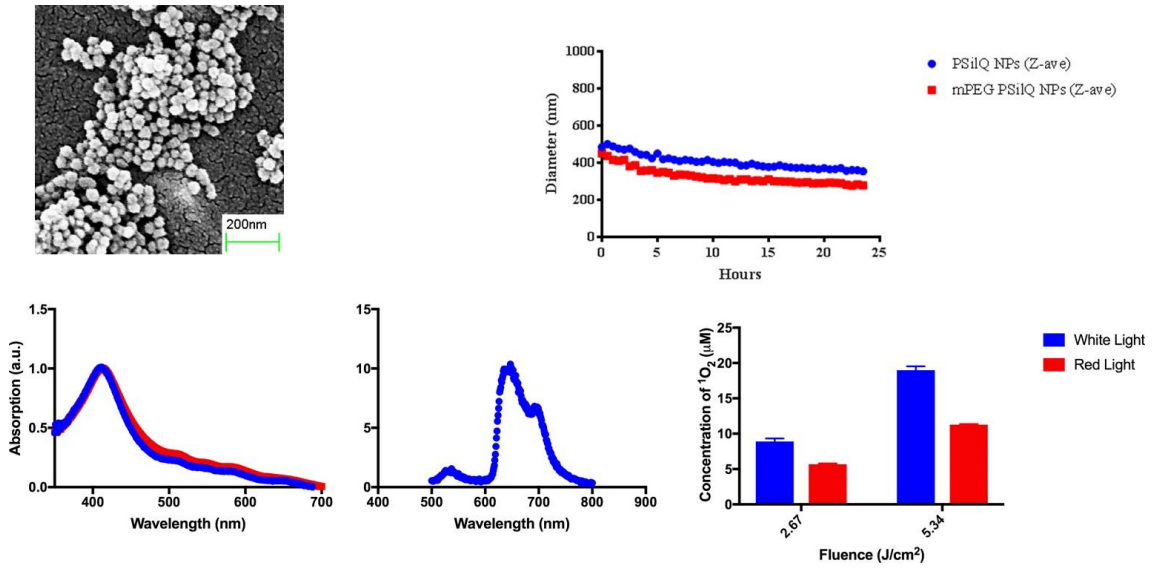


*Figure 13. Structural and photophysical properties of PpIX PSilQ and mPEG PpIX PSilQ NPs. SEM image of PpIX PSilQ NPs. Colloidal stability of the PSilQ NPs in the presence of serum. UV-vis (normalized) and fluorescence spectrum of PpIX PSilQ (red) and mPEG PpIX PSilQ (blue) NPs (0.5 mg/mL; ~50 uM PpIX). Generation of $^1O_2$ by PpIX PSilQ (red) and mPEG PpIX PSilQ (blue) NPs.*

To evaluate the stimuli-responsive ability of the PpIX PSilQ and mPEG PpIX PSilQ NPs upon a high reducing environment a release profile was performed in the presence of the reducing agent dithiothreitol (DTT) (**Figure 14**). The release plot shows that before the addition of DTT there is a slow release of compound **3** from the

nanoparticles; however, immediately after the addition of the reducing agent a fast release rate of photosensitizer was determined followed by a slow release rate and a plateau as an indication of a typical release profile. The half-life ($t_{1/2}$) for the release of compound **3** was ~23 h and ~18 h under reducing conditions for PpIX PSilQ and mPEG PpIX PSilQ NPs, respectively. Previous work in our group and others has shown that the use of disulfide bonds is a successful strategy to develop redox-responsive nanoparticles.

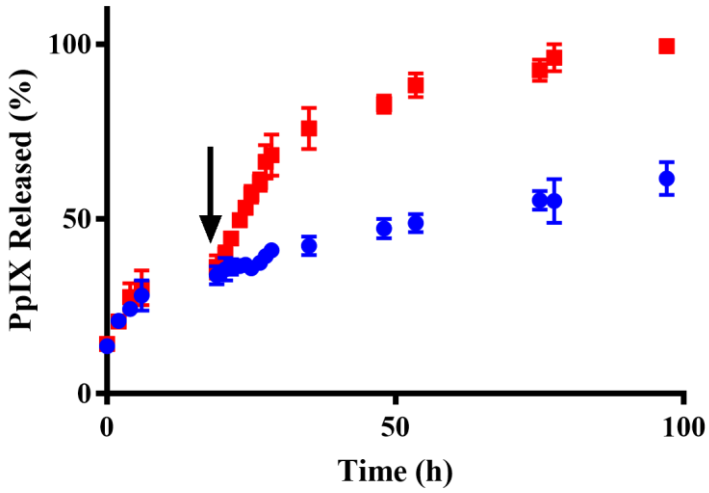


*Figure 14. Redox-responsive properties of PpIX PSilQ NPs in the presence of the reducing agent DTT. Two samples were used. One sample was kept as a control (blue circles) while the other sample was exposed to 10 mM DTT. The DTT addition is indicated by the black arrow. After the addition, a clear burst release was observed before a plateau equal to the release of the control sample.*

### *2.3.3. Study internalization of multifunctional PpIX PSilQ NPs in vitro.*

To evaluate the interaction of PpIX PSilQ NPs with (TNBC) cells, we studied the uptake of the nanoparticles by using fluorescence-activated cell sorting (FACS) flow cytometry and confocal microscopy in MDA-MB-231 cell line (**Figure 15**). FACS shows that both PpIX PSilQ and mPEG PpIX PSilQ NPs are internalized by MDA-MB-

231 cells after of incubation with a percentage of fluorescence for positive cells of 26% and 62%, respectively. The difference on the internalization could be due to the highly negative surface charge associated with the PpIX PSilQ NPs (-37 mV).[60,61] Confocal microscopy was performed on both the PpIX PSilQ NPs (Figure 15 B.) and mPEG PpIX PSilQ NPs (Figure 15 A.) to qualitatively determine the cellular uptake of the particles in the triple negative breast cancer cell line MDA-MB-231. The overlapped confocal micrographs of the red and DIC channels confirm the internalization of PpIX PSilQ NPs.

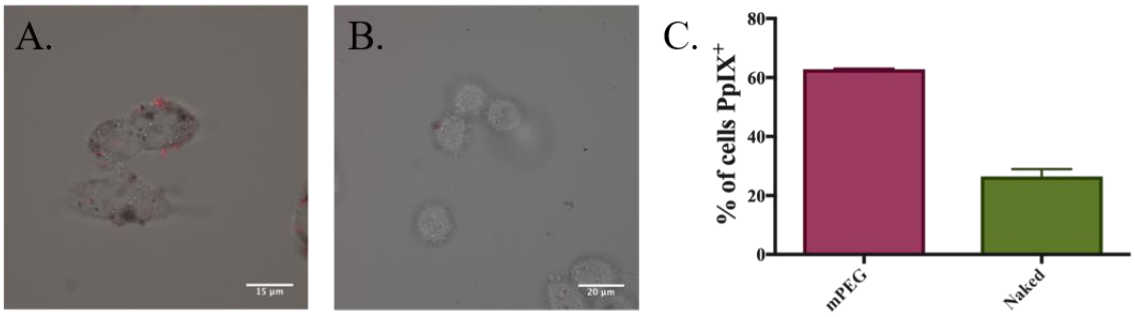


*Figure 15. Interaction of PSilQ NPs with MDA-MB-231 cells. Confocal microscopy was used to qualitatively determine the cellular uptake of mPEG PpIX PSilQ NPs (A.) and PpIX PSilQ NPs (B.) C. FACS was used to determine the internalization of PpIX PSilQ and mPEG PpIX PSilQ NPs. Confocal microscopy of show the uptake inside the cells.*

### *2.3.4. Phototoxicity of multifunctional PpIX PSilQ NPs.*

To study the phototoxicity of PpIX PSilQ and PEG-PpIX NPs, the following human breast cancer cell lines were selected: MDA-MB-231, MDA-MB-453, and MCF-7. Also, normal MCF-10a mammary cells were evaluated for comparison.[39,115] MDA-MB-231 and MDA-MB-453 are aggressive forms of breast cancer that are negative for both hormone receptors and do not overexpress human epidermal growth factor 2 (HER2); qualifying them as triple negative breast cancer (TNBC).[11] MDA-MB-231 also

does not produce claudin, a tight junction forming protein, resulting in a limited response to chemotherapy,[12,116], therefore, requiring alternative treatments such as PDT to be used.

The breast cancer cells were irradiated with red light (620-630 nm) using a LED light source for a total fluence of 90 J/cm$^2$. The $IC_{50}$ for the phototoxic outcome was calculated using graphpad. $IC_{50}$ values in the presence of PpIX PSilQ NPs for MDA-MB-231, MDA-MB-453 and MCF-7 of 0.79, 0.90 and 4.01 μM were obtained, respectively (**Table 1**). In a similar way, $IC_{50}$ values in the presence of PEG-PpIX PSilQ NPs for MDA-MB-231, MDA-MB-453 and MCF-7 of 0.90, 1.92 and 4.35 μM were calculated, respectively. A similar trend was observed for both materials where the TNBC lines are more susceptible to the phototoxic effect than the MCF7. Previous reports have shown that TNBC can be easily killed using PDT, which makes this approach attactive to treat this type of breast cancer. Control experiments using PpIX under the same experimental conditions and light exposure used for the nanoparticles showed $IC_{50}$ for MDA-MB-231, MDA-MB-453, and MCF-7 of 2.44, 0.29 and >5.00 μM were calculated, respectively. These results demonstrated that the PpIX PSilQ NPs are more efficient to deliver PpIX inside the cells. It is well-established that aggregation of PpIX is one of the main issues for its application as PDT agent.

We also evaluated the performance of both PpIX PSilQ platforms in the normal breast cell line MCF-10a. The IC50 values after irradiation with red light (620-630 nm; 90 J/cm$^2$) are 1.27 and 2.40 μM for PpIX PSilQ and mPEG PpIX PSilQ NPs, respectively. The PEG-PpIX PSilQ NPs showed three- and two-fold higher phototoxicity toward TNBC cells. The MCF-10a cell line should have a lower reducing environment as

compared to the TNBC cell lines.[71,81,90,117] The lower reducing environment is caused by a decrease in metabolism, meaning the cells won't take up NPs as readily nor degrade them inside the cell as well as TNBC cell lines. Therefore, the toxicity in the MCF-10a is expected to be lower than that of the MDA-MB-231 and MDA-MB-435.

*Table 1. $IC_{50}$ Values for PpIX PSilQ NPs and mPEG PpIX PSilQ NPs after irradiation*

| Cell Line | PpIX PSilQ NPs (D) | PpIX PSilQ NPs (L) | mPEG PpIX PSilQ NPs (D) | mPEG PpIX PSilQ NPs (L) | PpIX (D) | PpIX (L) |
|---|---|---|---|---|---|---|
| MDA-MB-231 | 1.80 | 0.79 | 2.49 | 0.90 | > 5.00 | 2.44 |
| MCF-7 | > 5.00 | 4.01 | > 5.00 | 4.35 | > 5.00 | > 5.00 |
| MDA-MB-453 | 2.05 | 0.90 | 4.85 | 0.84 | > 5.00 | 0.964 |
| MCF-10a | > 5.00 | 1.27 | > 5.00 | 2.40 | > 5.00 | 3.30 |

### *2.3.5. ROS, singlet oxygen and mechanisms of cell death PpIX PSilQ NPs.*

To study the role of ROS and singlet oxygen on the PDT process at cellular level we used dichlorofluorescein diacetate (DCF-DA) and SOSG assays. It has been reported that cell proliferation and differentiation could be promoted by a moderate increase in intracellular ROS, whereas the excessively elevated intracellular ROS can destroy cellular structure directly causing necrosis and apoptosis of cancer cells. Therefore, we studied the intracellular generation of ROS in MDA-MB-231 cells with PpIX PSilQ and mPEG PpIX PSilQ NPs. The generation of ROSs in vitro was quantitatively evaluated using cell-permeant DCF-DA. This molecule is a chemically reduced form of fluorescein used as an indicator for ROS in cells. Upon cleavage of the acetate groups by ROS the nonfluorescent DCF-DA is converted to the highly fluorescent 2',7'-dichlorofluorescein.

MDA-MB-231 cells were incubated with DCF-DA and irradiated in the presence of PpIX PSilQ and mPEG PpIX PSilQ NPs with red light (620–630 nm; 30 J/cm$^2$). The results clearly showed higher amount of positive cells for the samples containing NPs and irradiated. PpIX under the conditions evaluated in this experiment did not show that high amount of ROS generation (**Figure 16**). These results confirm the participation of ROS on the PDT process to kill MDA-MB-231.

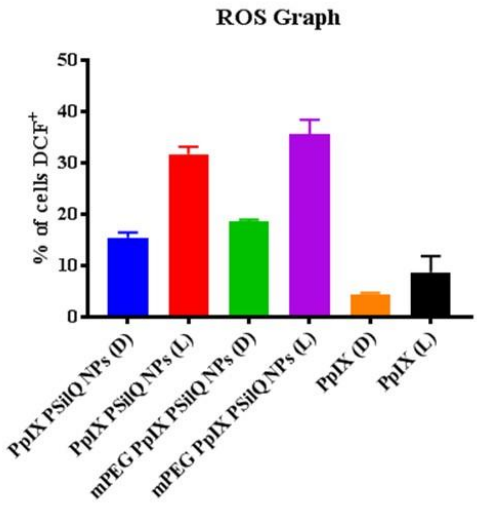


*Figure 16. Intracellular ROS was qualitatively determined using dichlorofluorescein diacetate (DCF-DA). DCF-DA reacts with ROS to restore fluorescence to the FITC moiety. The PpIX PSilQ NPs and mPEG PpIX PSilQ NPs both showed a significant increase in FITC fluorescence after irradiation. PpIX showed limited fluorescence both before and after irradiation.*

It has been reported that apoptosis or necrosis or a combination of the two is the mechanism of PDT in killing cancer cells. As compared to apoptosis necrosis breaks down the integrity of the cell plasma membrane and leads to a higher level of cell damage. Usually, high doses of PDT (such as high concentration of photosensitizer or light power) will be needed to induce necrosis in cancer cells, which will result in additional damage to the surrounding healthy tissues. To determine whether necrosis

and/or apoptosis was the main mechanism of PDT using PpIX PSilQ and mPEG PpIX PSilQ NPs in MDA-MB-231 cells, we used the Annexin V assay. The appearance of phosphatidylserine residues in the surface of the cell is an early event in apoptosis. Annexin V has a strong affinity for phosphatidylserine and it is used as a probe for detecting apoptosis. MDA-MB-231 cells were incubated in the presence of PpIX PSilQ and mPEG PpIX PSilQ NPs and irradiated with red light (620–630 nm; 30 J/cm$^2$) as described in the experimental protocol. Using flow cytometry, treated MDA-MB-231 cell populations were sorted by early apoptotic, apoptotic and necrotic cells (**Figure 17**). Control MDA-MB-231 cells and cells incubated with PpIX under dark conditions showed a very low percentage < 4.0% of positive cells for any of the populations. At the concentration evaluated in this experiment (2 uM), the presence of PSilQ NPs under dark conditions produced some toxic effect increasing the amount of positive apoptotic and necrotic cells in 9.1-7.2% and 7.3-6.3%, respectively. Nevertheless, after irradiation, a two-fold enhancement for apoptotic and necrotic cells was observed. Apoptotic cells increased in 15.0 and 15.3% for PpIX PSilQ and mPEG PpIX PSilQ NPs, respectively. In the case of necrotic cells, an increase of 15.0 and 17.7% was determined. These results show that for the PDT treatment with the PpIX PSilQ platform both mechanisms, necrosis, and apoptosis are relevant.

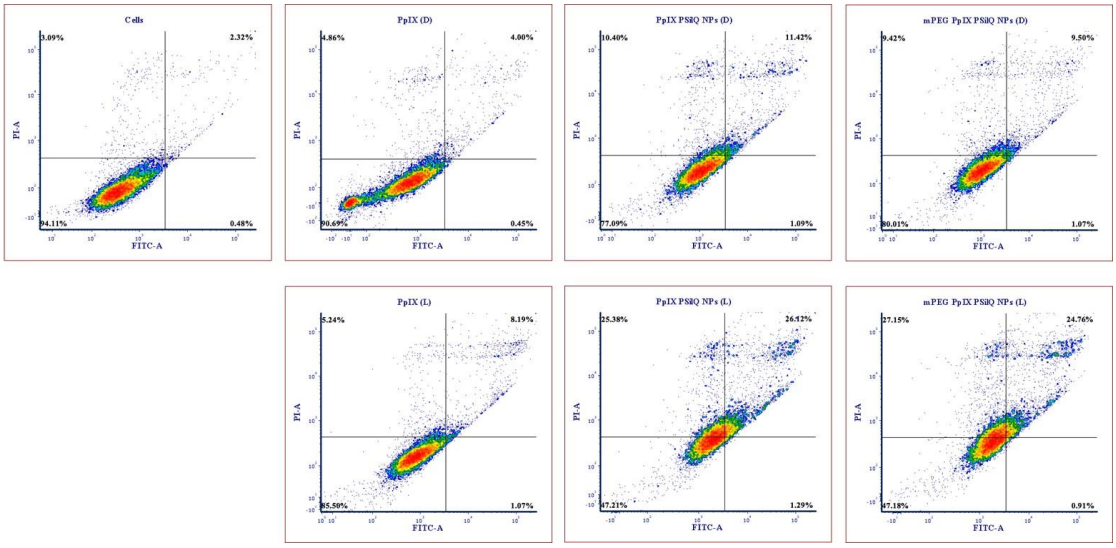


*Figure 17. An apoptosis assay was performed to determine the different killing mechanisms associated with the PpIX PSilQ NP platform. There was an increase in apoptotic death when PpIX PSilQ NPs and mPEG PpIX PSilQ NPs were used when compared to PpIX used as a small molecule.*

### *2.3.6. Investigate in vivo performance of multifunctional PpIX PSilQ NPs using a xenograft mouse model.*

A major drawback of PDT for cancer treatment deals with the inability to deliver a high concentration of PS to the tumor tissue. PSs tend to be quickly excreted from the body due to their hydrophobic nature. We envision that PpIX PSilQ platform would overcome these limitations by their degradable design as well as their passive, through the enhanced permeation and retention effect (EPR), and active targeting properties. These targeting properties will increase the phototherapeutic efficacy of the nanoparticles due to the accumulation in the tumor tissue. Testing PpIX PSilQ NPs and showing their ability to degrade while delivering a high payload of PS in a localized tumor environment would further advance the field of PDT and NP drug delivery systems.

### *2.3.7. Biodistribution and toxicity of mPEG PpIX PSilQ NPs in vivo.*

The maximum tolerated dose (MTD) in fully immuno-competent C57/BL mice was evaluated using different doses of NIR PEG PpIX PSilQ NPs (20, 40, and 60 mg/Kg) intravenously injected. The three experimental groups (n=3) were tested for a period of 10 days. During this time, there were no adverse side effects nor weight loss observed (Figure 8). These results showed that mPEG PpIX PSilQ NPs can be i.v. administered up to 60 mg/Kg without apparent signs of toxic effect in the short term.

The accumulation and elimination of mPEG PpIX PSilQ NPs was followed using the IVIS imaging system for up to 72 h. By analyzing the abdominal region of the mice with different doses of nanoparticles, it was determined that the maximum luminescence is detected around 24 h, followed by a decrease until the values are similar to the control group. Interestingly, some of the luminescence appeared in the bladder region as possible indication that the nanoparticles may be degraded and excreted by the renal excretion pathway.

Ten days post injection the mice were sacrificed; liver, lungs, kidneys, spleen, and heart were harvested and imaged. For the doses tested in this experiment, liver showed the highest luminescent followed by lung and kidneys (**Figure 18**) It is important to remember that the luminescent detected by IVIS system is associated to the NIR dye. Therefore, to find whether the biodistribution determined by IVIS using the NIR dye is similar to the one for PpIX, we determined the total amount of PpIX in liver, lung, and kidneys. PpIX was extracted over a 24 h period from the liver, lung, and kidneys after homogenization in a methanol/perchloric acid solution (1:1 v/v). The PpIX fluorescence

was measured and, using a calibration curve, we determined the concentration of PpIX in the organs as seen in **Figure 18c**. The amount of PpIX molecules found in liver, lung, and kidneys for the three different doses of mPEG PpIX PSilQ NPs administered was within the range observed for the control group. The difference in biodistribution of the NIR signal and the PpIX can be explained by the rational design of the PSilQ platform. PpIX molecules are chemically attached to the PSilQ NPs through a disulfide bond that seems to be broken faster than the silica bond of the NIR-PEG polymer. A more rigorous pharmacokinetic study is necessary to confirm these findings.

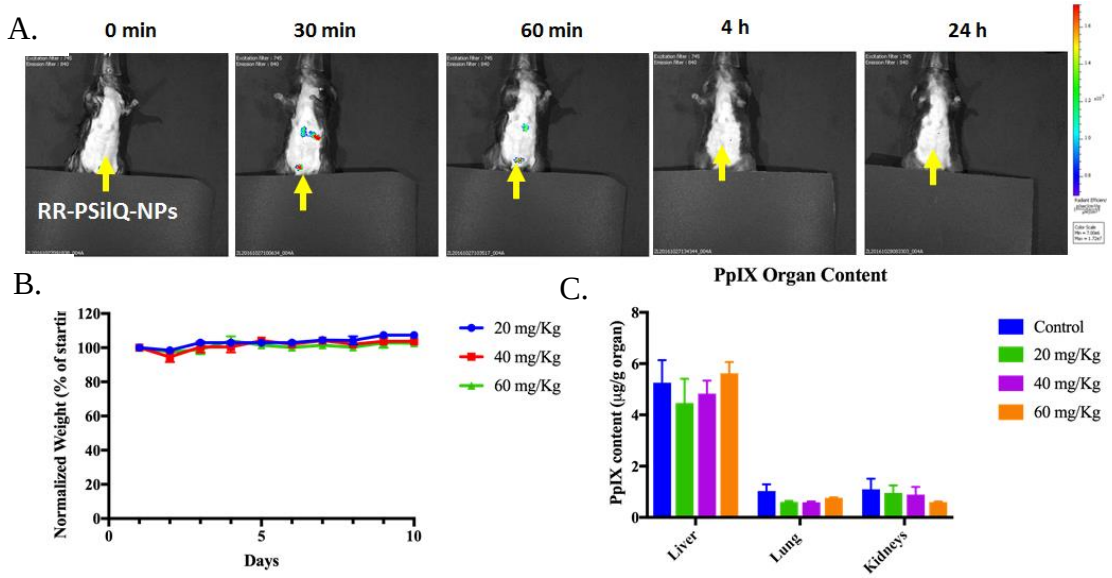


*Figure 18. A. Shows the accumulation of the NIR PpIX PSilQ NPs in the MTD studies. The arrow indicates the accumulation in the bladder at 30 and 60 min. The loss of fluorescence at 4 and 24 h show the complete degradation and excretion. B. The mouse weights were recorded with no weight change, proving the biocompatibility of the PSilQ platform. C. After the study organs were analyzed for PpIX content. There is not increase in PpIX in any of the groups when compared to the control.*

We further investigated the toxicity of the mPEG PpIX PSilQ platform in vivo by analyzing the tissue morphology of liver and kidneys post-injection with NIR PEG PpIX PSilQ NPs using hematoxylin and eosin (H&E) staining slides of the organs. The H&E

slides showed no signs of tissue degradation as an indication of the lack of toxicity for the mPEG PpIX PSilQ NPs. Confocal microscopy of those slides did not show the presence of PpIX in the red channel.

Overall, these data demonstrated that the mPEG PpIX PSilQ platform at doses below 60 mg/Kg is non-toxic, and can be quickly degraded and excreted in vivo, which are important features for moving silica-based delivery systems toward clinical applications. Interestingly, the cargo (PpIX) and the carrier (PSilQ NPs) seems to have different biodistribution due to chemistry of the platform.

### *2.3.8. Targeting and phototherapeutic efficacy against an orthotopic mice model of TNBC.*

To evaluate the targeting and therapeutic ability of the mPEG PpIX PSilQ platform against TNBC in vivo, we developed an orthotopic mice model using NSG mice and MDA-MB-231 TNBC cells. It has been shown that NSG mice is a reliable model to develop orthotopic TNBC model. First, the target ability of the platform was evaluated after i.v. injections of 40 mg/Kg of mPEG PpIX PSilQ NPs. After 4 days post administration, the mouse was sacrificed, and the organs were imaged with IVIS system. Fluorescence from the organs clearly showed a higher accumulation of the nanoparticles in the tumor (**Figure 19**). The accumulation of PpIX was confirmed by analyzing the amount of the molecule in the organs. These results showed that nanoparticles target the tumor tissue most likely through the EPR effect.

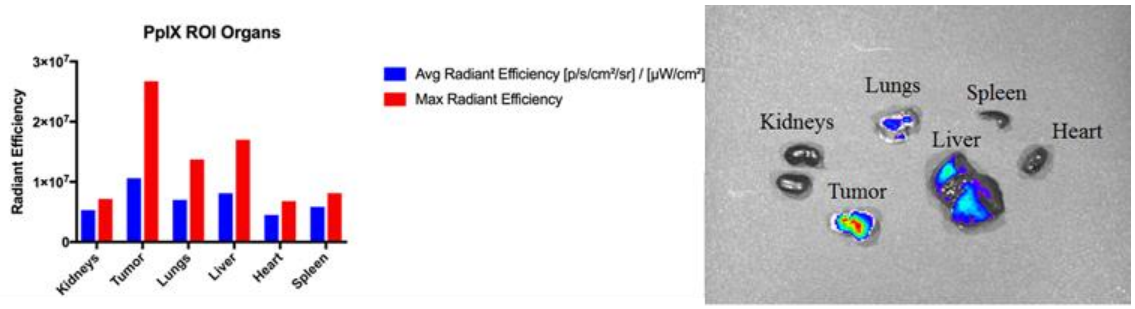


*Figure 19. After the targeting study, the organs were collected and imaged using the IVIS imaging instrument. A. is a graphical Representation of the fluorescence analyzed for each organ. B. Shows the intensity of fluorescence and the increase in the tumor over other major organs.*

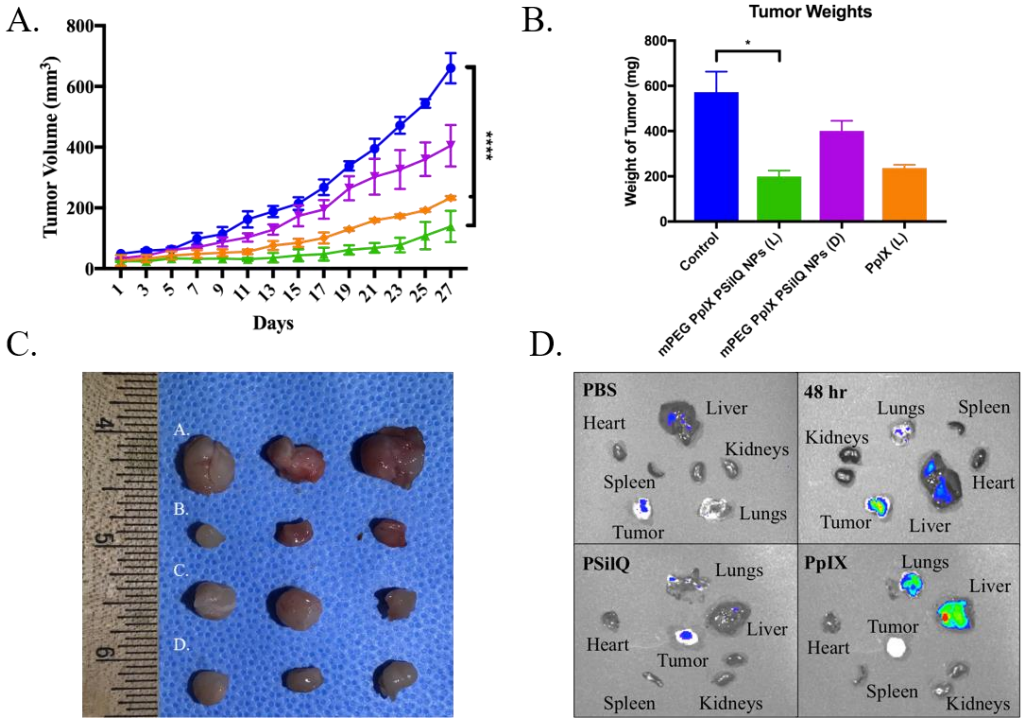


*Figure 20.* ***A.*** *Shows tumor volumes over the period of the phototherapeutic efficacy studies. The control (blue) clearly grows at a faster pace than the PpIX (yellow) with irradiation, with greatest effect on the tumor growth observed in the mPEG PpIX PSilQ NP (green) with red light irradiation. Limited tumor growth delay was observed in the mPEG PpIX PSilQ NP (purple) in dark.* ***B.*** *Tumor weights recorded after excision at the end of the study.* ***C.*** *Tumor comparison, groups are as follows A.is the PBS group, B. is the mPEG PpIX PSilQ NPs, C. is the mPEG PpIX PSilQ NP in dark, and D. is the PpIX.* ***D.*** *IVIS images of PpIX fluorescence in the major organs after the phototherapeutic efficacy study.*

The phototherapeutic efficacy of the mPEG PpIX PSilQ platform was tested in the orthotopic mice model. Four groups were evaluated; PBS, mPEG PpIX PSilQ NPs without light irradiation, PpIX and mPEG PpIX PSilQ NPs with light irradiation. Orthotopic MDA-MB-231 mice with tumors around 100 mm3 in size were iv injected with 40 mg/Kg of nanoparticles or the equivalent of PpIX molecules. The tumor was illuminated with red light (630 nm; J/cm2) three times 0, 4 and 24 hours after the dose of nanoparticles was administrated. This protocol was repeated for another two times. The growth of tumor was measured every other day using a caliper. The group with mPEG PpIX PSilQ NPs and light showed the highest tumor growth inhibition as an indication of the efficient delivery and phototherapy of PpIX in the tumor. PpIX molecule also depicted a decrease rate in tumor growth. The control group of mPEG PpIX PSilQ NPs in the absence of light showed a slight inhibition in tumor growth at the end of the experiment (**Figure 20**). Most likely due to the light environment from the vivarium. The images of H&E-stained tumor tissues revealed an obvious necrosis of major tumor cells in the PDT group, demonstrating the highly efficient antitumor potency of the PpIX PSilQ NPs. We also investigated the apoptotic effect of the mPEG PpIX PSilQ platform. TUNEL staining results demonstrated a great population of cell apoptosis in the tumor tissue of the mice with light irradiation, confirming the effectiveness of PpIX PSilQ NPs in killing TNBC cells *in vivo*. Overall the data show that mPEG PpIX PSilQ NPs efficiently reduce tumor growth in an orthotopic TNBC mouse model.

### *2.3.9. In Vivo toxicity evaluation of PpIX PSilQ nanoparticles in orthotopic mice model of TNBC.*

We then evaluated the in vivo biosafety of PpIX PSilQ NPs by comparing H&E staining images of major organs collected from mice injected nanoparticles and mice without any treatment. H&E staining showed no pathological change after nanoparticle injection. These results demonstrated that PSilQ NPs were safe for in vivo PDT applications.

Organs were imaged using the IVIS system (**Figure 20d**) It is clear even visually the accumulation of PpIX in organs like liver and spleen for the free PpIX group compared with the mPEG PpIX PSilQ NPs. Further analysis of PpIX content confirmed the highest accumulation of PpIX in the lungs and liver of the PpIX injection group. Accumulation of PpIX in human porphyrias can cause skin photosensitivity, biliary stones, hepatobiliary damage, and even liver failure. Because PpIX is a hydrophobic molecule, its disposition is by hepatic rather than renal excretion. Large amounts of PpIX are toxic to the liver and can cause cholestatic liver injury.

# CHAPTER 3
# COMBINATORIAL MESOPOROUS SILICA NANOPARTICLES FOR THE DELIVERY OF A PHOTOSENSITIZER (CHLORIN E6) AND CHEMOTHERAPEUTIC (CISPLATIN) IN TREATMENT OF TRIPLE NEGATIVE BREAST CANCER

## 3.1. Introduction to Project.

Triple negative breast cancer is associated with the highest mortality rate and highest rate of recurrence of all breast cancers requiring a new approach for treatment. The combination of photodynamic therapy along with chemotherapy has shown to overcome resistance to chemotherapy and effectively improve the anticancer activity by combining different cell death mechanisms. The difficulty in delivering both therapeutics simultaneously can be overcome by using nanoparticle delivery systems. One delivery system that has been used previously is a mesoporous silica nanoparticle (MSN). Here we report the synthesis and evaluation of phototherapeutic effect of PS Chlorin e6 combined with chemotherapy drug cisplatin in MSN platform for the simultaneous delivery of Ce6 and cisplatin for the improved therapy of TNBC.

We have successfully synthesized MSN loaded with Ce6 and cisplatin, where the Ce6 loading was determined to be 3.23 μg/mg and the cisPt content was determined to be 12.2 % (wt./wt.) and the MSNs were further functionalized with PEG to afford mPEG-Ce6-cisPt-MSN. We have further determined the cellular uptake of mPEG-Ce6-cisPt-MSN through confocal microscopy and flow cytometry in the TNBC cells MDA-MB-231. Phototoxicity was also performed with mPEG-Ce6-cisPt-MSN in TNBC cell lines MDA-MB-231, HCC-70, MDA-MB-453, and the murine TNBC cells 4T1. The combination effect of cisPt was determined by comparing toxicity with mPEG-Ce6-MSN

where a greater toxicity was observed when irradiated in comparison to the dark control when both Ce6 and cisPt were present in MSNs. Furthermore, the phototherapeutic efficacy of the mPEG-Ce6-cisPt-MSN was determined in an orthotopic TNBC mice.

## 3.2. Materials and Methods.

### *3.2.1. Materials.*

Chlorin e6 was generously provided as a gift by Dr. Vanderleigh Bagnato (Sao Paolo, Brazil), 1-ethyl-3-(3-dimethylaminopropyl) carbodiimide (EDC) was purchased from Oakwood Chemical. Hexadecyltrimethylammoinum bromide (CTAB), Tetraethyl orthosilicate (TEOS), (3-aminopropyl) trihydroxysilane (APTES). BD Pharmingen™ Annexin V-FITC Apoptosis Detection Kit was purchased from BD Biosciences. *In situ* Apoptosis Detection Kit (ab206386) was purchased from Abcam Co LTD (USA). The other reagents were purchased from Sigma-Aldrich and were used without further purification. Thermogravimetric analysis (TGA) was determined using a Mettler Toledo TGA/SDTA851 instrument (Mettler-Toledo AG Analytical, Schwersenbach, Switzerland) with a platinum pan and a heating rate of 1.0 °C/min from 25.0 to 800.0 °C under a nitrogen atmosphere. The sample was held at 800.0 °C for 3 h for complete calcination. A Raith 150 Field Emission Scanning Electron Microscope (SEM) (Raith America Inc., New York, NY, USA) was utilized to measure the particle size and shape of the materials. Dynamic light scattering (DLS) and ζ-potential measurements were carried out using a Malvern Instrument Zetasizer Nano (red laser 633 nm) (Malvern Instrument Ltd., Malvern, UK). The amount of chlorin e6 co-condensated in the MSNs

was quantified by UV-vis spectroscopy (Varian, Cary 300 Bio UV/vis spectrometer) (Varian, Sydney, Australia). The photophysical properties of Ce6 containing MSNs were determined using UV-vis and fluorescence (Varian, Cary Eclipse fluorescence). A BD LSRFortessa™ cell analyzer was used for the fluorescence-activated cell sorting (FACS) experiments. An Olympus Fluoview FV 1000 confocal fluorescence microscope system was used for the LCSM experiments. The IVIS Imaging system was used to determine the fluorescence of the NPs for the *in vivo* studies. LINCE light was used for irradiation for the *in vivo* studies. All tissue slides were visualized using an Olympus IX71 fluorescence microscope.

### *3.2.2. Experimental Methods.*

*3.2.2.1 Synthesis of Mesoporous Silica Chlorin e6 nanoparticles (Ce6-MSN).*

Chlorin e6 (40.2 μmol, 24 mg) was dissolved in 3 mL of DMSO. Aminopropyltriethoxy silane (APTES, 7.9 μmol, 140 μL) was added along with 1-ethyl-3-(3- dimethylaminopropyl) carbodiimide (EDC, 354.7 μmol, 68 mg) and 48 mg of N-Hydroxysuccinimide (NHS). This solution was left to stir for 2 h at room temperature. In a separate flask, cetrimonium bromide (CTAB, 3.64 mmol, 100 mg) was dissolved in 48 mL of nanopure $H_2O$. Mesitylene (5.0 μM, 700 μL) and NaOH (2 M, 350 μL) were added and left to stir for 1 h at 80 °C. When both reactions were complete, 940 uL of the chlorin e6 solution was added to the CTAB micelle solution, along with APTES (0.30 μmol, 69.7 μL), and tetraethyl orthosilicate (TEOS, 2.2 μmol, 500 μL). The solution was left to stir for 2 h at 80 $^{o}$C. At the completion of the 2 h, the nanoparticles were

centrifuged out of solution and washed three times with ethanol. The particles were subsequently washed for 48 h at 80 $^{o}$C in an acid bath. The acid bath consisted of a 10:1 ratio of Ce6-MSN(mg):MeOH(mL) and ~3.5 mL of concentrated HCl. After 24 h the particles were collected through centrifugation and a new acid bath was prepared. The particles were washed with ethanol and stored in ethanol under dark.

*3.2.2.2. Quantification of Chlorin e6 conjugated to MSN.*

Solutions of chlorin e6 were made at varying concentrations in DMSO and were analyzed using UV-Vis to acquire a calibration curve at 409 nm ($\varepsilon$ = 199,500 L/mol•cm). Subsequently, solutions of particles were made with varying concentrations and analyzed using the same UV-Vis. The absorption was plotted on the calibration curve to determine the concentration of the chlorin e6 in the MSN particles.

*3.2.2.3. Cisplatin prodrug synthesis.*

To synthesize dihydroxycisplatin(IV), diamminedichloroplatinum(II) (cisplatin (cisPt), 0.67 mmol, 200 mg) was added to nanopure water (9 mL) in a round-bottom flask, which was subsequently covered in aluminum foil to prevent photo-oxidation of the platinum substrate. To this solution, hydrogen peroxide (1.02 mL, 30%) was added. The solution was stirred at 70 °C for 5 h under nitrogen. Subsequently the reaction was cooled to room temperature and continued to stir overnight. The product was then washed one time with 10 mL cold nanopure water, followed by washing with 10 mL cold ethanol, and a final wash with 10 mL of ether. The product, a yellow solid, was

centrifuged and the supernatant was discarded. The dihydroxy cisplatin (IV) (0.372 mmol, 123.6 mg) was weighed into a scintillation vial and covered with aluminum foil. Dimethyl sulfoxide (DMSO, 4 mL) was added to the scintillation vial along with succinic anhydride (1.489 mmol, 148.9 mg). The solution was heated and stirred overnight at 70 °C. After that, the solution was dried in a lyophilizer. To obtain the cisplatin prodrug, the solid was washed one time with 10 mL cold acetone and the supernatant was discarded. The cisplatin prodrug solid was then dried, and the final product was characterized. Yield: 131.0 mg (66.1 wt%). $^{1}$H NMR (300 MHz, DMSO-D6, ppm): δ 2.43-2.39 (m, 2H), 2.31-2.23 (m, 2H); $^{13}$C NMR (300 MHz, DMSO-D6, ppm): δ 184.6 (C(O)OPt), 179.1 (COOH), 35.7 (PtOC=O$CH_2$), 34.7 ($CH_2$COOH); FT-IR ($cm^{-1}$): 3453 (O-H), 3263 (N-H).

*3.2.2.4. Cisplatin prodrug conjugation to Ce6-MSN.*

Cisplatin prodrug (47.0 μmol, 25 mg) was dissolved into 5 mL of DMSO. EDC (0.67 mmol, 104.3 mg) was added and allowed to stir for 10 minutes. A second solution of 100 mg of Ce6-MSN dispersed in 10 mL of DMSO was prepared and triethylamine (TEA, 43.7 μL) was added. The two solutions were then combined and stirred for 48 h at room temperature. Subsequently, the solution was centrifuged down and washed once with DMSO, and twice with EtOH to afford Ce6-cisPt-MSN. The supernatants were stored under dark for further analysis of cisplatin loading using AAS (12.5% wt./wt.).

*3.2.2.5. Synthesis of Methoxy-Poly(ethyleneglycol)-Amine (mPEG-$NH_2$).*

methoxy-PEG (mPEG) (1 mmol, 2 g) was heated to 90 ºC under vacuum overnight. To this polymer, dry THF (10 mL) was added along with methyl sulfonyl chloride (19.38 mmol, 1.5 mL). The solution was transferred onto an ice bath and DIPEA (3.0 mL) was added dropwise over a period of 30 min. After that, the solution was stirred overnight at room temperature. Nanopure water was added to dissolve any solid that has formed. Then, sodium bicarbonate solution (1 N, 2 mL) and sodium azide (1.5 g) were added to the solution. THF was removed by rotary evaporation. After that, the aqueous layer was refluxed overnight. The MeO-PEG-N3 product was extracted with dichloromethane (DCM, 5x15mL), and washed with brine solution. $MgSO_4$ was then used to completely dry the solution and filtered out before removal of the DCM by rotary evaporation. A Triphenyl phosphine (6.3 molar equivalents) was added to the product and dissolved in dry THF (12 mL) under $N_2$ atmosphere. The solution was stirred overnight. $H_2O$ (1.4 mL) was added and the solution was again stirred overnight. THF was removed by rotary evaporation and ~20mL of $H_2O$ was added. The precipitate was filtered out of solution, and the product was dried by rotary evaporation and placed in a lyophilizer. Yield: 1.28 g 64 %wt. $^1H$ NMR (300MHz, $CDCl_3$, ppm): δ (t, 6H, 2.65-3.01), (s, 3H, 3.31-3.41), (m, 180H, 3.55-3.65); We can add the 13C NMR data; FT-IR ($cm^{-1}$): 3401 (N-H), 2986 (C-H), 1665 (C-N), 1107 (C-O)

*3.2.2.6. Conjugation of mPEG to Ce6-MSN and Ce6-cisPt-MSN.*

mPEG-$NH_2$ (20.4 μmol, 50mg) was dissolved into 1mL of DMSO. 5.7 uL of TEA and triethoxysilylpropylisocyanate (TESPIC, 0.06 μmol, 15.2 μL) was added and allowed to stir for 4 h. 500 uL of this PEG solution was added to a solution of 50 mg of particles dispersed in 10 mL of ethanol and refluxed overnight at 90 $^{O}$C. The particles were then centrifuged out of solution, washed with ethanol and stored in ethanol under dark.

*3.2.2.7. Photophysical Characterization of mPEG-Ce6-MSN and mPEG-Ce6-cisPt-MSN.*

A Cary 300 Bio UV/vis (Varian, Sidney, Australia) and a Cary Eclipse fluorescence spectrometer (Varian, Sidney, Australia) were used to determine the absorption and fluorescence emission of mPEG-Ce6-MSN and mPEG-Ce6-cisPt-MSN. The particles were dispersed to 1 mg/mL concentrations to determine the loading of Ce6.

*3.2.2.8. In Vitro studies.*

MDA-MB-231 was used to determine phototoxicity as well as cellular uptake. MDA-MB-453, HCC-70, 4T1, and MCF-7 breast cancer cell lines (purchased from ATCC) were used for to determine phototoxicity. MDA-MB-231, MCF-7 cell lines were grown in RPMI 1640 media (10% FBS, 1% P/S) and phenol red pH indicator. MDA-MB-453, HCC-70, and 4T1, were grown in DMEM with 10% FBS, 1% P/S, 1% NEAA, 1% glutamax. All cell lines were purchased from ATCC.

*3.2.2.8.1. Cellular uptake analysis of mPEG-Ce6-MSN and mPEG-Ce6-cisPt-MSN using Confocal Microscopy.*

MDA-MB-231 triple negative breast cancer cells were seeded at a concentration of $5 \times 10^4$ cells/well on a glass cover slip in a 6 well plate with 2 mL of complete RPMI-1640 media. After 24 hours, the cells were inoculated with mPEG-Ce6-MSN and mPEG-Ce6-cisPt-MSN at a concentration of 50 μg/mL in RPMI-1640 media for 24 h. The cells were then washed with PBS and the glass cover slip was placed on a microscope slide for examination using an Olympus FluoView FV 1000 confocal microscopy instrument.

*3.2.2.8.2. Cellular uptake analysis of mPEG-Ce6-MSN and mPEG-Ce6-cisPt-MSN using Fluorescence-activated Cell Sorting (FACS).*

MDA-MB-231 triple negative breast cancer cells were seeded at a concentration $1 \times 10^5$ cells/well in a 6 well plate with 2 mL of complete RPMI-1640 media. The cells were allowed to attach for 24 h before inoculation with mPEG-Ce6-MSN and mPEG-Ce6-cisPt-MSN at a concentration of 50 ug/mL in RPMI-1640 media for 48 h. The cells were subsequently washed with PBS, trypsinized and collected through centrifugation. The cells were redispersed in 0.5 mL of RPMI-1640 complete media and 100 μL of trypan blue was added. The cells were analyzed using a BD LSR Fortessa flow cytometer instrument.

*3.2.2.8.3. Determination of in vitro ROS generation by mPEG-Ce6-MSN and mPEG-Ce6-cisPt-MSN.*

MDA-MB-231 cells were seeded in a 6-well plate at a concentration of $2 \times 10^5$ cells per well. The cells were allowed to attach for 24 h before inoculation with the mPEG-Ce6-MSN and mPEG-Ce6-cisPt-MSN. The cells were washed twice with PBS 24 h after inoculation. A 10 μM solution of dichlorofluorescein diacetate (DCF-DA) in serum free media was added for 30 min before being removed and the cells were washed with PBS. Fresh PBS was placed on the cells before irradiation with red light for 5 min at 24.5 mW/cm$^2$ (30 J/cm$^2$). The PBS was removed and stored. The cells were then trypsinized and centrifuged down along with the PBS stored from the irradiation. The cells were resuspended in 500 μL of serum free media and were analyzed using a BD LSR Fortessa flow cytometer instrument.

*3.2.2.8.4. Evaluation of phototoxicity of mPEG-Ce6-MSN and mPEG-Ce6-cisPt-MSN.*

MDA-MB-231, MDA-MB-453, HCC-70, and MCF-7 were seeded at a concentration of 5000 cells/well while 4T1 was seeded at a concentration of 500 cells/well. The cells were then incubated for 24 h. The media was removed and replaced with media containing mPEG-Ce6-MSN and mPEG-Ce6-cisPt-MSN at Ce6 concentrations ranging from 0.05-2 μM. The cells were inoculated for 24 h. Media was removed, and the cells were washed twice with PBS immediately followed by irradiation. Irradiation was performed with only PBS present at 620-630 nm light (14 mW/cm$^2$). The PBS was then removed, and media was placed on the cells for 24 hrs. 20 μL of Cell Titer

was added to each well and the plate was read after 3 hrs. The absorbance was plotted to yield the viability.

*3.2.2.9. In Vivo Studies.*

*3.2.2.9.1. Phototherapeutic efficacy of mPEG-Ce6-cisPt-MSN against an orthotopic mice model of TNBC.*

An orthotopic xenograft mouse model was used to determine the phototherapeutic efficacy. The mice (NOD SKID gamma, NSG) were injected with $5x10^5$ cells (100 μL of 1:1 growth factor reduced matrigel/PBS) into the mammary fat pad. Once the tumor reached ~100 $mm^3$ $\left(\frac{l \times w^2}{2}\right)$, the mice were randomly divided into the following groups (n=3): phosphate buffer solution (PBS), and mPEG-Ce6-cisPt-MSN with red light. The treatment consisted of total 5 injections in alternating eyes (*r.o.*) with an interval of four days between injections. Following each injection, there were three irradiations at 24 hr, 30 hr, and 48 hr post injection with red light (125 $mW/cm^2$, 12 min, 90 $J/cm^2$).[29] The irradiation conditions were performed to prevent the formation of hypoxic environment. The tumor sizes were monitored using a digital caliper every other day until 7 days after the final injection when the mice were sacrificed. Once the mice had been sacrificed blood was collected, the tumor was excised, weighed and the tumor and all major organs were collected and fixed for further studies.

*3.2.2.9.2. Hematoxylin and eosin (H&E) staining for toxicity evaluation.*

Tumors and major organs were fixed using a buffered 10% formalin solution for 24 h before being transferred to ethanol. The organs were paraffin-embedded, sectioned

(4 μm thick), and stained with H&E. Histopathological changes were observed using a fluorescent microscope (IX71, Olympus).

*3.2.2.9.3. Apoptosis staining of tumor tissue.*

Parafin-embedded tumor tissue (10 μm thick) was stained using the Abcam Co LTD. (USA) "*In situ* Apoptosis Detection Kit (ab206386)" as per manufacturer's instructions. The staining was observed using a fluorescent microscope (IX71, Olympus).

## 3.3. Results and Discussions.

### *3.3.1. Synthesis and characterization of mPEG-Ce6-MSN and mPEG-Ce6-cisPt-MSN.*

*3.3.1.1. Synthesis of mPEG-Ce6-MSN and mPEG-Ce6-cisPt-MSN.*

Chlorin e6 was covalently attached to 3-aminopropyltriethoxysilane (APTES) through the utilization of carbodiimide chemistry. The reaction proceeded through the use of 1-ethyl-3-(3-dimethylaminopropyl)carbodiimide (EDC) and N-hydroxysuccinimide (NHS). The carboxylic acid groups on Ce6 first reacted with the EDC to form a highly reactive product, which reacted further with NHS to form a succinimide ester. The succinimide group is a good leaving group and therefore activated the carboxylic acid group. APTES was added to displace the succinimide ester and form an amide bond between the APTES and Ce6. The Ce6 silane derivative was added during MSN synthesis. The Ce6-MSN was then synthesized through a surfactant template approach. The co-condensation of tetraethylorthosilicate (TEOS), additional APTES and the silane derivative of Ce6 in the presence of sodium hydroxide (NaOH), mesitylene and cetyltrimethylammonium bromide (CTAB) formed the desired Ce6-MSN. Mesitylene

was used as a pore expander, while CTAB was used as the surfactant. The highly organic nature of Ce6 allowed for it to incorporate itself inside the micelles formed by CTAB where it condensated inside the porous structure of the MSN. The CTAB was removed with a subsequent acid wash. Once CTAB had been removed the surface of the MSN was reacted with the cisplatin prodrug.

The prodrug was synthesized according to procedures previously found in literature and can be seen in **Figure 21**. Diaminedichloroplatinum (cisplatin, cisPt) was oxidized with $H_2O_2$ where Pt(II) is oxidized to Pt(IV) through the addition of two axial hydroxyl groups forming dihydroxycisplatin(IV). The dihydroxycisplatin(IV) was subsequently reacted with an excess succinic anhydride to form the cisPt prodrug with two carboxylic acid groups that could be used for covalent attachment to the Ce6-MSN. The cisPt prodrug was conjugated to the MSN through an amide bond between the amines on the MSN and the carboxylic acid groups on the prodrug to form Ce6-cisPt-MSN. Lastly, methoxy-poly(ethylene)glycol-amine (mPEG, 2KDa) was functionalized on the MSN surface. The mPEG-amine was first reacted with 3-(triethoxysilyl)propyl isocyanate to form a urea bond between the amine and isocyanate groups. The mPEG-silane derivative is subsequently added to Ce6-MSN and Ce6-cisPt-MSN where it was condensated onto the surface. The final MSN products, mPEG-Ce6-MSN and mPEG-Ce6-cisPt-MSN were then recovered through centrifugation and stored in ethanol.

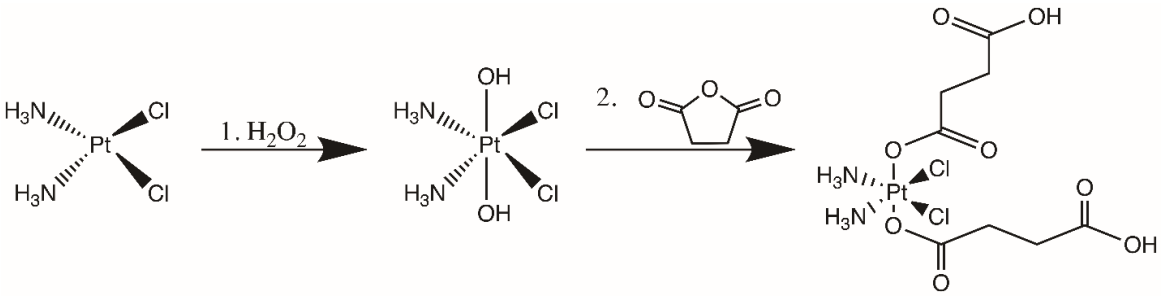


*Figure 21. The synthesis of the cisPt prodrug starts with the oxidation of platinum from Pt(II) to Pt(IV) using hydrogen pyroxide. 2. Succinic anhydride is opened and one carboxy group coordinates to Pt while the other is used as a synthetic handle to conjugate the cisPt prodrug to form Ce6 cisPt MSN.*

*3.3.1.2. Physicochemical characterization of mPEG-Ce6-MSN and mPEG-Ce6-cisPt-MSN.*

The Ce6-MSN and Ce6-cisPt-MSN were characterized for size, morphology and organic content using scanning electron microscopy (SEM), dynamic light scattering (DLS), zeta potential, and thermogravimetric analysis (TGA) and are described in detail in Table 2. The diameter of the MSNs prior to the addition of PEG was determined to be 131 ± 15 nm through SEM. However, the hydrodynamic diameter ($D_h$) was observed to be much larger by DLS with a $D_h$ of 590 ± 22 nm for the Ce6-MSN and a $D_h$ of 510 ± 34 for Ce6-cisPt-MSN in 1 mM PBS (pH 7.4). The increase in diameter is evident of aggregation that is occurring between the particles in PBS solution. The aggregation under physiological conditions can be attributed to the organic nature of the surface of the MSNs. The aminopropyl groups mask the more hydrophilic silanol groups that are found on the surface of MSNs. Zeta potential measurements proved the presence of amine groups on the surface with charges of +12 ± 0.5 mV for Ce6-MSN. Primary amine groups have a pKa of ~10.4 and therefore would be protonated in 1 mM PBS and were responsible for the positive surface charge. The cationic amine groups were reacted with

the cisPt prodrug which resulted in a decrease in surface charge to -8 ± 0.7 mV for Ce6-cisPt-MSN. The change in surface charge is due to removing the catioinic properties of the amine by reacting them with the prodrug and from the free, non-reacted carboxylate groups on the prodrug. The pKa of a carboxylic acid is ~4.6, and therefore would be deprontonated at pH 7.4. Upon the addition of mPEG to the surface, there was further aggregation confirmed by DLS with $D_h$ of 740 ± 67 nm and 850 ± 31 nm for mPEG-Ce6-MSN and mPEG-Ce6-cisPt-MSN respectively. The increased aggregation was determined to be caused by the decrease in charge-charge repulsion between particles. The decrease in surface charge was confirmed by zeta potential measurements with surface charges of +0.04 ± 0.06 mV for mPEG-Ce6-MSN and -0.7 ± 0.3 mV for mPEG-Ce6-cisPt-MSN. The only cause of this surface charge is the conjugation of mPEG on the surface of the MSN. The neutralization of surface charge is important to prevent the MPS from identifying the MSN during circulation inside the body. Highly negative charges avoid detection in the body, whereas strongly negative charges are less likely to undergo cellular uptake.[118] SEM was then performed to ensure there was no size or morphological changes after the addition of mPEG. **Figure 22** shows the spherical characteristics of MSNs and a size of ~200 nm.

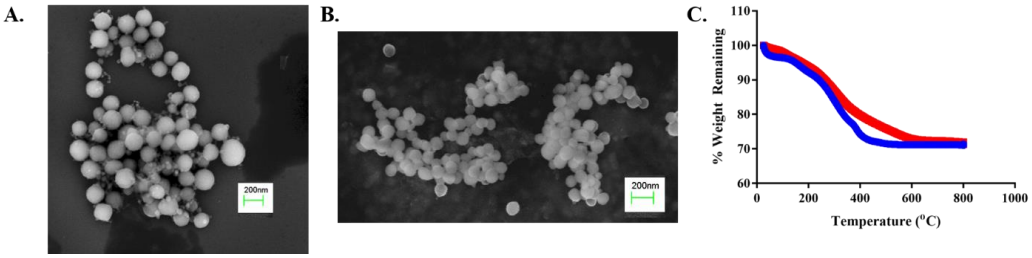


*Figure 22. SEM images of mPEG Ce6 MSN (**A.**) and mPEG Ce6 cisPt MSN (**B.**). **C.** TGA plot for mPEG Ce6 MSN (blue) and mPEG Ce6 cisPt MSN (red).*

The organic content present on the MSN was determined through TGA. The organic content was separated into three temperature ranges. The first range of 25-150 °C was attributed to the removal of solvent and was discarded. The second and third ranges of 150-350 °C and 350-800 °C were attributed to the aliphatic compounds and aromatic compounds, respectively. The materials expected to contribute to the aliphatic regions were the aminopropyl groups, the cisPt prodrug, and the mPEG. mPEG was expected to contribute the most due to the size of the polymer. The chlorin e6 was primarily responsible for the aromatic content and the high temperature was used to guarantee all of the Ce6 was removed from inside the pores. The Ce6-MSN had an organic content of 5.3 % in the aliphatic range and an 18.5 % organic content in the aromatic range. The organic content increased in the aliphatic region to 9.0 % and decreased in the aromatic range to 12.9 % for the Ce6-cisPt-MSN. These changes were to be expected with the addition of the cisPt prodrug and the two acid groups, which inherently decreased the wt. % of the Ce6 present. Platinum is not removed during TGA and was therefore responsible for the overall organic content decrease between Ce6-MSN and Ce6-cisPt-MSN. Once again, the organic wt. % expectedly changed with the addition of mPEG to the surface, with the mPEG-Ce6-MSN having 11.1 % organic material in the aliphatic range and 11.3 % organic material in aromatic while the mPEG-Ce6-cisPt-MSN had an 11.0 % organic content in the aliphatic range and an 11.7 % organic content in the aromatic range. The observed changes in the aliphatic material confirmed the addition of the mPEG on the surface of the MSN.

*Table 2. Characterization table of Ce6-MSN, mPEG-Ce6-MSN, Ce6-cisPt-MSN and mPEG-Ce6-cisP-MSN.*

| Material | Hydrodynamic Diameter (nm) | Zeta Potential (mV) | Organic content (%) | Ce6 Content (µg/mg) | Platinum Content (% wt/wt) |
|---|---|---|---|---|---|
| Ce6 MSN | 590 ± 22 | +12 ± 0.5 | 18.4 | 5.68 | N/A |
| mPEG Ce6 MSN | 740 ± 67 | +0.04 ± .06 | 21.2 | 5.35 | |
| Ce6 cisPt MSN | 510 ± 34 | -8 ± 0.7 | 21.9 | 3.43 | 12.2 |
| mPEG Ce6 cisPt MSN | 850 ± 31 | -0.7 ± 0.3 | 23.9 | 3.23 | 11.2 |

*3.3.1.3. Quantification of cisplatin loading in Ce6-MSN.*

The loading of cisplatin was determined through atomic absorption spectroscopy (AAS). A calibration curve at 265 nm was plotted and the supernatant was analyzed. The loading was determined to be 12.2 % wt./wt. of cisplatin prodrug with a loading efficiency of 48.8 %.

*3.3.1.4. Photophysical properties of Ce6 MSN and Ce6 cisPt MSN.*

The Ce6-MSN, Ce6-cisPt-MSN as well as the PEG derivatives all showed the standard absorption expected for Ce6. The soret band was observed at 404 nm (ε =

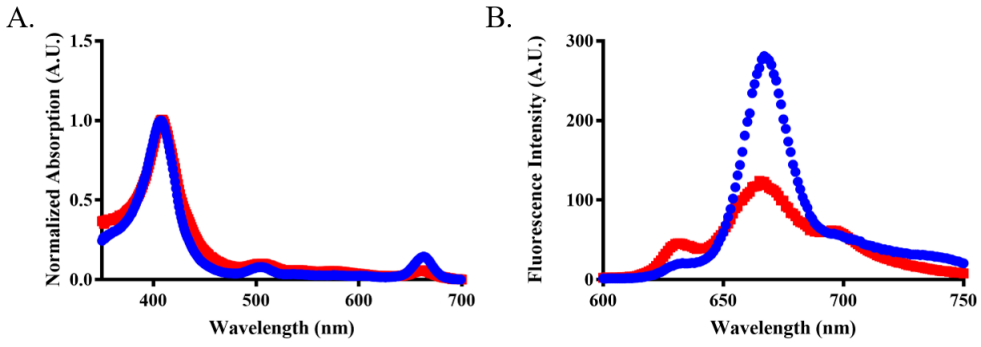


*Figure 23. The absorption (**A.**) and fluorescence (**B.**) spectra of mPEG-Ce6-MSN (blue) and mPEG-Ce6-cisPt-MSN (red).*

199,500 L/mol•cm), which was followed by the characteristic Q-bands. The increase in red light absorption at 668 nm is a primary reason chlorins are preferred over their counterpart porphyrin. The Ce6 loading was determined through UV-Vis spectroscopy (**Figure 23**). The soret band at 404 nm was used to determine the Ce6 content in the MSNs. The Ce6 loading was determined to be 5.68 μg/mg for the Ce6-MSN and 3.43 μg/mg for Ce6-cisPt-MSN. The Ce6 concentration changed a negligible amount upon the addition of mPEG and was observed to be 5.35 μg/mg for mPEG-Ce6-MSN and 3.23 μg/mg for mPEG-Ce6-cisPt-MSN. The characterized properties of Ce6-MSN, Ce6-cisPt-MSN, and their PEG derivatives is presented in **Table 2**.

### *3.3.2. In Vitro Studies.*

*3.3.2.1. Cellular uptake of nanoparticles in TNBC cell line MDA-MB-231.*

Cell line MDA-MB-231 is a triple negative breast cancer cell line. Cellular uptake studies were performed on MDA-MB-231 using flow cytometry and confocal microscopy. Due to the difficulty in visualizing the Ce6, fluorescein isothiocyanate was grafted to the surface of MSNs to ensure the MSNs could be observed. The flow cytometry samples were prepared in the presence of trypan blue to prevent fluorescence from any MSN that did not undergo complete cellular uptake. It is important for the MSN to be completely taken up by the cells to ensure release of active cisPt. The Pt(IV) complex is reduced by glutathione to become the active Pt(II) complex. The reduction is expected to occur rapidly due to the increased glutathione levels found in cancer cells. 20 % of cells were observed to have fluorescence due to FITC when analyzed showing adequate uptake to produce both a photodynamic and chemotherapeutic effect (**Figure**

**24a**). Confocal microscopy was able to show the FITC labeled MSNs undergoing complete cellular uptake wherein the nanoparticles were found inside of the cell membrane (**Figure 24b**). Once again this was important as complete cellular uptake is necessary for cisPt to be released.

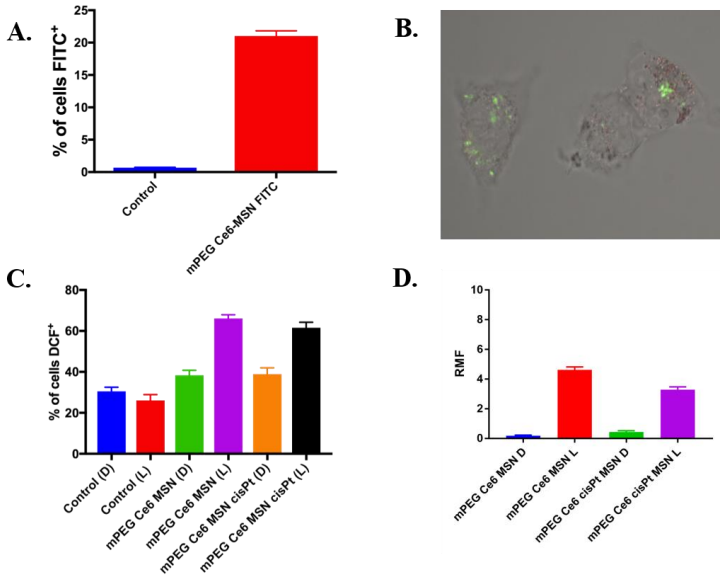


*Figure 24.* ***A.*** *Flow cytometry was used to show the cellular uptake of mPEG Ce6 FITC MSN. It was also confirmed through confocal microscopy (****B.****).* ***C.*** *The intracellular ROS was determined using a DCF-DA assay, where an increase in DCF cells is related to the increase in ROS production.* ***D.*** *The intracellular singlet oxygen was analyzed using SOSG. Again the increase in fluorescence is directly proportional to the amount of singlet oxygen that is produced inside the cell.*

### *3.3.2.2. Determination of intracellular ROS and singlet oxygen produced for mPEG-Ce6-MSN and mPEG-Ce6-cisPt-MSN.*

To study the role of ROS and singlet oxygen on the PDT process on a cellular level, we used dichlorofluorescein diacetate (DCF-DA) and SOSG assays. It has been reported that cell proliferation and differentiation could be promoted by a moderate increase in intracellular ROS, whereas an excessively elevated intracellular ROS can

destroy cellular structure directly causing necrosis and apoptosis of cancer cells. Therefore, we studied the intracellular generation of ROS in MDA-MB-231 cells by Ce6-MSNs. The generation of ROS *in vitro* was quantitatively evaluated using cell-permeant DCF-DA, which is a chemically reduced form of fluorescein used as an indicator for ROS in cells. Upon cleavage of the acetate groups by ROS the nonfluorescent DCF-DA is converted to the highly fluorescent 2',7'-dichlorofluorescein. MDA-MB-231 cells were incubated with DCF-DA and irradiated in the presence of mPEG-Ce6-MSN and mPEG-Ce6-cisPt-MSN with red light (620–630 nm; 30 J/cm$^2$). The results clearly showed higher amount of FITC fluorescent cells for the samples containing NPs after irradiation. These results confirm the participation of ROS on the PDT process to kill MDA-MB-231.

*3.3.2.3. Toxicity studies towards TNBC cell lines.*

The toxic effect of mPEG Ce6 MSN and mPEG Ce6 cisPt MSN was determined using three human TNBC cell lines (MDA-MB-231, MDA-MB-453, and HCC-70), one murine TNBC cell line (4T1) and one ER$^+$ cell line (MCF-7). The studies were performed in the same manner with cells having attached for 24 h before inoculation with Ce6 concentrations of 0.05-2 μM (2.4-94/7 μM cisPt) with irradiation 24 h post inoculation with 24.5 mW/cm$^2$ of 620-640 nm red light for 5 min (total radiance of 7.5 J/cm$^2$). Finally, toxicity was measured using Cell Titer©. The $IC_{50}$ values can be seen in **Table 3**. It was observed that mPEG Ce6 cisPt MSN had a lower $IC_{50}$ value of 0.42 μM and 0.05 μM than mPEG Ce6 MSN values of 0.47 μM and 0.15 μM for TNBC cell lines MDA-MB-231 and MDA-MB-453 respectively. In the cell line HCC-70, the $IC_{50}$ values were similar with 0.10 μM for mPEG Ce6 cisPt MSN and 0.06 μM for mPEG Ce6 MSN.

However, when the dark toxicity was compared to the light toxicity, there was a larger difference between the two, showing that there is a greater toxic effect after irradiation if both therapeutics were present.

*Table 3. $IC_{50}$ values for TNBC cells lines using mPEG Ce6 MSN and mPEG Ce6 cisPt MSN*

| Platform | MDA-MB-231 | MDA-MB-453 | HCC-70 | 4T1 | MCF-7 |
|---|---|---|---|---|---|
| mPEG Ce6 MSN (L) | 0.47 μM | 0.15 μM | 0.06 μM | 0.68 μM | 0.46 μM |
| mPEG Ce6 cisPt MSN (L) | 0.42 μM | 0.05 μM | 0.10μM | 0.88 μM | 0.22 μM |

### *3.3.3. In Vivo Phototherapeutic efficacy studies.*

The phototherapeutic efficacy was determined using an orthotopic model of TNBC cell line MDA-MB-231. Cells ($5\times10^5$) were dispersed in PBS and growth factor reduced matrigel (1:1 v/v). The matrigel was diluted due to a high viscosity. The cells were injected into the 4$^{th}$ mammary fat pad of the mouse. NOD SCID gamma mice were used to ensure there was no rejection of cells after injection. After injection, the tumor volume was monitored using a digital caliper every other day. Once the volume reached ~100 $mm^3$ the mice were grouped into a control which received an injection of 100 μL of PBS and a treatment groups which received an injection of 50 mg/Kg of mPEG Ce6 cisPt MSN dispersed in 100 μL of PBS. The concentration of MSN used was determined by a previous maximum tolerated dose study. The 1$^{st}$ irradiation (125 $mW/cm^2$, 12 min, 90 $J/cm^2$) was performed at 24 h post injection to allow for maximum accumulation in the tumor tissue. In the case of a high light dose with a strong photosensitizer an anaerobic environment can be produced, to ensure this didn't happen the 2$^{nd}$ and 3$^{rd}$ were performed at 30 and 48 h post injection. The mice received a total of 5 injections with four days

between each injection, followed by the same irradiation regiment. The tumor volumes were monitored until 7 days after the last injection. The mice were sacrificed at this point followed by the collection of blood, the tumor and major organs. The tumors were then weighed to determine the final effect of mPEG-Ce6-cisPt-MSN. Both the tumor volumes and the tumor weights confirmed the success of mPEG-Ce6-cisPt-MSN on the treatment of orthotopic model. The tumor volumes showed that through the first 15 days there was a negligible amount of growth by the tumor in the treatment group compared to control, which over doubled in size. The final tumor weights showed that the tumors from control group was twice as large as the treatment group. The tumor volume and the tumor weight are depicted in **Figure 25**.

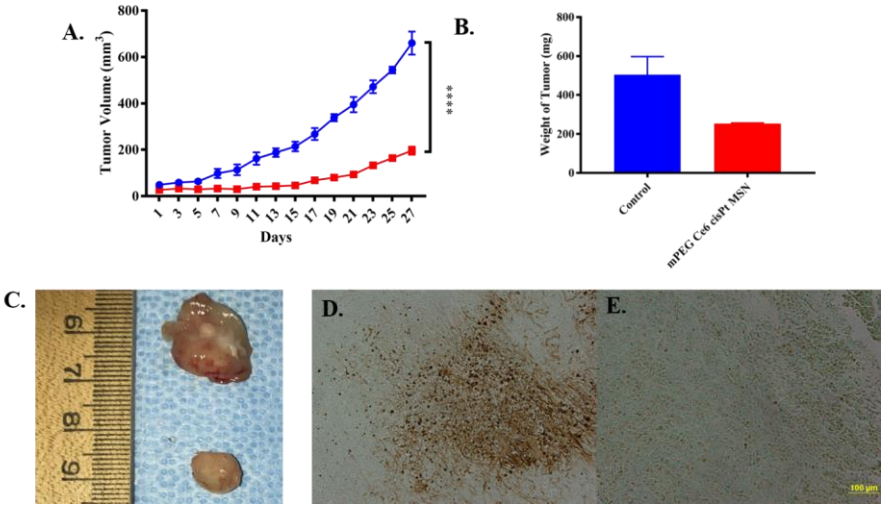


*Figure 25.* ***A.*** *Measured tumor volume for the control (blue) and the mPEG Ce6 cisPt MSN (red).* ***B.*** *Weights of the excised tumors.* ***C.*** *Images of tumor control (top) and mPEG Ce6 cisPt msn.* ***D-E.*** *Tumor tissue slides were stained to observe apoptosis. Terminal deoxynucleotidyl Transferase (TdT) is used to aid in staining apoptotic cells brown, while health cells will fluoresce green. The tumor tissue from the mPEG Ce6 cisPt MSN (D.) shows more apoptosis than that of the control group (E.).*

# CHAPTER 4
# MULTIFUNCTIONAL POLYSILSESQUIOXANE NANOPARTICLES FOR PHOTO-, CHEMO-, AND GENE THERAPY OF TRIPLE-NEGATIVE BREAST CANCER

## 4.1. Introduction to Project.

Multifunctional nanoparticles are attracting a lot of attention because of their ability to carry a wide variety of therapeutic agents. Such integrated nanoplatforms have been shown to be effective therapeutic options for cancer treatment. In this report, we successfully designed, fabricated, and applied a multifunctional polysilsesquioxane-based platform for the multimodal treatment using photo-, chemo- and gene therapy of highly aggressive triple-negative breast cancer cells. The platform that carries a photosensitizer (protoporphyrin IX), a therapuetic agent (curcumin) and siRNA

## 4.2. Materials and Methods.

Protoporphyrin IX (PpIX), Aerosol OT (AOT), 2',7'-dichlorodihydrofluorescein diacetate ($H_2$DCF-DA), and singlet oxygen sensor green (SOSG) were obtained from Thermo Fischer Scientific. 1-ethyl-3-(3-dimethylaminopropyl) carbodiimide (EDC) was purchased from Oakwood Chemical. Polyethylene imine (PEI, branched, MW 10kD) and methoxy-polyethyleneglycol-NHS (MeO-PEG-NHS, MW 2kD) was purchased from Alfa Aesar and creative PEGworks, respectively. n-butanol, dithiothreitol (DTT), 9,10-anthracene dipropionic acid (ADPA), ninhydrin and the rest of the chemicals used in this work were obtained from Sigma-Aldrich and used without any further purification unless otherwise noted. A homemade LED device emitting at 620-630 nm (24.5 mW/cm$^2$) was used for our *in vitro* experiments. Roswell Park Memorial Institute (RPMI 1640), fetal

bovine serum (FBS), MBEM, penicillin-streptomycin (pen-strep), phosphate buffer saline (PBS, 1X), trypsin were purchased from Cornings. CellTiter 96® AQueous Assay was obatined from Promega (Madison, WI, USA). Lysotracker green, endoplasmic reticulum tracker blue, and Hoechst 33342 were obtained from Life technologies (NY, USA). Double stranded DNA for cell internalization experiments and siRNA for GFP knockdown were provided by Dr. Kirill A. Afonin's laboratory in UNC at Charlotte.

### *4.2.1. Synthesis of RR-PpIX-PSilQ nanoparticles.*

The ligand used for RR-PpIX-PSilQ NPs was the same redox responsive silane ligand (**5**) from CHAPTER 2. The direct microemulsion method was used as the approach for the synthpesis of PpIX-based redox responsive PSilQ NPs (RR-PpIX-PSilQ NPs). Briefly, 0.22 g AOT (494.87 μmol) was added to 10 mL of nanopure water under gentle stirring for 30 min at room temperature, which gave a translucent solution. This was followed by the addition of 0.4 mL n-butanol. Only after the solution became clear, 0.1 mL cyclohexane (as the oil phase) was added. The final mixture was allowed to stir for 15 min to give a single phase transparent solution. To the above solution, ligand 5 (16 mg/mL;) was dissolved in 1:2 DMSO/DMF mixture (0.1mL) dropwise under continuous stirring at room temperature. In order to increase the rate at which condensation occured, 0.1 mL of aqueous ammonia (28 %) followed by 0.2 mL of an aqueous solution of NaOH (2 M) was added to the solution. The reaction mixture was allowed to stir for 48 h at room temperature. The nanoparticles were obtained by disrupting the micro-emulsion with an excess of acetone, which afforded the precipitation of the RR-PpIX-PSilQ NPs as a brown precipitate. The RR-PpIX-PSilQ NPs were collected by centrifugation (13K rpm

for 10 min) and washed sequentially with acetone, ethanol, and DMF to remove any unreacted reagents. The washed RR-PpIX-PSilQ NPs were stored in ethanol at 4 $^{0}$C. Curcumin was used a model drug for encapsulation into the hydrophobic core of the RR-PpIX-PSilQ NPs. To synthesize this material, 0.4 mL of curcumin solution (5 mg/mL in DMSO) was added to the oil-in-water micro-emulsion described above before the addition of the PpIX-based ligand (5). The final RR-PpIX-PSilQ(cur) NPs were collected by centrifugation and washed as described above. The supernatant and washing solutions were stored to quantify the loading of curcumin using UHPLC.

### *4.2.2. Modification of RR-PpIX-PSilQ(cur) nanoparticles with PEI polymer.*

To modify the surface of RR-PpIX-PSilQ(cur) NPs with PEI polymer (MW=10kD), 10 mg of RR-PpIX-PSilQ(cur) NPs were re-dispersed in 1 mL of nanopure water. PEI solution (5 mg, 20 mg/mL in EtOH) was added dropwise to the nanoparticle dispersion under gentle stirring at room temperature for 2 h. PEI-RR-PpIX-PSilQ(cur) NPs were collected by centrifugation (15K rpm for 10 min) and washed 2-3 times with ethanol to remove the excess of PEI. The amount of amine functional groups that were chemically available on the surface of PEI-RR-PpIX-PSilQ(cur) NPs were indirectly quantified using Kaiser's test.

### *4.2.3. Functionalization of PEI-RR-PpIX-PSilQ(cur) nanoparticles with PEG polymer.*

PEI-RR-PpIX-PSilQ(cur) NPs were further functionalized with PEG (MW=2kD) polymer. For this, 10 mg of PEI-RR-PpIX-PSilQ(cur) NPs were dispersed in 9 mL of ethanol. To this dispersion, ethanolic solution of of MeO-PEG-NHS (3 mg in 1 mL

ethanol) was added dropwise under stirring conditions. The reaction mixture was left to stir for 24 h at room temperature. The PEG-PEI-RR-PpIX-PSilQ(cur) NPs were collected by centrifugation (15K rpm for 10 min) and washed twice with ethanol to remove any unreacted MeO-PEG-NHS chains. The PEG-PEI-RR-PpIX-PSilQ(cur) NPs were redispersed and stored in ethanol.

### *4.2.4. Size and morphology analysis.*

The size and shape of the nanoparticles were measured using TEM (JEM-1230 TEM) operating at an accelerating voltage of 80 kV. The samples for TEM were prepared by dispersing the RR-PpIX-PSilQ NPs in aqueous solution, and then deposited on a carbon-coated copper grid and air dried for at least 24 h. Particle size distributions were calculated by ImageJ based on a sample of at least 50 particles from different images taken over different quartiles.

### *4.2.5. Dynamic light scattering and ζ potential measurements.*

The hydrodynamic diameter and ζ potential of the RR-PpIX-PSilQ NPs and subsequent modifications were assessed by DLS using Malvern Instrument Zetasizer Nano (red laser 633 nm). The equilibration time for the sample was set to 2 min, and three measurements taken on each sample. The measurements were performed on dilute dispersion (0.5 – 1.0 mg/mL) of NPs in either 1 mM PBS or complete cell media (cDMEM). Measurements were performed in triplicates, and the data is reported as average ± SD.

The short-term colloidal stability of RR-PpIX-PSilQ and RR-PpIX-PSilQ(cur) NPs was determined in the cDMEM supplemented with FBS for 24 h. The RR-PpIX-PSilQ NPs at a concentration of 0.5 mg/mL were kept at 37 °C in the Zetasizer Nano plastic cuvette for 24 h. The particle size and size distribution of RR-PpIX-PSilQ or RR-PpIX-PSilQ(cur) NPs were recorded by DLS at regular intervals of time for a total period of 24h. All the results were the mean of three test runs, and all data is presented as the average ± SD.

### *4.2.6. Determination of the amount of PpIX-loaded to PsilQ NPs by UV-visible spectroscopy.*

The absorption spectra of RR-PpIX-PSilQ materials were recorded by UV-vis spectrophotometer (Varian, Cary 300 Bio). In order to calculate the percentage of loading of PpIX in PSilQ NPs, absorbance of the RR-PpIX-PSilQ NPs was measured at 408 nm in aqueous medium. Then by plotting the calibration curve for PpIX using absorbance as the function of different PpIX concentration (made by diluting DMSO stock solution in aqueous medium), the amount of PpIX loaded per milligram of PSilQ NPs was calculated. Three batches were tested, and the data is presented as the average ± SD.

### *4.2.7. Determination of the amount of PpIX-loaded to PsilQ NPs by thermogravimetric analysis.*

The amount of PpIX loaded to RR-PpIX-PSilQ materials was further confirmed by thermogravimetric analysis (TGA). TGA was conducted using a Mettler Toledo TGA/SDTA851 instrument. A platinum pan was used to hold the sample, which was

heated at a rate of 1.0 °C/min from 25.0 to 800.0 °C and held to the highest temperature for 3 h under nitrogen atmosphere. The data is reported as the mean ± SD.

### *4.2.8. Quantification of curcumin loaded to RR-PpIX-PsilQ NPs by ultra-high performance liquid chromatography.*

The chromatographic analysis was performed using UHPLC with a Thermo scientific UHPLC plus focused series LC /UV Vanquish diode array detector system, fitted with 1.9 μm particle size, 100 x 2.1 mm Hypersil Gold C18 column (Thermo Scientific, USA). Samples (10 μL) were injected with a flow rate of 250 μL/min in 10% Solvent B (Solvent A: water/ 0.1% Formic Acid [vol/vol]; Solvent B: acetonitrile/ 0.1% Formic Acid [vol/vol]). Analytes were eluted from the column after a 1 min holding at 10 % B with a linear 9 μL /min gradient to 100% B. After a 3 min holding at 100% B, the column was returned to 10% B in 4 min and re-equilibrated for 5 min before the next injection. Curcumin standards ranged from 100 to 800 pg/10 μL injection. The detection wavelength used for curcumin was 421 nm. Diluted aliquots from the supernatant obtained for the synthesis of RR-PpIX-PSilQ(cur) NPs were used for this analysis. Three batches were tested, and the data is presented as the average ± SD. The amount of curcumin loaded to RR-PpIX-PSilQ NPs was also confirmed by TGA as described above.

### *4.2.9. Quantification of Chemically available primary amines using the Kaiser's test.*

The Kaiser's test was used to quantify primary amines on the surface of PEG- and PEI-RR-PpIX-PSilQ NPs as described elsewhere [7]. Sodium acetate buffer (2 M, 100 mL) was prepared by dissolving 14.11 g sodium acetate in 86 mL distilled water

followed by addition of 14 mL glacial acetic acid (2 M). The pH of the resulting solution was adjusted to 5.4 using an acid. The ninhydrin solution was prepared by dissolving 0.5 g ninhydrin in 10 mL ethanol. For the Kaiser's assay; 100 μL of the prepared sodium acetate buffer (pH 5.4) and 70 μL ninhydrin solution were mixed together in a glass vial. Then 10-20 μL of the NP sample was added. The tubes were heated up to 70 °C in an oil bath for 10-15 min. After cooling, 3 mL of ethanol-water mixture in a ratio of 3:2 (vol/vol) was added to each tube. Finally, the absorbance of each solution was measured at 570 nm against the reference blank by a UV-Vis spectrophotometer. The results were the average of four test runs, and all data is presented as the average ± SD.

***4.2.10. Release of PpIX from RR-PpIX-PSilQ NPs via reductive degradation.***

RR-PpIX-PSilQ NPs are stimulus-responsive degradable nanoplatform that are capable of recognizing and responding to cell-specific microenvironmental changes. To study the release of PpIX molecules from RR-PpIX-PSilQ NPs under simulated reducing environment, the reducing agent dithiothreitol (DTT) was used. Three separate dispersions of RR-PpIX-PSilQ NPs at a concentration of 2 mg/mL in DMF were used. Before starting the time dependent measurements, the RR-PpIX-PSilQ NPs were washed with DMF to remove any physisorbed PpIX. Then the dispersion of nanoparticles was stirred at 37 °C and after regular time intervals of 30 min the nanoparticles were centrifuged down, and the absorbance of the supernatant was measured at 408 nm. The supernatant was return to the original vial and the nanoparticle were re-dispersed. This process was repeated 4 times to determine the background release of PpIX. At this point,

DTT was added to two of the nanoparticle dispersions to reach a final concentration of 10 μM and 10 mM, respectively. The rationale for choosing this concentration range is the huge difference of glutathione (GSH) concentration between extracellular (2-10 μM) and intracellular (2-10 mM) condition.[119–121] Additionally, since the concentration of GSH has been found to be several fold higher in cancer cells than in normal cells, we wanted to test our system for selectivity towards cancer cells. The absorbance was measured at defined intervals (0 – 28 h) following the protocol described above. These values were used to calculate and plot the percentage of PpIX release versus time. The dispersion not treated with DTT was used as control experiment. The results were the average of three test runs, and all data is presented as the average ± SD.

***4.2.11. Ex vitro Singlet oxygen ($^1O_2$) detection.***

To measure the amount of singlet oxygen ($^1O_2$) generated by RR-PpIX-PSilQ materials, 9,10-anthracene dipropionic acid (ADPA) was used as a $^1O_2$ trapping reagent.[75,78] In a typical experiment, 2 mL of an aqueous solution containing 0.05 mM ADPA and 100 μg/mL RR-PpIX-PSilQ NPs was placed in a quartz cuvette under dark conditions. The solution was then illuminated under red light (λ = 620-630 nm, fluence rate = 24.5 mW/cm$^2$) for different irradiation times [0, 5, 10, 15, and 20 min]. The non-irradiated samples were kept in dark as the control for the experiment. The absorption of the control and irradiated samples were recorded at 378 nm. The $^1O_2$ generation was evaluated by the decreasing in absorbance intensity of ADPA at 378 nm before and after

irradiation. The results were the average of three test runs, and all data is presented as the average ± SD.

### *4.2.12. Photostability of RR-PpIX-PSilQ NPs.*

To examine the photostability of the RR-PpIX-PSilQ materials, photo bleaching experiments were carried out. Samples were irradiated using a red light ($\lambda$ = 620-630 nm, fluence rate = 24.5 mW/cm$^2$) for 20 min. The fluorescence spectra were recorded before and after the irradiation. For comparison, PpIX was also investigated for its photostability, under the same conditions as control group.

### *4.2.13. Cell culture.*

MDA-MB-231, a human invasive TNBC cell line; and MCF-10A, a normal epithelial cell lines were purchased from American Type Culture Collection (ATCC). Breast cancer cells were cultured in RPMI 1640 medium (supplemented with 10% FBS, 1% pen-step) at 37 °C with 5% $CO_2$ atmosphere. For culturing MCF-10A cell line, MEGM (Mammary Epithelial Cell Medium) 1 kit BulletKit (basal media and SingleQuots packaged together) obtained from Lonza fischer Scientific. The culture media was changed every other day. All cell cultures were maintained in 25 cm$^2$ or 75 cm$^2$ cell culture flasks and the cells were passaged at 70-80% confluency every 2-4 days. The cell survival was tested by the CellTiter 96® AQueous Assay (MTS assay). The absorbance was measured at a wavelength of 490 nm in a plate reader Multiskan FC.

### *4.2.14. Measurement of intracellular ROS in PDT.*

2',7'-dichlorodihydrofluorescein diacetate (DCFH-DA) is a commonly used cell permeable fluorescent probe for measuring intracellular ROS.[122] MDA-MB-231 cells were seed in a 24-well plate at a density of 2 x $10^4$ cells and incubated at 37 °C in 5% $CO_2$ atmosphere for 24 h. The cells were incubated with RR-PpIX-PSilQ NPs and RR-PpIX-PSilQ(cur), each at three different concentrations of PpIX [12.5, 25, 37.5 μM], in order to study the concentration dependence. One hour before irradiation, the nanoparticles were removed, and the cells were washed twice with PBS. MDA-MB-231 cells were incubated with DCFH-DA (10 μM) in low serum media in dark at 37 °C and 5% $CO_2$. Subsequently, the media was removed, and cells were washed with PBS. MDA-MB-231 cells were exposed to red light (620-630 nm, 24.5 mW/$cm^2$) for 20 min. Immediately after irradiation, the cells were washed with PBS and harvested using trypsin [0.25% Trypsin with EDTA]. The formation of DCF was quantified by monitoring fluorescence at 485/528 nm using a flow cytometer (BD LSRFortessa™ cell analyzer). Results were analyzed using FlowJo software. MDA-MB-231 cells incubated with nanoparticles, but not irradiated, and cells not treated with nanoparticles were used as control groups. The results were the average of three test runs, and all data is presented as the average ± SD.

To study the formation of intracellular $^1O_2$ generated during the PDT experiment, $^1O_2$ production by RR-PpIX-PSilQ NPs and RR-PpIX-PSilQ(cur) NPs internalized by MDA-MB-231 cells was measured by an indirect method of detection based on the

measurement of the SOSG fluorescence in the cell lysate.[123] MDA-MB-231 cells were seeded in a 96-well plate at a density of 2 x $10^4$ cells and incubated at 37 °C in 5% $CO_2$ atmosphere for 24 h. The pre-seeded MDA-MB-231 cells in a 96-well plate were treated with different PpIX concentrations [12.5, 25, 37.5 μM] of RR-PpIX-PSilQ NPs and RR-PpIX-PSilQ(cur) NPs and incubated for 48 h at 37 °C in 5% $CO_2$ atmosphere. After that, the cell media was removed, and the cells were washed twice with PBS to remove any non-internalized nanoparticles. Then, MDA-MB-231 cells were lysed by adding 20 μL of 1% triton X 100 (TX 100) to each well and incubated for 30 min. SOSG solution [made as per manufacturer's protocol] was added to each well for a final concentration of 5 μM. The lysate-containing 96-well plates were illuminated with light (λ = 620-630 nm, fluence rate = 24.5 mW/$cm^2$) for 20 min. The absorbance and emission values for the lysates were measured at excitation/emission of 505/520 nm using a microplate reader. The results were the average of three test runs, and all data is presented as the average ± SD.

***4.2.15. Qualitative analysis by confocal laser scanning microscopy (CLSM).***

MDA-MB-231 cells were seeded on the top of a cover glass in 6-well plates at a density of 1 x $10^5$ cells and incubated for 24 h at 37 °C in 5% $CO_2$ atmosphere. The cells were treated with RR-PpIX-PSilQ(cur) NPs in fresh media at a concentration of 30 μg/mL, and were incubated for another 48 h. $H_2$DCF-DA (10 μM) was added to the cells in low serum media [with 1% serum] in dark and incubated for 30 min. Subsequently, the cells were washed with PBS and were exposed to the red light irradiation (620-630 nm,

24.5 mW/cm$^2$) for 20 min. After irradiation, the cells were washed with PBS, incubated with fresh media and stained with Hoechst 33342 for 15 min. Images were acquired using a Olympus Fluoview FV 1000 confocal fluorescence microscope. Cells not irradiated and not treated with the nanoparticles were used as control groups.

To visualize intracellular $^1O_2$ generation, we explored a newer alternative approach for detecting the intracellular formation of $^1O_2$ *in vitro*. For this, SOSG was first loaded to the fabricated RR-PpIX-PSilQ materials. By using this new assay, the RR-PpIX-PSilQ(cur) NPs are utilized not only as $^1O_2$ generators but are also being used as the carrier for SOSG molecules. To prepare RR-PpIX-PSilQ(cur) NPs loaded with SOSG, 1 mg of RR-PpIX-PSilQ(cur) NPs were dispersed in 1 mM aqueous solution of SOSG. The dispersion was allowed to stir for 24 h under dark conditions. After stirring for 24h in dark, the nanoparticles were washed to remove any free SOSG before further use. The prepared RR-PpIX-PSilQ(cur) NPs-doped-SOSG were redispersed in PBS (1 mg/mL). For ***in vitro*** imaging, the pre-seeded cells were treated with RR-PpIX-PSilQ(cur) NPs and RR-PpIX-PSilQ(cur) NPs-doped-SOSG, in the same manner as explained above. Briefly, MDA-MB-231 cells were seeded on the top of a cover glass in 6-well plates at a density of 1 x $10^5$ cells and incubated for 24 h at 37 °C in 5% $CO_2$ atmosphere. The cells were treated with RR-PpIX-PSilQ(cur) NPs and RR-PpIX-PSilQ(cur) NPs-doped-SOSG in fresh media at a concentration of 5 μg/mL, and were incubated for another 48 h. Next, the cells treated with RR-PpIX-PSilQ(cur) NPs were further incubated for 1 h with SOSG solution at a final concentration 5 μM in well plate. In order to have a fair comparison, treatment concentration of SOSG was fixed at 5 μM for all the treatment sets.

Subsequently, the cells were washed with PBS and were exposed to the red-light irradiation (620-630 nm, 24.5 mW/cm$^2$) for 20 min. After irradiation, the cells were washed with PBS, incubated with fresh media and stained with Hoechst 33342 for 15 min. Images were acquired using an Olympus Fluoview FV 1000 confocal fluorescence microscope. Cells not irradiated and not treated with the nanoparticles were used as control groups.

***4.2.16. In vitro PDT cell toxicity.***

The *in vitro* cytotoxicity of PpIX, RR-PpIX-PSilQ NPs, RR-PpIX-PSilQ(cur) NPs were evaluated by MTS assay. In addition, PEI-RR-PpIX-PSilQ(cur) NPs, and PEG-PEI-RR-PpIX-PSilQ(cur) NPs were also tested for their photocytotoxicities by MTS assay before evaluating their siRNA delivery efficiency. For this study, MDA-MB-231 cells were seeded in 96-well plate at a density of 5 x $10^3$ cells per well in 100 μL of complete media and incubated at 37 °C in 5% $CO_2$ atmosphere for 24 h. After removing the cell culture medium, PpIX (in DMSO), RR-PpIX-PSilQ NPs, RR-PpIX-PSilQ(cur) NPs, PEI-RR-PpIX-PSilQ(cur) NPs, and PEG-PEI-RR-PpIX-PSilQ(cur) NPs were dispersed in complete media and added to the MDA-MB-231 cells at different PpIX concentrations (9 - 222 μM). After 48 h of incubation in the presence of RR-PpIX-PSilQ materials, the culture media was removed, and the cells were washed twice with PBS. MDA-MB-231 cells were illuminated with the red light (620-630 nm) at a fluence rate of 24.5 mW/cm$^2$ for 20 min. Control experiments were maintained in the same conditions, but in the dark for the same interval of time. After irradiation, the media was replaced by fresh media

and the cells were allowed to grow for an additional 24 h. To measure the phototoxic and dark toxicity effects the treated MDA-MB-231 cells were subjected to cell viability assay using the MTS assay following the instructions provided by the vendor. Cell viability (%) was calculated as follows: viability = $(A_{sample}/A_{control}) \times 100\%$, where $A_{sample}$ and $A_{control}$ denote as absorbance values of the sample and control wells measured at 490 nm, respectively. Data were graphed from at least three independent experiments performed with six replicates. The data is reported as the average ± SD.

***4.2.17. Intracellular trafficking of RR-PpIX-PSilQ nanoparticles.***

To monitor the intracellular trafficking of RR-PpIX-PSilQ NPs, MDA-MB-231 cells were seeded on the top of a cover glass in 6-well plate at a density of 5 x $10^6$ cells/well and incubated for 24 h at 37 °C in 5% $CO_2$ atmosphere. The cells were incubated in the presence of RR-PpIX-PSilQ NPs at a concentration of 5 μg/mL for 24 h. Cells were washed twice with PBS and further incubated with Lyso-Tracker Green DND-99 at 300 nM (Molecular Probes, Invitrogen, USA) for 20 min or 200 nM ER tracker™ Blue-White DPX (Molecular Probes) for 45 min following the procedure described by the vendor. Imaging flow cytometer (Amnis ImageStream® Platform) was used for analyzing the intracellular localization of the nanoparticles in MDA-MB-231 cells. The data was analyzed using IDEAS™ analysis software.

### *4.2.18. Preparation of PEG-PEI-RR-PpIX-PSilQ(cur) NPs- Alexa488-labeled dsDNA/GFP-siRNA nanoplexes.*

To fabricate the PEG-PEI-RR-PpIX-PSilQ(cur) nanoplexes with Alexa488 dsDNA or GFP-siRNA, a N/P (moles of amines to moles of phosphates) ratio of 10 was used.[124] For Alexa488-labeled dsDNA loading to nanoparticles, 1 mg of PEG-PEI-RR-PSilQ(cur) NPs were suspended in 2 mL assembly buffer (2mM $Ca^{2+}$, $Mg^{2+}$). To this, Alexa488-labeled dsDNA [35 μL of 10 μM stock solution for N/P = 10] was added dropwise at room temperature. The nanoplexes were produced by incubating the dispersion for 30-45 min at $4^0$C. The formed PEG-PEI-RR-PpIX-PSilQ(cur) NPs Alexa488-labeled DNA nanoplexes were centrifuged, washed and redispersed in buffer to a final concentration of 1 mg/mL. The same protocol was used for GFP-siRNA loading. Briefly, 1mg of PEG-PEI-RR-PpIX-PSilQ(cur) was dispersed in 2 mL of assembly buffer. To this, 35 μL of GFP-siRNA [for N/P = 10] was added dropwise, and this was incubated for 30-45 min at 4 $^o$C, resulting in formation of PEG-PEI-RR-PpIX-PSilQ(cur) nanoplexes. The formed nanoplexes was centrifuged, washed and redispersed in assembly buffer to a final concentration of 1 mg/mL, and consequently used for in vitro studies. PEI-RR-PpIX-PSilQ(cur) NPs was also used to form similar nanoplexes using same procedure as above, for comparison purposes.

### *4.2.19. Assessment of cellular uptake of Alexa488-labeled dsDNA-loaded PEG-PEI-RR-PpIX-PSilQ nanoparticles.*

CLSM and flow cytometry were used to evaluate the uptake of the Alexa488-labeled dsDNA-loaded PEG-PEI-RR-PpIX-PSilQ NPs in MDA-MB-231 cells. For flow

cytometry, MDA-MB-231 cells were cultured in 24-well plate at a density of 2 x $10^4$ cells/well in 0.5 mL medium and incubated for 24 h at 37 °C and 5% $CO_2$ atmosphere. PEG-PEI-RR-PpIX-PSilQ(cur) and PEI-RR-PpIX-PSilQ(cur) NPs loaded with Alexa488-labeled dsDNA were added to the cultured cells at a dose of 30 μg/mL and incubated for 48 h. Afterwards, the cells were washed, trypsinized and collected for analysis in the flow cytometer (BD LSRFortessa™ cell analyzer) using mean FL-1, and FL-2 for Alexa488 and PpIX fluorescence, respectively. Alexa488-labeled dsDNA was also evaluated as control sample. GraphPad Prism version 7.03 for Mac, (GraphPad Software, La Jolla California USA, www.graphpad.com) was used for the statistical analysis of the results. Data were graphed from at least three independent experiments performed with two replicates.

For CLSM, the MDA-MB-231 cells were seeded on a coverslip placed in 6-well plates at a density of 5 × $10^4$ cells per well in 2 mL of DMEM and incubated at 37 °C in 5% $CO_2$ atmosphere for 24 h. After removing the culture medium, the cells were incubated with PEG-PEI-RR-PpIX-PSilQ(cur) and PEI-RR-PpIX-PSilQ(cur) NPs loaded with Alexa488-labeled dsDNA at a dose of 30 μg/mL in complete media. After 48 h of incubation, cells were washed three times with cold PBS. The cell nuclei were stained with Hoechst 33342 for 15 min. All microscopy images were acquired with an Olympus Fluoview FV 1000 CLSM.

### *4.2.20. Silencing of green fluorescence protein using GFP-siRNA loaded PEG-PEI-RR-PpIX-PSilQ(cur) NPs in GFP expressing MDA-MB-231 cells.*

To obtain MDA-MB-231_GFP cells, regular MDA-MB-231 cells were transfected with a GFP plasmid and then sorted in the FL-1 channel to select stable GFP expressing cells. The sorted cells were then cultured and used for siRNA transfection studies. MDA-MB-231_GFP cells were seeded in 24-well plate at a density of 1 x $10^4$ cells per well in 0.5 mL complete medium and incubated for 24 h at 37 °C in 5% $CO_2$ atmosphere. The cells were then exposed to three different concentrations [22, 44, 66 μM of PpIX] of the formed GFP-siRNA loaded PEG- and PEI-RR-PpIX-PSilQ(cur) materials and incubated for 48 h. The nanoplatform was found to be non-toxic within the selected concentrations, both under light and dark conditions. The cells were washed twice with PBS and culture for additional 24 h in fresh medium. The plates were analyzed and imaged for microscopic imaging. For flow cytometry cells were harvested and the decrease in GFP expression (FL-1 channel) was analyzed. The data is reported in terms of percentage of GFP silencing. The data is reported as the average ± SD.

To assess the effect of PCI, a phenomenon associated with PDT systems on the transfection efficacy of RR-PpIX-PSilQ NPs, the combination of PCI and silencing was evaluated in MDA-MB-231_GFP cells. The cells were seeded in 24-well plate at a density of 1 x $10^4$ cells per well in 0.5 mL complete medium and incubated for 24 h at 37 °C in 5% $CO_2$ atmosphere. The MDA-MB-231_GFP cells were treated with GFP-siRNA loaded PEG- and PEI-RR-PpIX-PSilQ(cur) materials [22, 44, 66 μM of PpIX] and incubated for 48 h. After incubation time, the cells were washed and irradiated with red

light (620-630 nm) at a rate of 24.5 mW/cm$^2$ for 5 min. Fresh media was added and the plates were incubated for an additional 24 h. Next, the plates were analyzed and imaged for microscopic imaging. For flow cytometry, MDA-MB-231_GFP were harvested and the decrease in GFP expression (FL-1 channel) was analyzed. The data is reported in terms of percentage of GFP silencing. Statistical analyses were performed by using GraphPad Prism (v7.03 for Windows, La Jolla California, CA, USA). The effect of PDT in GFP silencing was evaluated by two-way univariate analysis of variance (ANOVA) model with the Bonferroni post hoc test. A value of $p < 0.05$ was considered as statistically significant.

**4.3. Results and discussion.**

***4.3.1. Synthesis of the redox-responsive of PpIX silica derivative (5).***

The synthesis of the redox-responsive PpIX silane ligand was performed through a series of sequential reactions as shown in Scheme 1. First, the carboxylic acid groups in the PpIX molecule were activated using N-hydroxy succinimide (NHS) through a coupling reaction mediated by 1-ethyl-3-(3'-dimethylaminopropyl)carbodiimide (EDC) to afford PpIX-SE (2). Compound 2 was reacted with cysteine hydrochloride in the presence of diisopropylethylamine (DIPEA) affording PpIX-Cys (3). The thiol group in compound 3 was modified by a disulfide exchange reaction using dipyridine disulfide (DPDS) to afford 4. DPDS acted as an activating group for the next reaction between compound 4 and 3-mercaptopropyltriethoxysilane (MPTES) through another disulfide exchange reaction to produce the final redox-responsive PpIX silane ligand (5).

### *4.3.2. Synthesis of RR-PpIX-PSilQ, RR-PpIX-PSilQ(cur), PEI-RR-PpIX-PSilQ(cur), and PEG-PEI-RR-PpIX-PSilQ(cur) Nanoparticles.*

The synthesis of RR-PpIX-PSilQ nanoparticles was carried out by the microemulsion method. Microemulsion-based synthesis is a versatile route to fabricate nanoparticle-based delivery platforms. This approach relies on the preferential distribution of a hydrophobic ligand into the oil droplet of the oil-in-water (O/W) microemulsion. The benefit of using the micro-emulsions as nanoreactors has proven to be an effective method to reduce the polydispersity in the nanoparticle size. In addition, the hydrophobic nature of the nanodroplet can be used to solubilize and encapsulate a wide spectrum of hydrophobic drugs. In this work, we used AOT as surfactant, n-butanol as cosurfactant, cyclohexane as the oil phase and water as the main component of the microemulsion system. Aqueous ammonia and NaOH solution were added to enhance the solubility and accelerate the condensation of the PpIX silane precursor 5. By using this synthetic approach, RR-PpIX-PSilQ NPs with narrow size distribution and high loading of PpIX molecules were obtained. Moreover, the microemulsion method allows for the co-encapsulation of other hydrophobic drugs. In this work, we selected curcumin as a model drug. Curcumin is a well-known naturally occurring plant-derived compound that is extracted from the famous Indian spice turmeric.[125,126] It has been shown to possess various biological and pharmacological properties.[127,128] In several studies the anticancer effect of curcumin against different types of cancer such as breast, ovarian, pancreatic, and neuroblastoma has been observed.[129–132] Curcumin was added directly to the oil-in-water microemulsion solution to afford RR-PpIX-PSilQ(cur) NPs.

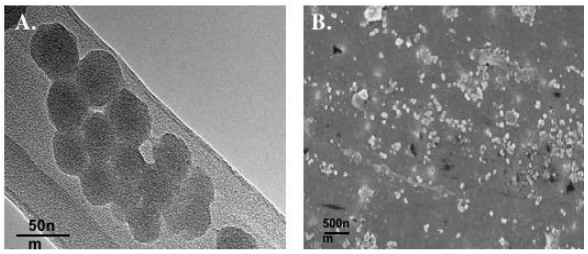


| | Size (nm) | ζ Potential (mV) |
|---|---|---|
| RR-PpIX PSilQ NPs | 254.8 ± 25.0 | -35.1 ± 3.0 |
| RR-PpIX-PSilQ(cur) NPs | 228.7 ± 40.0 | -38.6 ± 2.0 |
| PEI-RR-PpIX-PSilQ(cur) NPs | 313.8 ± 18.0 | +10.4 ± 0.6 |
| PEG-PEI-RR-PSilQ(cur) NPs | 271.3 ± 20.0 | +6.91 ± 0.3 |

*Figure 26. A. TEM and (B.) SEM images for RR-PpIX-PSilQ NPs along with characterization table.*

We took advantage of the negative charge produce by the presence of the carboxylate groups on the surface the RR-PpIX-PSilQ NPs under physiological pH to further functionalize the nanoparticles through electrostatic interaction with the positively charged polyethylene imine (PEI; MW=10kD) polymer (PEI-RR-PpIX-PSilQ(cur) NPs). This strategy renders the capability to the PEI-RR-PpIX-PSilQ(cur) platform as gene carrier by using the electrostatic binding of the cationic polymer PEI with the negatively charged DNA or RNA.[133] Finally, the PEI-RR-PpIX-PSilQ(cur) NPs were modified with polyethylene glycol (PEG; MW=2kD). PEG molecules enhance the biocompatibility of nanoparticles and for *in vivo* applications can reduce their opsonization and uptake by mononuclear phagocytic system (MPS).[134,135]

### *4.3.3. Characterization of RR-PpIX-PSilQ, RR-PpIX-PSilQ(cur), PEI-RR-PpIX-PSilQ(cur), and PEG-PEI-RR-PpIX-PSilQ(cur) Nanoparticles.*

The physicochemical properties of the different RR-PpIX-PSilQ materials were characterized using transmission and scanning electron microscopy (TEM/SEM), dynamic light scattering (DLS), ζ-potential, UV-vis and fluorescence spectroscopy, thermogravimetric analysis (TGA), Kaiser's assay, ultra-high performance liquid

chromatography (UHPLC), and $^1O_2$ generation using ADPA probe. TEM and SEM were utilized to analyze the particle size and morphology of the fabricated RR-PpIX-PSilQ nanoparticles. The nanoparticles are spherical in shape with an average diameter of 40 ± 5 nm (N= 40 particles), as depicted in **Figure 26**. The hydrodynamic diameter and ζ-potential of the different RR-PpIX-PSilQ materials was characterized by DLS and the electrophoretic mobility in phosphate buffer solution [PBS, 1 mM]. The RR-PpIX-PSilQ NPs showed a hydrodynamic diameter of 254.8 ± 25.0 nm, which higher than the one measured by TEM/SEM. Aggregation of the nanoparticles of PBS and swelling may account for this observation.[113] A negative value of -35.1 ± 3.0 mV for the ζ-potential was measured that is indicative of the presence of carboxylate groups on the surface of the RR-PpIX-PSilQ NPs (**Table 1**). The co-encapsulation of curcumin into RR-PpIX-

*Table 4. Characterizaiton of the amine functional groups on the surface of the MSN*

| Sample | PEI with NPs (nmol) | Free amines on NPs (nmol/mg) |
|---|---|---|
| PEI-RR-PpIX-PSilQ(cur) NPs | 1.00 | 536.0 |
| PEG-PEI-RR-PpIX-PSilQ(cur) NPs | 0.62 | 328.0 |

PSilQ NPs had a negligible effect on the hydrodynamic diameter and ζ-potential of the nanoparticles, 228.7 ± 40.0 nm and -38.6 ± 2.0 mV, respectively. Nevertheless, after surface modification of the RR-PpIX-PSilQ(cur) NPs with PEI polymer, both the hydrodynamic diameter increased from 228.7 ± 40.0 to 313.8 ± 18.0 nm and the ζ-potential from -38.6 ± 2.0 to +10.4 ± 0.6 mV. The increase in aggregation is due to the reduction in electrostatic repulsion; but, it is also indicative of the coating of RR-PpIX-PSilQ(cur) NPs with PEI polymer. Another possible explanation for the increase of the hydrodynamic diameter in the PEI-RR-PpIX-PSilQ(cur) NPs could be that the surface of

the nanoparticles is not uniformly covered with the cationic PEI polymer causing the formation of aggregated particles on standing. Further functionalization of the PEI-RR-PpIX-PSilQ(cur) NPs with PEG polymer reduced the hydrodynamic diameter without much variation in the ζ-potential, 271.3 ± 20.0 nm and +6.9 ± 0.3 mV, respectively. The steric effect due to the PEG chains increased the repulsion between nanoparticles in dispersion, which produced a decrease in the hydrodynamic diameter.[136]

To study the colloidal stability of the RR-PpIX-PSilQ platform, PEG-PEI- and RR-PpIX-PSilQ NPs were redispersed in cell media containing FBS and the hydrodynamic diameter was measured over a period of 24 h at 37 °C. It was seen that both the nanoplatforms were satisfactorily stable over the measurement time of 24 h, under the physiological media supplemented with FBS.

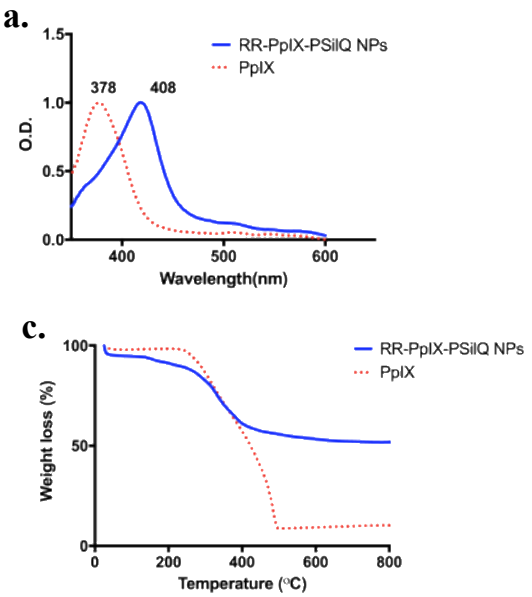


**d.**

| Percentage of PpIX content in nanoparticles | | |
|---|---|---|
| | **UV-Vis** | **TGA** |
| RR-PpIX-PSilQ NPs | 25.8 ± 10.0 | 24.4 ± 2.5 |

*Figure 27. (a)UV-Visible spectra for RR-PSilQ NPs, absorption band at 401nm, with shoulders at 520nm, 550 nm, and 580 nm. (b) Thermogravimetric analysis for for RR-PSilQ NPs, RR-PSilQ-Cur NPs, Curcumin, and PpIX. Left-Bar graph showing organic content for nanoparticles. (c) Hydrodynamic diameter (DLS), and PpIX content obtained from UV-Visible spectra and TGA.*

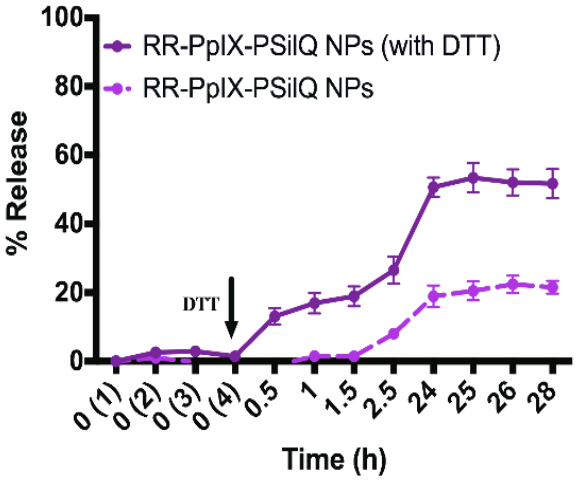


*Figure 28. Release profile showing the release of PpIX from RR-PSilQ NPs in the presence (solid line) and absence (broken line) of the reducing agent DTT. Data points show the average and SD of three independent experiments.*

The UV-vis absorption spectra of free PpIX and PpIX-RR-PSilQ NPs showed the characteristic Soret and Q bands for porphyrin molecules. A red shift for the Soret band of the PpIX-RR-PSilQ NPs was observed compared with free PpIX, from 378 nm to 408 nm. This red shift effect can be explained by the close packing of the PpIX molecules into the framework of the PSilQ platform, which results in a bathochromic shift typical of J-aggregates for porphyrins as has been reported for other nanoparticles.[137,138] The fluorescence spectra of free PpIX and PpIX-RR-PSilQ NPs revealed a 7-fold decrease in the fluorescence intensity for the nanoparticle formulation in comparison with free PpIX. This decrease in the fluorescence is accounted by the self-quenching effect due to the close proximity of the PpIX molecules in this type of nanoparticulate systems. We have reported this observation in other PSilQ NPs containing porphyrins.

Thermogravimetric analysis and UV-vis spectroscopy were used to determine the amount of PpIX loaded to the RR-PpIX-PSilQ NPs**.** TGA showed a loss in total organic content in three batches in the range of 46-52%, which correspond to 24.4 ± 2.5 % of PpIX **(**450 ± 50 μmol/g). This PpIX loading was further corroborated by UV-Vis spectroscopy by measuring the absorbance at 408 nm of RR-PpIX-PSilQ NPs in DMF. The actual amount of PpIX was determined using a calibration curve of PpIX.

To quantify the amount of primary amines chemically available on the surface of the RR-PpIX-PSilQ nanoparticles after functionalization with PEI polymer, the ninhydrin-based Kaiser's test was performed.[139] After the analysis for three batches of PEG-PEI-RR-PpIX-PSilQ(cur) NPs and PEI-RR-PpIX-PSilQ(cur) NPs, the amount of chemically accessible primary amines was 328 ± 10 and 536 ± 45 nmol per mg of nanoparticles, respectively (**Table 2**). In addition, the ratio of 0.61 implies that more than 50% of the primary amines reacted with the methoxy PEG-NHS.

The amount of curcumin loaded into RR-PpIX-PSilQ(cur) nanoparticles was determined by UHPLC. The supernatant solution of the microemulsion reaction to fabricate the RR-PpIX-PSilQ(cur) NPs was stored and analyzed by UHPLC. The analysis showed negligible amount of curcumin present in the supernatant, ~1.0 % wt of the total amount of curcumin added, as an indication that most of the curcumin (~99.0 %wt) was loaded to RR-PpIX-PSilQ(cur) NPs [201.5 nmol/mg]. Furthermore, TGA showed an increase of 8.5 ± 1.5 on the percentage of organic content for RR-PpIX-PSilQ(cur) NPs compared to RR-PpIX-PSilQ NPs. This data corroborates the loading obtained by UHPLC which shows loading of approximately 7.56 %wt.

### *4.3.4. Triggered release via reductive degradation.*

Precise control over nanoparticle degradation is desirable to eliminate unwanted side effects to healthy cells, premature release and uncontrolled disintegration of the nanoplatform, which taken together adversely affect the therapeutic outcome. Recently, efforts are being made for the development of stimuli responsive delivery systems. We have shown in previous reports that by using a disulfide bond as part of the building unit for the fabrication of porphyrin-based PSilQ NPs, redox-responsive properties can be rendered to the platform.[81,84,140] Some advantages have been demonstrated by using the approach of on/off biodegradability properties.[69,141]

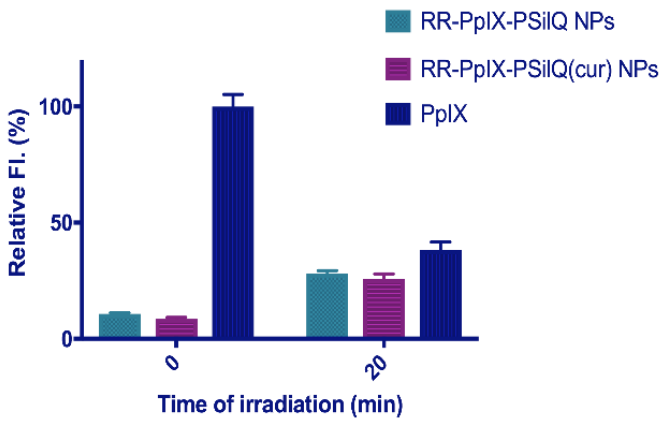


*Figure 29. Relative photostability for RR-PSilQ NPs, RR-PSilQ-Cur NPs, and PpIX, before and after 20 min irradiation using red light (630nm) at fluence rate of 24 mW/cm2.*

In this work, the controlled release of PpIX under high reducing environment was investigated using 10 mM dithiothreitol (DTT) as reducing agent. As depicted in **Figure 28**, there is minimal leakage of PpIX from the RR-PpIX-PSilQ NPs before the addition of DTT. This leakage was considered to be caused by mechanical degradation and not actual

release of PpIX. However, a greater and more rapid release of ~10% PpIX was observed immediately after the addition of 10 mM DTT. This is attributed to the cleavage of the disulfide bond on the surface of the RR-PpIX-PSilQ NPs. A steady release was observed during the following 24 h where a plateau was finally reached. The amount released of PpIX from RR-PpIX-PSilQ NPs in that period of time in the presence DTT was ~50% of the total amount loaded to the nanoparticles. In the case of both, 10 mM DTT (data not shown) and the control sample (without DTT), ~20% release of PpIX molecules was seen over the time period for the study (**Figure 28**). The release in the control sample is attributed to the hydrolysis of the silica bond, which also can cause the release of PpIX molecules. Overall, the results demonstrate that the presence of DTT at a concentration of 10 mM or higher triggers the reduction the disulfide (–S-S-) bonds within the RR-PpIX-PSilQ NPs framework resulting in the release of the active photosensitizer.

***4.3.5. Photobleaching/Photostability studies.***

Photobleaching is one of the primary limitations for the long term use of photosensitizers.[15,30,141,142] It occurs due to the degradation and the loss of fluorescence intensity of the PS molecule under light conditions. To evaluate the photostability of RR-PpIX-PSilQ NPs, the nanoparticles were exposed to red light (620-630 nm) at irradiance of 24.5 mW/cm$^2$ for 20 min (**Figure 29**). Free PpIX at the same concentration was used as the control. There is no major change in fluorescence intensity for the RR-PpIX-PSilQ NPs after irradiation with red light. However, there is a dramatic decrease of more than 50% on the fluorescence coming from free PpIX molecules as an indication of

photobleaching. Previous reports have shown that nanoparticle systems have the ability to prevent photobleaching by preventing the reaction between oxygen and other oxidative products that are responsible for photodegradation.[143–146]

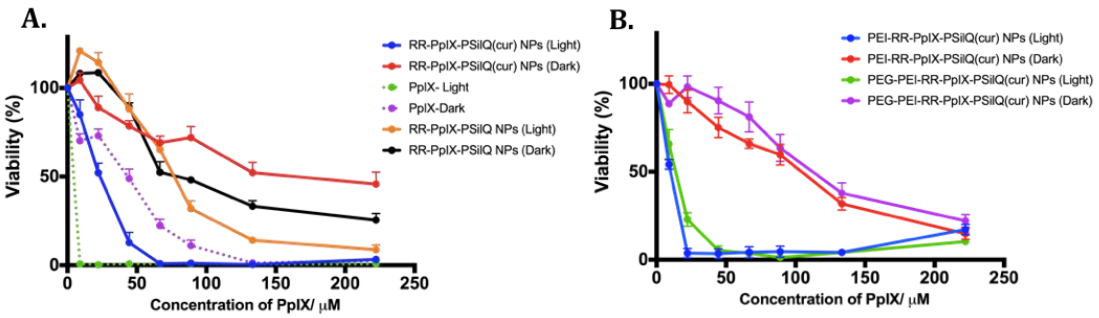


*Figure 30. Cyto-phototoxicity for MDA-MB-231 cells incubated with RR-PSilQ (to be added..), RR-PSilQ-Cur, PEI-RR-PSilQ-Cur, and PEG-PEI-RR-PSilQ-Cur, at concentrations of PpIX ranging from 8-130μM. Incubation time was 48h, followed by irradiation at 24mWcm-2 for 20min.*

The basic principle for PDT is that after irradiation with light at the right wavelength, the PS molecule will generate $^1O_2$ through the energy transfer from the triplet excited state of the PS to molecular oxygen. To verify the ability of RR-PpIX-PSilQ NPs to produce $^1O_2$, a singlet oxygen probe 9,10-anthracene dipropionic acid (ADPA) was used. ADPA reacts with $^1O_2$ to form an endoperoxide, which prevents the absorption of light. The absorbance of ADPA at 378 nm was monitored in the presence of RR-PpIX-PSilQ NPs (with and without curcumin) after light exposure (620-630 nm; irradiance = 24.5 mW/cm$^2$) at different times [0, 5, 10, 15, and 20 min. The absorption intensity of ADPA at 378 nm decreased gradually as a function of time of irradiation which is an indication that $^1O_2$ molecules are produced by both RR-PpIX-PSilQ and RR-PpIX-PSilQ(cur) NPs. Control experiments in the absence of light did not show significant change in the absorption intensity of ADPA at 378 nm. The RR-PpIX-PSilQ

platform shows the ability to generate $^1O_2$ in aqueous solution, but also important to note is that after degradation and release of free PpIX inside the cancer cells that $^1O_2$ production is restored.[69,85]

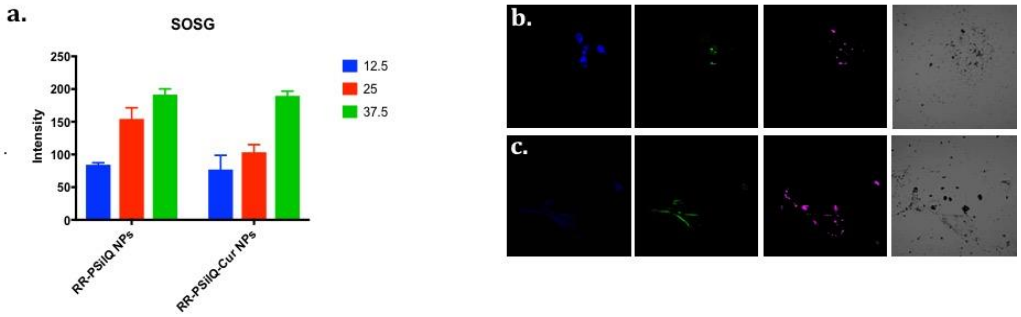


*Figure 31. Singlet oxygen detection using SOSG for RR-PSilQ NPs and RR-PSilQ-Cur NPs, for three concentrations of NPs (12.5,25.0,37.5 μg/mL). Confocal fluorescent microscopic images for MDA-MB-231 treated with (b.) RR-PpIX-PSilQ(cur) NPs-loaded with SOSG, (c.) RR-PpIX-PSilQ(cur) NPs, followed by SOSG treatment before irradiation. Blue channel for Hoechst 33362 stained nuclei. Green channel for fluorescence of SOSG in presence of singlet oxygen. Magenta channel for PpIX-PSilQ.*

### *4.3.6. PDT and combination therapy using the RR-PpIX-PSilQ platform in vitro.*

PDT is a localized therapeutic approach for potential eradication of malignant tissues and vasculature in carcinogenesis. It relies on preferential accumulation of a PS by tumor cells followed by their activation using specific wavelength of laser light. PDT has been used to treat different types of cancers such as skin cancer, lung, esophageal, and head, and neck in clinical settings. Recently, the first clinical trial to treat breast cancer with PDT is ongoing in UK.[147] In this work, we tested the ability of the RR-PpIX-PSilQ platform to treat TNBC. The phototoxicity of RR-PpIX-PSilQ materials in MDA-MB-231 TNBC cells was evaluated using the MTS assay (Figure 30). RR-PpIX-PSilQ NPs

showed a dose-dependent phototoxicity against MDA-MB-231 cells upon light irradiation of 24.5 mW/cm$^2$ for 20 min (5 J/cm$^2$). However, there was not a significant difference between the light and the dark condition for RR-PpIX-PSilQ NPs with IC50 values being 76.7 µM and 91.6 µM. Next, the phototoxicity of the RR-PpIX-PSilQ(cur) NPs was evaluated. The cell viability data showed significant phototoxicity when MDA-MB 231 cells were incubated with RR-PpIX-PSilQ(cur) NPs with the IC50 value dropping down by 71% (from 76.7 µM to 21.7 µM) for light irradiated system. This can be due to the release of curcumin molecules on light irradiation from the PSilQ NPs, as a result of which curcumin known for its ability to trigger apoptosis, in combination with PDT effect improves the efficacy of the system. This finding that the combination of curcumin with PpIX in RR-PpIX-PSilQ(cur) NPs appreciably enhanced the *in vitro* cytophototoxicity indicated that this combination may have synergistic or additive effect. In dark conditions, PpIX encapsulated into the PSilQ NPs is less cytotoxic than free PpIX ($IC_{50}$ = 46.4 µM vs 91.6 µM). It is remarkable that in the case of the RR-PpIX-PSilQ(cur) NPs the cytotoxicity is reduced in 4-fold of the free PpIX. It is most likely due to the antioxidant properties of curcumin.[94]

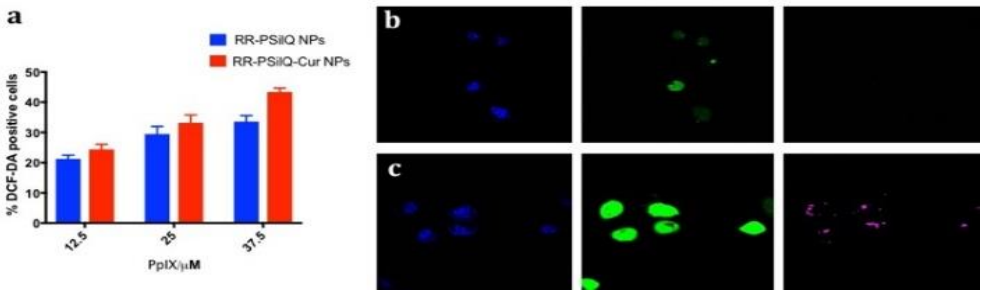


*Figure 32. In vitro detection of ROS using DCF-DA. (A)Quantitative measure of ROS using flow cytometry, with three concentrations of PpIX (12.5, 25.0, 37.5 µg/mL). (B, C) Confocal images for the visual aid of ROS generation in MDA-MB-231(B- non-irradiated, C- irradiated)*

The phototoxicity of the PEG- and PEI-RR-PpIX-PSilQ(cur) NPs was also investigated (**Table 5**). PEI coating increased the cytotoxicity of the nanoparticles ($IC_{50}$ = 94.1 μM), but further functionalization with PEG polymer reduced the toxic effect in the absence of light ($IC_{50}$ = 115.3 μM). The phototoxicity analysis showed that both materials have higher performance than RR-PpIX-PSilQ(cur) NPs, 9.3 and 12.2 μM, respectively. This increased efficiency of the nanoparticles can be attributed to the cationic surface which renders higher cellular interaction and thus increased internalization of the nanoparticles. Endosomal escape assists in the high efficacy of the surface modified platform.

Also, in order to assess the photocytotoxicity of the nanoparticles against healthy cells, normal human epithelial cell line MCF-10A was incubated with RR-PpIX-PSilQ NPs and treated under the same condition as the ones used for MDA-MB-231 cells. It is remarkable that both the phototoxicity and dark toxicity of free PpIX is at least 100-fold higher than those observed for RR-PpIX-PSilQ NPs. This is most likely to the differences of internalization between the free PpIX, which is through a diffusion/passive mechanism, and RR-PpIX-PSilQ NPs where the cells used an active mechanism (endocytosis).

*Table 5. IC 50 values under Light (irradiated) and Dark(non-irradiated) conditions.*

| Sample | IC 50(PpIX/μM) | |
|---|---|---|
| **MDA-MB-231** | **Light** | **Dark** |
| PpIX | 4.9 | 46.4 |
| RR-PpIX-PSilQ NPs | 76.7 | 91.6 |
| RR-PpIX-PSilQ(cur) NPs | 21.7 | 170.0 |
| PEI-RR-PpIX-PSilQ(cur) NPs | 9.3 | 94.1 |
| PEG-PEI-RR-PpIX-PSilQ(cur) NPs | 12.2 | 115.3 |
| **MCF-10A** | | |
| PpIX | 0.36 | 0.48 |
| RR-PpIX-PSilQ(cur) NPs | >67.0 | >67.0 |

### *4.3.7. Measurement of intracellular $^1O_2$ and ROS generated by RR-PpIX-PSilQ NPs.*

The generation of $^1O_2$ and ROS are key elements for the phototoxicity of PS molecules. One of the benefits of PDT is that without irradiation there is no $^1O_2$ produced and therefore no toxicity. To investigate the intracellular $^1O_2$ produced by RR-PpIX-PSilQ NPs, we used singlet oxygen sensor green (SOSG).[148] SOSG is a cell-impermeable compound, highly selective for $^1O_2$, which is used as an indirect method to quantify $^1O_2$. SOSG emits strong green fluorescence in the presence of $^1O_2$.[148] Samples of MDA-MB-231 cells incubated with different concentrations of RR-PpIX-PSilQ NPs and lysed were irradiated with red light (620-630 nm) at 24 mW/cm$^2$ for 20 min in the presence of SOSG (**Figure 31**). The production of $^1O_2$ is nanoparticle concentration dependent, which is associated to the amount of PpIX carried by the RR-PpIX-PSilQ NPs. RR-PpIX-PSilQ(cur) NPs were also tested for the generation of $^1O_2$ following this methodology. The fluorescence results showed that the curcumin co-encapsulated with the RR-PpIX-PSilQ NPs did not have a major effect in the formation of $^1O_2$. These results

demonstrated that RR-PpIX-PSilQ NPs after been internalized by MDA-MB-231 can still efficiently produce $^1O_2$, which is an important factor in accounting for the phototoxicity of these nanoparticles. Control experiments using SOSG were carried out with MDA-MB-231 cells incubated in the presence of RR-PpIX-PSilQ NPs but without irradiation, and in the absence of nanoparticles with light irradiation. In all the control experiments, minimal increase in fluorescence coming from SOSG was observed as an indication that the RR-PpIX-PSilQ NPs under light irradiation are the main responsible for the generation of $^1O_2$.

To further corroborate that indeed RR-PpIX-PSilQ NPs can generate $^1O_2$ inside MDA-MB-231 a direct measured was performed taking advantage of the properties of RR-PpIX-PSilQ NPs as carriers. SOSG was passively loaded to the RR-PpIX-PSilQ NPs. This strategy allowed that the cell membrane-impermeable SOSG molecule can be transported inside of the cells. **Figure 31** shows confocal images for cells incubated with SOSG-loaded RR-PpIX-PSilQ(cur) NPs after irradiation with red light. Green fluorescence from SOSG was observed as an indication that of SOSG was not only efficiently transport inside the cells but was also able to detect the generation of $^1O_2$. As the control experiment, we treated the cells with the nanoparticles, followed by incubation with SOSG, in a sequential manner. As expected, the fluorescence was detected from the periphery of the cells, with negligible sub-cellular fluorescence, validating the impermeable nature of the probe.

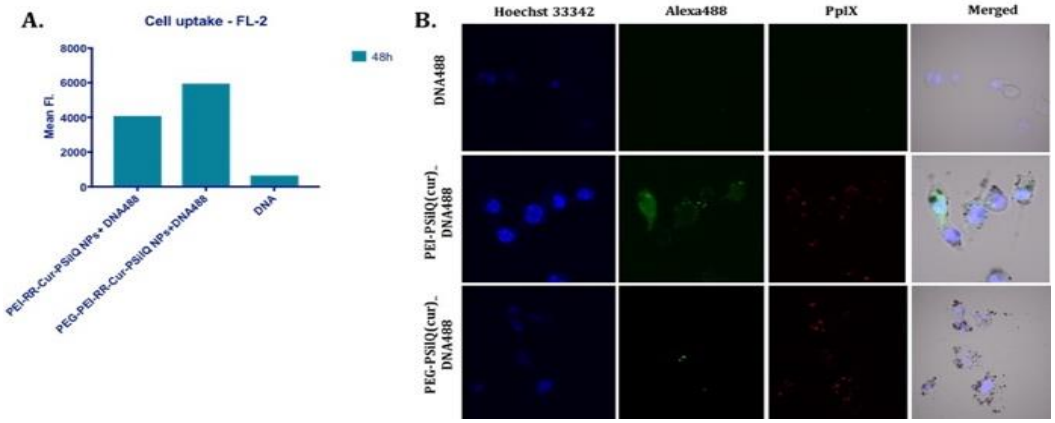


*Figure 33. Cell uptake for naked DNA-Alexa488, PEI-RR-PSilQ-Cur NPs, and PEG-PEI-RR-PSilQ-Cur NPs. (A) Mean fluorescence intensity obtained from flow cytometry was used to generate the graph, after correcting the data for untreated cells which served as control. (B) Confocal microscopy used to visually identify the uptake for naked DNA-Alexa488, PEI-RR-PSilQ-Cur NPs, and PEG-PEI-RR-PSilQ-Cur NPs, at a concentration of 30 ug/mL*

The production of ROS also plays a role for the effectiveness of PDT to treat cancer (**Figure 32**). The ability of RR-PpIX-PSilQ and RR-PpIX-PSilQ(cur) NPs to produce ROS in MDA-MB-231 cells was characterized using DCFH-DA.[122] The cells were incubated with different concentrations of nanoparticles and irradiated using red light (620-630 nm, 24.5 $mW/cm^2$) for 20 min. The positive cells showing the green fluorescence produced by the oxidation of DCFH-DA with ROS were quantified using flow cytometry. Both nanoparticles, RR-PpIX-PSilQ and RR-PpIX-PSilQ(cur), produced higher amount of ROS than control experiments. In addition, no statistical significant different were find between the amount of ROS generated by RR-PpIX-PSilQ or RR-PpIX-PSilQ(cur) NPs was found at lower concentrations (12.5 and 25 μg/mL). However, the ROS generations increased significantly for higher concentration (37.5 μg/mL), which can be justified by previous studies illustrating that curcumin triggers ROS production under red light. Confocal micrographs showed that MDA-MB-231 cells

incubated with RR-PpIX-PSilQ NPs in the absence of light irradiation generated some amount of green fluorescence, most likely due to the existence of endogenous ROS such as $H_2O_2$ in cells and certain oxidative stress generated by the nanoparticles.[122] However, the high intensity observed in the green fluorescence channel observed for MDA-MB-231 cells incubated with RR-PpIX-PSilQ NPs and irradiated with red light demonstrated the effective generation of ROS by the nanoparticles. The results from these experiments confirmed that RR-PpIX-PSilQ NPs can efficiently transport PpIX molecules inside the MDA-MB-231 cells with keeping the capability of generating both $^1O_2$ and ROS, which are critical elements for the effectivity of PDT.

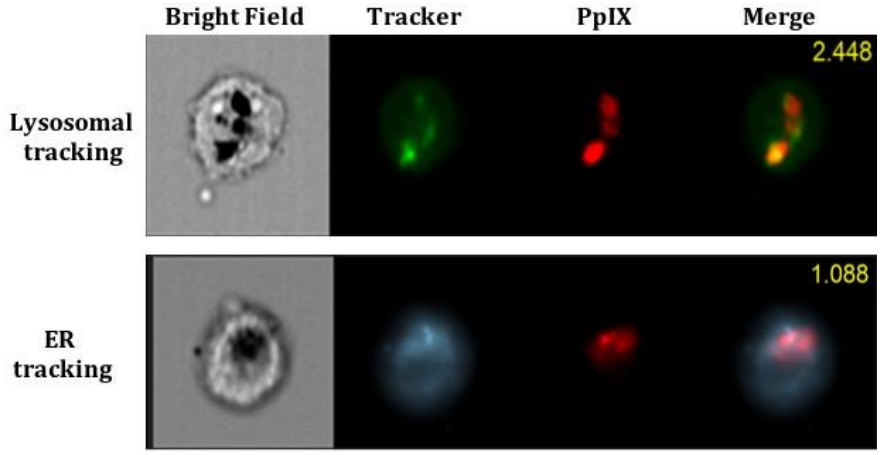


*Figure 34. In vitro fluorescence images of MDA-MB-231 cells labeled with lysotracker (green), and ER tracker (blue), after incubating with RR-PpIX-PSilQ(cur) NPs for 24 h.*

We performed additional investigation of the sub-cellular localization of RR-PpIX-PSilQ nanoparticles in MDA-MB-231 cells using imaging flow cytometer. Lyso-Tracker green and blue ER tracker were used for labelling lysosomes and endoplasmic reticulum (ER), respectively. Briefly, MDA-MB-231 cells were incubated with RR-

PpIX-PSilQ NPs for 24 h and the co-localization of fluorescent images in the green (lysosomes), blue (ER) and red (nanoparticles) channels were analyzed by the new technique of image flow cytometry (AMNIS, **Figure 34**). The micrographs/data revealed that RR-PpIX-PSilQ nanoparticles were mainly co-localized in the lysosomes and occasionally in the cytosol and ER. The co-localization of PpIX-PSilQ NPs in the lysosome means that not only will ROS be released from the NPs but also oxidative enzymes will be released from the lysosome causing further cell damage.

### *4.3.8. RR-PpIX-PSilQ(cur) as efficient carrier for the intracellular transport of DNA and RNA material.*

The multifunctional capabilities of the RR-PpIX-PSilQ platform to carry genetic material were tested *in vitro* using the PEG- and PEI- RR-PpIX-PSilQ(cur) NPs. First, to study the transport and internalization of genetic material, Alexa488-labeled dsDNA was loaded to both PEG- and PEI- RR-PpIX-PSilQ(cur) NPs. MDA-MB-231 cells were incubated with these materials (30 μg/mL) for 48 h. Flow cytometry showed that nanoparticles efficiently carried Alexa488-labeled dsDNA into MDA-MB-231 cells compared with just Alexa488-labeled dsDNA by itself (**Figure 33**). These findings were further confirmed by confocal microscopy. Both the green and red channel depicted the presence of Alexa488-labeled dsDNA and nanoparticles. The merged image confirmed that they are successfully internalized inside MDA-MB-231 cells and mainly co-localized with each other. Interestingly, some of the fluorescence from the green channel did not co-localized with the nanoparticles as a possible indication that Alexa488-labeled dsDNA has been released from the nanoparticles.

To further corroborate the delivery properties of RR-PpIX-PSilQ system, MDA-MB-231 cells expressing green fluorescence protein were used (MDA-MB-231_GFP). Different amounts of GFP-siRNA was loaded to PEG- and PEI-RR-PpIX-PSilQ(cur) NPs to evaluate the silencing of GFP. Control experiments using free GFP-siRNA and lipofectamine 2000 (L2K) were also carried out. MDA-MB-231_GFP cells treated with the GFP-siRNA loaded nanoparticles were analyzed by flow cytometry to determine the transfection capability of the PEG- and PEI-RR-PpIX-PSilQ(cur) NPs. The flow cytometry data showed that the silencing of GFP is concentration-dependent with the maximum transfection reached at 138 and 84 nM of GFP-siRNA for PEG- and PEI-RR-PpIX-PSilQ(cur) NPs (150 µg/mL), respectively. At these concentrations, GFP silencing of 40 and 54 % was achieved in MDA-MB-231-GFP cells. Control experiments with free GFP-siRNA and L2K as carrier reached 0 and 70 % of transfection. These results confirmed that GFP-siRNA indeed needs a carrier to be able to afford any transfection. L2K is the standard system for transfection *in vitro*; however, it does have several limitations for *in vivo* applications. The data demonstrated that PEG- and PEI-RR-PpIX-PSilQ(cur) NPs were able to efficiently transport and deliver GFP-siRNA inside MDA-MB-231-GFP cells.

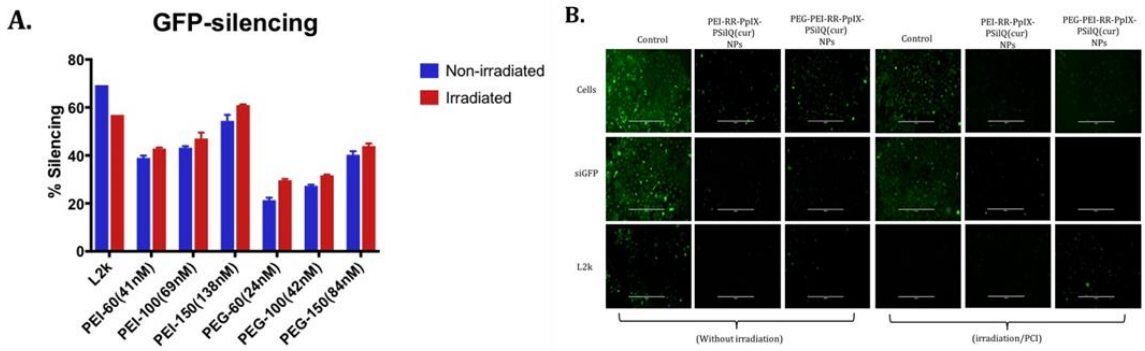


*Figure 35. GFP silencing after treatment with PEG- and PEI-RR-PpIX-PSilQ(cur) NPs showing the efficiency of gene delivery by PSilQ NPs.*

One of the main challenges for nanoparticle-based gene delivery systems is to escape from the endolysosomal pathway to efficiently deliver the DNA/siRNA material in the cytoplasm.[149] Several approaches have been explored to reach this goal. One alternative that has attracted attention in recent years is the use of photosensitizers. Photo-induced ROS generation could disrupt the endolysosomal membranes to facilitate nanoparticle escape and enhance gene transfection, this effect has been called photochemical internalization (PCI).[56,88] By taking advantage of the multimodal capabilities of our RR-PpIX-PSilQ platform, we explore the PCI effect on the delivery of GFP-siRNA. MDA-MB-231-GFP cells were treated with the GFP-siRNA loaded PEG- and PEI-RR-PpIX-PSilQ(cur) NPs as described above. After 48h of incubation, MDA-MB-231-GFP cells were irradiated with red light (620-630 nm) at an irradiance of 24.5 mW/cm$^2$ for 5 min. This light fluence is not enough to produce PDT effect but still allows the generation of $^1O_2$ and ROS by the PpIX loaded to the nanoparticles. As shown in **Figure 35**, a trend is observed in the enhancement of GFP silencing in MDA-MB-231-GFP cells after irradiation with light in comparison with the results discussed above,

which do not involve light irradiation. For the PEG- and PEI-RR-PpIX-PSilQ(cur) NPs with the highest concentration of GFP-siRNA tested in this work a transfection of 44 and 61 % was achieved, respectively. This correspond to an increase of GFP silencing of 4 and 7 %. MDA-MB-231-GFP cells transfected with L2K were also irradiated with red light using the conditions described above, but no enhancement on GFP silencing was observed. This result confirmed that the presence of photosensitizer molecule is required for the PCI effect. The transfection enhancement using the PEG- and PEI-RR-PpIX-PSilQ(cur) NPs is encouraging but needs to be further optimized.

# CHAPTER 5
# CONCLUSIONS AND FUTURE WORK

## 5.1. Conclusions and Future Work.

In conclusion, current limitations continue to hinder the abilities of PDT to be a widespread treatment method. Some of these limitations were addressed with the use of degradable NPs and combination therapy. mPEG PpIX PSilQ NPs showed to be an efficient PS delivery vehicle with an increase in phototoxicity and biocompatibility when compared to PpIX alone. PpIX PSilQ NPs were also shown to be useful in combination with chemotherapy and gene therapy. The use of an MSN as a combination delivery vehicle was also explored using Chlorin e6 and cisplatin. Both of these nanoparticles were shown to be biocompatible and showed a phototherapeutic efficacy when treating TNBC in an orthotopic model.

### *5.1.1. Biodegradable Protoporphyrin IX Loaded Silica-Based Nanoparticles For The Improved Photodynamic Therapy Of Triple-Negative Breast Cancer.*

#### *5.1.1.1. Conclusions.*

In this work, we were able to show the complete synthesis and application of PSilQ NPs using PDT to treat TNBC. The ligand was synthesized from the endogenous porphyrin, PpIX. The synthesis included the addition of a redox-responsive bond to allow the PSilQ NP to be biodegradable. The ligand structure was characterized as well as the photophysical properties. PpIX-PSilQ NPs were successfully synthesized using a reverse micro-emulsion technique before a hydrophilic polymer was conjugated to the surface to increase biocompatibility, producing the final product mPEG-PpIX-PSilQ NP. The

physico-chemical properties and photophysical properties were fully characterized before finally testing with *in vitro* and *in vivo* studies.

PpIX PSilQ NPs were proven to be redox responsive in the presence of reducing conditions. It was shown to undergo cellular uptake in TNBC cell line MDA-MB-231, as well as show phototoxicity towards multiple BC cell lines. Phototherapeutic efficacy studies showed mPEG-PpIX-PSilQ NPs were capable of slowing tumor growth in a TNBC orthotopic model using MDA-MB-231. It once again was proven to be a redox responsive system as mPEG-PpIX-PSilQ NPs were degraded and excreted showing no residual PpIX in major organs after the study. This work has proven mPEG-PpIX-PSilQ NPs to be a quality NP for the treatment of TNBC using PDT.

*5.1.1.2. Future Work.*

Further purification of the ligand during synthesis may allow for better solubility as well as an increase in phototoxicity. The increase in solubility would allow for more characterization techniques to be used and provide insight to the full structure of the redox-responsive ligand. A complete study of the biocompatibility and biodistribution can also be investigated. This would provide a better understanding to the optimal irradiation time, and the amount of time it takes for mPEG-PpIX-PSilQ NPs to degrade inside the body.

Furthermore, the PSilQ platform can be used with other PSs. Chlorin E6 would be an alternative PS that could be used. Ce6 has shown to be an efficient PS and can be combined with multiple therapeutics to improve the overall efficacy of PSilQ NPs as a PDT treatment.

### *5.1.2. Combinatorial Mesoporous Silica Nanoparticles For The Delivery Of A Photosensitizer (Chlorin E6) And Chemotherapeutic (Cisplatin) In The Treatment Of Triple Negative Breast Cancer.*

#### *5.1.2.1. Conclusions.*

A combination treatment MSN was successfully synthesized to treat TNBC. Chlorin E6 was co-condensated during the MSN synthesis. A cis-platin prodrug (cisPt) was attached, along with a hydrophilic polymer, affording the mPEG-Ce6-cisPt-MSN. This MSN was subsequently used to treat TNBC in both *in vitro* and *in vivo* models. mPEG-Ce6-cisPT-MSN showed a high phototoxicity towards TNBC cell lines *in vitro* and drastically slowed tumor growth in an orthotopic model of TNBC cell line MDA-MB-231. These studies have given insight into the possibilities of combination therapy using MSNs. Also eluding to the abilities of combining PDT with other forms of therapy.

#### *5.1.2.2. Future Work.*

Further studies regarding the mechanism of cell death during combination therapy is needed. This would prove exactly what methods of cell death each therapeutic is involved with, whether it be necrosis, apoptosis, autophagy or a combination. A system comparing cisPt alone would also provide an understanding as to how much combination or synergy is occurring with the two therapeutics there.

Additionally, the combination of Ce6 with other chemotherapeutics is of great interest. Ce6 is a potent PS and therefore requires low concentrations to be effective. Combining this PS with a potent chemotherapeutic would potentially provide an efficient and effective treatment option.

### *5.1.3. Multifunctional Polysilsesquioxane Nanoparticles For Photo-, Chemo-, And Gene Therapy Of Triple-Negative Breast Cancer.*

#### *5.1.3.1. Conclusions.*

In summary, we have developed a more effective nanoparticle-based PS system for improving the strategy for photodynamic therapy. The PpIX-based PSilQ hybrid nanoparticles were engineered to incorporate redox responsive linkage, in addition to multi-functional carboxyl group, with oil-in-water direct microemulsion. The structural properties of these PpIX-based PSilQ NPs showed that by employing O/W microemulsion as the template, RR-PpIX-PSilQ NPs were synthesized with sizes of 40-50 nm in diameter and high contents of PpIX, of the order of 450-520 µmol per g of PSilQ NPs. Moreover, we show that RR-PpIX-PSilQ NPs form reasonably stable colloidal dispersion in complete biological medium (cDMEM) with the hydrodynamic radius not much altered from those measured in PBS, demonstrating their good solubility without any tendency for uncontrolled aggregation. The PpIX molecule exists in its quenched state as a part of nanoparticle in solution but can be released in cancerous intracellular conditions. The micellar formulation provided a method to co-load hydrophobic drug molecules within the core of the oil droplet. To our surprise, the curcumin loaded RR-PpIX-PSilQ NPs showed increased phototoxicity against MDA-MB-231 cell lines, suggesting some sort of synergism associated with combining curcumin with PDT. However, the mechanism behind this synergistic effect is still to be studied, in details. In addition, the surface of these formulated nanoparticles was functionalized with PEI and PEG modifications. PEI corona not only positively mitigated

the overall cellular toxicity of the corresponding nanoparticles, but it also enabled the generation of efficient nanoscale carrier for siRNA delivery.

Furthermore, with PEG modification, the *in vitro* gene silencing was tested using MDA-MB-231 TNBC cells overexpressing green fluorescent protein (GFP) where GFP was the target gene for knockdown. The optimal PEI-coated formulations resulted in silencing degree of as high as 70% compared to untreated cells. These results contribute to the establishment of a nanoplatform that can serve multiple functions and be useful in future for its multi-modality towards cancer therapeutics and other diseases.

References


1. Society, A. C. Cancer Facts & Figures 2018. (2018).
2. Siegel, R. L., Miller, K. D. & Jemal, A. Cancer statistics, 2018. *CA. Cancer J. Clin.* **68,** 7–30 (2018).
3. Chavez, K., Garimella, S. & Lipkowitz, S. Triple Negative Breast Cancer Cell Lines: One Tool in the Search for Better Treatment of Triple Negative Breast Cancer. *Breast Dis.* **32,** 35–48 (2012).
4. Hudis, C. A. & Gianni, L. Triple-Negative Breast Cancer: An Unmet Medical Need. *Oncologist* **16,** 1–11 (2011).
5. Foulkes, W. D., Smith, I. E. & Reis-Filho, J. S. Triple-Negative Breast Cancer. *N. Engl. J. Med.* **363,** 1938–1948 (2010).
6. Oualla, K. *et al.* Novel therapeutic strategies in the treatment of triple-negative breast cancer. *Ther. Adv. Med. Oncol.* **9,** 493–511 (2017).
7. Khosravi-Shahi, P., Cabezón-Gutiérrez, L. & Custodio-Cabello, S. Metastatic triple negative breast cancer: Optimizing treatment options, new and emerging targeted therapies. *Asia. Pac. J. Clin. Oncol.* **14,** 32–39 (2018).
8. Kassam, F. *et al.* Survival outcomes for patients with metastatic triple-negative breast cancer: Implications for clinical practice and trial design. *Clin. Breast Cancer* **9,** 29–33 (2009).
9. Sambi, M. *et al.* Alternative therapies for metastatic breast cancer: multimodal approach targeting tumor cell heterogeneity. *Breast cancer* **9,** 85–93 (2017).
10. Kalimutho, M. *et al.* Targeted Therapies for Triple-Negative Breast Cancer: Combating a Stubborn Disease. *Trends Pharmacol. Sci.* **36,** 822–846 (2015).
11. Dawood, S. Triple-Negative Breast Cancer. *Drugs* **70,** 2247–2258 (2010).
12. Holliday, D. L. & Speirs, V. Choosing the right cell line for breast cancer research. *Breast Cancer Res.* **13,** 1–7 (2011).
13. de Ruijter, T. C., Veeck, J., de Hoon, J. P. J., van Engeland, M. & Tjan-Heijnen, V. C. Characteristics of triple-negative breast cancer. *J. Cancer Res. Clin. Oncol.* **137,** 183–192 (2011).
14. van Straten, D., Mashayekhi, V., de Bruijn, H. S., Oliveira, S. & Robinson, D. J. Oncologic photodynamic therapy: Basic principles, current clinical status and future directions. *Cancers (Basel).* **9,** 1–54 (2017).
15. O'Connor, A. E., Gallagher, W. M. & Byrne, A. T. Porphyrin and nonporphyrin photosensitizers in oncology: Preclinical and clinical advances in photodynamic therapy. *Photochem. Photobiol.* **85,** 1053–1074 (2009).
16. Allison, R. R. *et al.* Photosensitizers in clinical PDT. *Photodiagnosis Photodyn. Ther.* **1,** 27–42 (2004).
17. Ethirajan, M., Chen, Y., Joshi, P. & Pandey, R. K. The role of porphyrin chemistry in tumor imaging and photodynamic therapy. *Chem. Soc. Rev.* **40,** 340–62 (2011).
18. Dougherty, T. J. *et al.* Photodynamic Therapy. *JNCI J. Natl. Cancer Inst.* **90,** 889–905 (1998).
19. Zheng, Y. *et al.* Photodynamic-therapy activates immune response by disrupting immunity homeostasis of tumor cells, which generates vaccine for cancer therapy.

*Int. J. Biol. Sci.* **12,** 120–132 (2016).
20. Plackal Adimuriyil George, B. & Abrahamse, H. A Review on Novel Breast Cancer Therapies: Photodynamic Therapy and Plant Derived Agent Induced Cell Death Mechanisms. *Anticancer. Agents Med. Chem.* **16,** 793–801 (2016).
21. Lamberti, M. J. Breast cancer as photodynamic therapy target: Enhanced therapeutic efficiency by overview of tumor complexity. *World J. Clin. Oncol.* **5,** 901 (2014).
22. Akopov, A. *et al.* Preoperative endobronchial photodynamic therapy improves resectability in initially irresectable (inoperable) locally advanced non small cell lung cancer. *Photodiagnosis Photodyn. Ther.* **11,** 259–264 (2014).
23. Mimikos, C., Shafirstein, G. & Arshad, H. Current state and future of photodynamic therapy for the treatment of head and neck squamous cell carcinoma. *World J. Otorhinolaryngol. Neck Surg.* **2,** 126–129 (2016).
24. Caesar, L. *et al.* The use of photodynamic therapy as adjuvant therapy to surgery in recurrent malignant tumors of the paranasal sinuses. *Photodiagnosis Photodyn. Ther.* **12,** 414–421 (2015).
25. Allison, R. R. *et al.* Photodynamic therapy for chest wall recurrence from breast cancer. *Photodiagnosis Photodyn. Ther.* **1,** 157–171 (2004).
26. Agostinis, P. *et al.* Photodynamic Therapy of Cancer : An Update. *Am. Cancer Soc.* **61,** 250–281 (2011).
27. Wilson, B. C. & Patterson, M. S. The physics, biophysics and technology of photodynamic therapy. *Phys. Med. Biol.* **53,** R61–R109 (2008).
28. Wilson, B. C. & Patterson, M. S. The physics of photodynamic therapy. *Phys. Med. Biol.* **31,** 327–360 (1986).
29. Master, A., Livingston, M. & Gupta, A. Sen. Photodynamic Nanomedicine in the Treatment of Solid Tumors : Perspective and Challenges. *J Control Release* **168,** 88–102 (2013).
30. Allison, R. R. & Sibata, C. H. Oncologic photodynamic therapy photosensitizers: A clinical review. *Photodiagnosis Photodyn. Ther.* **7,** 61–75 (2010).
31. Scientific Committee on Emerging and Newly-Identified Health Risks. *Health Effects of Artificial Light*. *SCENIHR* (2012). doi:10.2772/8624
32. Wang, C., Cheng, L. & Liu, Z. Upconversion nanoparticles for photodynamic therapy and other cancer therapeutics. *Theranostics* **3,** 317–330 (2013).
33. Grossman, C. E. *et al.* Fluence rate differences in photodynamic therapy efficacy and activation of epidermal growth factor receptor after treatment of the tumor-involved murine thoracic cavity. *Int. J. Mol. Sci.* **17,** (2016).
34. Zhu, T. C., Kim, M. M., Liang, X., Finlay, J. C. & Busch, T. M. In-vivo singlet oxygen threshold doses for PDT. *Photonics Lasers Med.* **4,** 59–71 (2015).
35. Lee, S. *et al.* In vivo PDT dosimetry : singlet oxygen emission and photosensitizer fluorescence. *Phys. Sci. Inc.* (2010). doi:10.1117/12.846358
36. DeRosa, M. C. & Crutchley, R. J. Photosensitized singlet oxygen and its applications. *Coord. Chem. Rev.* **233–234,** 351–371 (2002).
37. Castano, A. P., Demidova, T. N. & Hamblin, M. R. Mechanisms in photodynamic therapy: Part one - Photosensitizers, photochemistry and cellular localization.

*Photodiagnosis Photodyn. Ther.* **1,** 279–293 (2004).
38. Lovell, J. F., Liu, T. W. B., Chen, J. & Zheng, G. Activatable photosensitizers for imaging and therapy. *Chem. Rev.* **110,** 2839–2857 (2010).
39. Kessel, D. Death pathways associated with photodynamic therapy. *Med. Laser Appl.* **21,** 219–224 (2006).
40. Gomer, C. J. PRECLINICAL EXAMINATION OF FIRST and SECOND GENERATION PHOTOSENSITIZERS USED IN PHOTODYNAMIC THERAPY. *Photochem. Photobiol.* **54,** 1093–1107 (1991).
41. Wang, X. *et al.* Analysis of the in vivo and in vitro effects of photodynamic therapy on breast cancer by using a sensitizer, Sinoporphyrin sodium. *Theranostics* **5,** 772–786 (2015).
42. Ormond, A. B. & Freeman, H. S. Dye sensitizers for photodynamic therapy. *Materials (Basel).* **6,** 817–840 (2013).
43. Yang, H. *et al.* Chemo-photodynamic combined gene therapy and dual-modal cancer imaging achieved by pH-responsive alginate/chitosan multilayer-modified magnetic mesoporous silica nanocomposites. *Biomater. Sci.* **5,** 1001–1013 (2017).
44. Latas, K. J. Heavy Atom Effects on the Phosphorescent Triplet States of Several Aromatic Molecules. **82,** 491–495 (1978).
45. Hayashi, K. *et al.* Photostable iodinated silica/porphyrin hybrid nanoparticles with heavy-atom effect for wide-field photodynamic/photothermal therapy using single light source. *Adv. Funct. Mater.* **24,** 503–513 (2014).
46. Issa, M. C. A. & Manela-Azulay, M. Photodynamic therapy: a review of the literature and image documentation. *An. Bras. Dermatol.* **85,** 501–511 (2010).
47. Jinadasa, R. G. W. Design , Synthesis , and Characterization of Porphyrin Derivatives for Biological Applications. (2013).
48. Wi, D., Hirth, A., Bogdahn-rai, T., Schnurpfeil, G. & Shopova, M. Photodynamic therapy of cancer : second and third generations of photosensitizers. *Russ. Chem. Bull.* **47,** 807–816 (1998).
49. Bechet, D. *et al.* Nanoparticles as vehicles for delivery of photodynamic therapy agents. *Trends Biotechnol.* **26,** 612–621 (2008).
50. Vega, D., Lodge, P. & Vivero-Escoto, J. Redox-Responsive Porphyrin-Based Polysilsesquioxane Nanoparticles for Photodynamic Therapy of Cancer Cells. *Int. J. Mol. Sci.* **17,** 56 (2015).
51. Mamaeva, V., Sahlgren, C. & Lindén, M. Mesoporous silica nanoparticles in medicine-Recent advances. *Adv. Drug Deliv. Rev.* **65,** 689–702 (2013).
52. Gary-Bobo, M. *et al.* Cancer therapy improvement with mesoporous silica nanoparticles combining targeting, drug delivery and PDT. *Int. J. Pharm.* **423,** 509–515 (2012).
53. Chatterjee, D. K., Fong, L. S. & Zhang, Y. Nanoparticles in photodynamic therapy: An emerging paradigm. *Adv. Drug Deliv. Rev.* **60,** 1627–1637 (2008).
54. Zhao, B. *et al.* Enhanced photodynamic efficacy towards melanoma cells by encapsulation of Pc4 in silica nanoparticles. *Toxicol. Appl. Pharmacol.* **241,** 163–172 (2009).
55. Dixit, V., Van Den Bossche, J., Sherman, D. M., Thompson, D. H. & Andres, R.

P. Synthesis and grafting of thioctic acid-PEG-folate conjugates onto Au nanoparticles for selective targeting of folate receptor-positive tumor cells. *Bioconjug. Chem.* **17,** 603–609 (2006).
56. Mackowiak, S. A. *et al.* Targeted drug delivery in cancer cells with red-light photoactivated mesoporous silica nanoparticles. *Nano Lett.* **13,** 2576–2583 (2013).
57. Iyer, A. K., Khaled, G., Fang, J. & Maeda, H. Exploiting the enhanced permeability and retention effect for tumor targeting. *Drug Discov. Today* **11,** 812–818 (2006).
58. Fang, J., Nakamura, H. & Maeda, H. The EPR effect: Unique features of tumor blood vessels for drug delivery, factors involved, and limitations and augmentation of the effect. *Adv. Drug Deliv. Rev.* **63,** 136–151 (2011).
59. Sudimack, J. & Lee, R. J. Targeted drug delivery via the folate receptor. *Adv. Drug Deliv. Rev. Deliv. Rev.* **41,** 147–62 (2000).
60. He, C., Hu, Y., Yin, L., Tang, C. & Yin, C. Effects of particle size and surface charge on cellular uptake and biodistribution of polymeric nanoparticles. *Biomaterials* **31,** 3657–3666 (2010).
61. Frohlich, E. The role of surface charge in cellular uptake and cytotoxicity of medical nanoparticles. *Int. J. Nanomedicine* **7,** 5577–5591 (2012).
62. Taylor-Pashow, K. M. L., Della Rocca, J., Huxford, R. C. & Lin, W. Hybrid nanomaterials for biomedical applications. *Chem. Commun.* **46,** 5832–5849 (2010).
63. He, C., Lu, J. & Lin, W. Hybrid nanoparticles for combination therapy of cancer. *J. Control. Release* **219,** 224–236 (2015).
64. An, B. K. *et al.* Organic nanoparticles for drug delivery and imaging. *MRS Bull.* **39,** 219–223 (2014).
65. Jin, C. S. & Zheng, G. Liposomal nanostructures for photosensitizer delivery. *Lasers Surg. Med.* **43,** 734–748 (2011).
66. Smolyanskaya, A. & Born, R. T. Liposomes derived from molecular vases. *Nature* **489,** 372–374 (2012).
67. Gaio, E., Scheglmann, D., Reddi, E. & Moret, F. Uptake and photo-toxicity of Foscan®, Foslip® and Fospeg® in multicellular tumor spheroids. *J. Photochem. Photobiol. B Biol.* **161,** 244–252 (2016).
68. Danhier, F. *et al.* PLGA-based nanoparticles : An overview of biomedical applications. *J. Control. Release* **161,** 505–522 (2012).
69. Oh, I. H. *et al.* Cancer cell-specific photoactivity of pheophorbide a-glycol chitosan nanoparticles for photodynamic therapy in tumor-bearing mice. *Biomaterials* **34,** 6454–6463 (2013).
70. Wilson, W. R. & Hay, M. P. Targeting hypoxia in cancer therapy. (2011). doi:10.1038/nrc3064
71. Shafer, F. & Buettner, G. Redox Environment of the Cell as Viewed Through the Redox State of the Glutathione Disulfide/Glutathion Couple. **30,** 1191–1212 (2001).
72. Auffan, M. *et al.* Towards a definition of inorganic nanoparticles from an environmental, health and safety perspective. *Nat. Nanotechnol.* **4,** 1–8 (2009).

73. Cheng, Y. *et al.* Highly efficient drug delivery with gold nanoparticle vectors for in vivo photodynamic therapy of cancer. *J. Am. Chem. Soc.* **130,** 10643–10647 (2008).
74. Lu, K., He, C. & Lin, W. Nanoscale metal-organic framework for highly effective photodynamic therapy of resistant head and neck cancer. *J. Am. Chem. Soc.* **136,** 16712–5 (2014).
75. Wieder, M. E. *et al.* Intracellular photodynamic therapy with photosensitizer-nanoparticle conjugates: cancer therapy using a 'Trojan horse'. *Photochem. Photobiol. Sci.* **5,** 727–34 (2006).
76. Shen, J. *et al.* Upconversion Nanoparticles for Photodynamic Therapy. *Small* **9,** 3213–3217 (2013).
77. Idris, N. M. *et al.* In vivo photodynamic therapy using upconversion nanoparticles as remote-controlled nanotransducers. *Nat. Med.* **18,** 1580–1585 (2012).
78. Ohulchanskyy, T. Y. *et al.* Organically modified silica nanoparticles with covalently incorporated photosensitizer for photodynamic therapy of cancer. *Nano Lett* **7,** 2835–2842 (2007).
79. Bourgeat-lami, E. in *Hybrid Organic/Inorganic Particles, in Hybrid Materials: Synthesis, Characterization, and Applications* 6 (2007).
80. Vivero-Escoto, J. L. & Huang, Y.-T. Inorganic-organic hybrid nanomaterials for therapeutic and diagnostic imaging applications. *Int. J. Mol. Sci.* **12,** 3888–927 (2011).
81. Vivero-escoto, J. L., Decillis, D., Fritts, L. & Vega, D. L. Porphyrin-based polysilsesquioxane nanoparticles to improve photodynamic therapy for cancer treatment. in *Optical Methods for Tumor Treatment and Detection: Mechanisms and Techniques in Photodynamic Therapy* **8931,** 1–10 (2014).
82. Rocca, J. Della *et al.* Polysilsesquioxane nanoparticles for triggered release of cisplatin and effective cancer chemoradiotherapy. *Nanomedicine Nanotechnology, Biol. Med.* **11,** 31–38 (2015).
83. Della Rocca, J., Huxford, R. C., Comstock-Duggan, E. & Lin, W. Polysilsesquioxane nanoparticles for targeted platin-based cancer chemotherapy by triggered release. *Angew. Chemie - Int. Ed.* **50,** 10330–10334 (2011).
84. Vivero-Escoto, J., Rieter, W., Lau, H. & Huxford-Phillips, R. Biodegradable Polysilsesquioxane Nanoparticles as Efficient Contrast Agents for Magnetic Resonance Imaging. *Small* **9,** 3523–3531 (2013).
85. Croissant, J. G. *et al.* Synthesis of disulfide-based biodegradable bridged silsesquioxane nanoparticles for two-photon imaging and therapy of cancer cells. *Chem. Commun.* **51,** 12324–12327 (2015).
86. Yang, G. *et al.* Mesoporous silica nanorods intrinsically doped with photosensitizers as a multifunctional drug carrier for combination therapy of cancer. *Nano Res.* (2014). doi:10.1007/s12274-014-0558-0
87. Slowing II, Vivero-Escoto, J. L., Wu, C. W. & Lin, V. S. Y. Mesoporous silica nanoparticles as controlled release drug delivery and gene transfection carriers. *Adv. Drug Deliv. Rev.* **60,** 1278–1288 (2008).
88. Argyo, C., Weiss, V., Bräuchle, C. & Bein, T. Multifunctional mesoporous silica

nanoparticles as a universal platform for drug delivery. *Chem. Mater.* **26,** 435–451 (2014).
89. Vivero-Escoto, J. L., Slowing II, Trewyn, B. G. & Lin, V. S. Mesoporous silica nanoparticles for intracellular controlled drug delivery. *Small* **6,** 1952–1967 (2010).
90. Vivero-Escoto, J. L. & Vega, D. L. Stimuli-responsive protoporphyrin IX silica-based nanoparticles for photodynamic therapy in vitro. *RSC Adv.* **4,** 14400 (2014).
91. Simon, V. *et al.* Pp IX silica nanoparticles demonstrate differential interactions with in vitro tumor cell lines and in vivo mouse models of human cancers. *Photochem. Photobiol.* **86,** 213–222 (2010).
92. Tu, H.-L. *et al.* In vitro studies of functionalized mesoporous silica nanoparticles for photodynamic therapy. *Adv. Mater.* **21,** 172–177 (2009).
93. Poon, C., He, C., Liu, D., Lu, K. & Lin, W. Self-assembled nanoscale coordination polymers carrying oxaliplatin and gemcitabine for synergistic combination therapy of pancreatic cancer. *J. Control. Release* **201,** 90–9 (2015).
94. Postiglione, I., Chiaviello, A. & Palumbo, G. Enhancing photodynamyc therapy efficacy by combination therapy: Dated, current and oncoming strategies. *Cancers (Basel).* **3,** 2597–2629 (2011).
95. De Freitas, L. M., Soares, C. P. & Fontana, C. R. Synergistic effect of photodynamic therapy and cisplatin: A novel approach for cervical cancer. *J. Photochem. Photobiol. B Biol.* **140,** 365–373 (2014).
96. Zhou, X. *et al.* Dual-responsive mesoporous silica nanoparticles mediated codelivery of doxorubicin and Bcl-2 SiRNA for targeted treatment of breast cancer. *J. Phys. Chem. C* **120,** 22375–22387 (2016).
97. Zhang, W. *et al.* Co-Delivery of Cisplatin Prodrug and Chlorin e6 by Mesoporous Silica Nanoparticles for Chemo-Photodynamic Combination Therapy to Combat Drug Resistance. *ACS Appl. Mater. Interfaces* **8,** 13332–13340 (2016).
98. Lecaros, R. L. G., Huang, L., Lee, T.-C. & Hsu, Y.-C. Nanoparticle Delivered VEGF-A siRNA Enhances Photodynamic Therapy for Head and Neck Cancer Treatment. *Mol. Ther.* **24,** 106–116 (2016).
99. Teng, I.-T. *et al.* Phospholipid-functionalized mesoporous silica nanocarriers for selective photodynamic therapy of cancer. *Biomaterials* **34,** 7462–70 (2013).
100. Vivero-Escoto, J. & Elnagheeb, M. Mesoporous Silica Nanoparticles Loaded with Cisplatin and Phthalocyanine for Combination Chemotherapy and Photodynamic Therapy in vitro. *Nanomaterials* **5,** 2302–2316 (2015).
101. Yao, X., Chen, X., He, C., Chen, L. & Chen, X. Dual pH-Responsive Mesoporous Silica Nanoparticles for Efficient Combination of Chemotherapy and Photodynamic Therapy. *J. Mater. Chem. B* **3,** 4707–4714 (2015).
102. Tannock, I. F. & Rotin, D. Acid pH in tumors and its potential for therapeutic exploitation. *Cancer Res.* **49,** 4373–4384 (1989).
103. Patil, Y. B., Toti, U. S., Khdair, A., Ma, L. & Panyam, J. Single-step surface functionalization of polymeric nanoparticles for targeted drug delivery. *Biomaterials* **30,** 859–866 (2009).
104. Moan, J. *et al.* PHARMACOLOGY OF PROTOPORPHYRIN IX IN NUDE

MICE AFTER APPLICATION OF ALA AND ALA ESTERS. *Int. J. Cancer* **103,** 132–135 (2003).
105. Fischer, M. J. E. in *Surface Plasmon Resonance* **627,** 55–73 (2010).
106. Uttamlal, M. & Holmes-smith, A. S. The excitation wavelength dependent fluorescence of porphyrins. *Chem. Phys. Lett.* **454,** 223–228 (2008).
107. Kano, K., Minamizono, H., Kitae, T. & Negi, S. Self-Aggregation of Cationic Porphyrins in Water. Can π−π Stacking Interaction Overcome Electrostatic Repulsive Force? *J. Phys. Chem. A* **101,** 6118–6124 (1997).
108. Kahne, D. & Still, W. C. Hydrolysis of a peptide bond in neutral water. *J. Am. Chem. Soc.* **110,** 7529–7534 (1988).
109. Secret, E. *et al.* Two-photon excitation of porphyrin-functionalized porous silicon nanoparticles for photodynamic therapy. *Adv. Mater.* **26,** 7643–7648 (2014).
110. Khairutdinov, R. F. & Serpone, N. Photoluminescence and Transient Spectroscopy of Free Base Porphyrin Aggregates. *J. Phys. Chem. B* **103,** 761–769 (1999).
111. He, C., Lu, K., Liu, D. & Lin, W. Nanoscale Metal − Organic Frameworks for the Co-Delivery of Cisplatin and Pooled siRNAs to Enhance Therapeutic E ffi cacy in Drug-Resistant Ovarian Cancer Cells. *J. Am. Chem. Soc.* **136,** 5181–5184 (2014).
112. Shi, X., Graiver, D. & Narayan, R. Hydrolysis and Condensation of Hydrophilic Alkoxysilanes Under Acidic Conditions. *Silicon* **4,** 109–119 (2012).
113. Haraguchi, K. Nanocomposite Hydrogels : A Unique Organic – Inorganic Network Structure with Extraordinary Mechanical , Optical , and Swelling / Deswelling Properties. **4095,** (2018).
114. Watermann, A. Mesoporous Silica Nanoparticles as Drug Delivery Vehicles in Cancer. *Nanomaterials* **7,** 189 (2017).
115. Shemesh, C. S., Hardy, C. W., Yu, D. S., Fernandez, B. & Zhang, H. Indocyanine green loaded liposome nanocarriers for photodynamic therapy using human triple negative breast cancer cells. *Photodiagnosis Photodyn. Ther.* **11,** 193–203 (2014).
116. Prat, A. *et al.* Phenotypic and molecular characterization of the claudin-low intrinsic subtype of breast cancer. *Breast Cancer Res.* **12,** 1–18 (2010).
117. Cairns, R. A., Harris, I. S. & Mak, T. W. Regulation of cancer cell metabolism. *Nat. Rev. Cancer* **11,** 85–95 (2011).
118. Fröhlich, E. The role of surface charge in cellular uptake and cytotoxicity of medical nanoparticles. *Int. J. Nanomedicine* **7,** 5577–5591 (2012).
119. Prasetyanto, E. A. *et al.* Hybrid Materials Hot Paper Breakable Hybrid Organosilica Nanocapsules for Protein Delivery Angewandte. 3323–3327 (2016). doi:10.1002/anie.201508288
120. Quignard, S., Masse, S., Laurent, G. & Coradin, T. Introduction of disulfide bridges within silica nanoparticles to control their intra-cellular degradation. *Chem. Commun.* **49,** 3410–3412 (2013).
121. Croissant, J. *et al.* Biodegradable Ethylene-Bis ( Propyl ) Disulfi de-Based Periodic Mesoporous Organosilica Nanorods and Nanospheres for Effi cient In-Vitro Drug Delivery. 6174–6180 (2014). doi:10.1002/adma.201401931
122. Aranda, A. *et al.* Dichloro-dihydro-fluorescein diacetate (DCFH-DA) assay: A quantitative method for oxidative stress assessment of nanoparticle-treated cells.

*Toxicol. Vitr.* **27,** 954–963 (2013).
123. Shen, Y. *et al.* Kinetic analysis of singlet oxygen generation in a living cell using Singlet Oxygen Sensor Green. *Opt. Heal. Care Biomed. Opt. IV* (2010). doi:10.1117/12.870261
124. Gary, D. J., Min, J. Bin, Kim, Y., Park, K. & Won, Y.-Y. The Effect of N/P Ratio on the In Vitro and In Vivo Interaction Properties of PEGylated Poly(2-(dimethylamino)ethyl methacrylate)-Based siRNA Complexes. *Macromol Biosci* **13,** 1059–1071 (2013).
125. Mirzaei, H. *et al.* Curcumin: A new candidate for melanoma therapy? *Int. J. Cancer* **139,** 1683–1695 (2016).
126. Mirzaei, H., Khoi, M. J. M., Azizi, M. & Goodarzi, M. Can curcumin and its analogs be a new treatment option in cancer therapy? *Cancer Gene Ther.* **23,** 410 (2016).
127. Ravindran, J., Prasad, S. & Aggarwal, B. B. Curcumin and Cancer Cells: How Many Ways Can Curry Kill Tumor Cells Selectively? *Aaps J.* **11,** 495–510 (2009).
128. Pescosolido, N., Giannotti, R., Plateroti, A. M., Pascarella, A. & Nebbioso, M. Curcumin: Therapeutical Potential in Ophthalmology. *Planta Med.* **80,** 249–254 (2014).
129. Karunagaran, D., Rashmi, R. & Kumar, T. R. S. Induction of apoptosis by curcumin and its implications for cancer therapy. *Curr. Cancer Drug Targets* **5,** 117–129 (2005).
130. Bandyopadhyay, D. Farmer to pharmacist: curcumin as an anti-invasive and antimetastatic agent for the treatment of cancer. *Front. Chem.* **2,** 11 (2014).
131. Nagaraju, G. P. *et al.* The impact of curcumin on breast cancer. *Integr. Biol.* **4,** 996–1007 (2012).
132. Mock, C. D., Jordan, B. C. & Selvam, C. Recent advances of curcumin and its analogues in breast cancer prevention and treatment. *Rsc Adv.* **5,** 75575–75588 (2015).
133. McBain, S. C., Yiu, H. H. P., El Haj, A. & Dobson, J. Polyethyleneimine functionalized iron oxide nanoparticles as agents for DNA delivery and transfection. *J. Mater. Chem.* **17,** 2561–2565 (2007).
134. Moghimi, S. M., Hunter, A. C. & Murray, J. C. Long-circulating and target-specific nanoparticles: Theory to practice. *Pharmacol. Rev.* **53,** 283–318 (2001).
135. Xie, J., Xu, C., Kohler, N., Hou, Y. & Sun, S. Controlled PEGylation of monodisperse Fe3O4 nanoparticles for reduced non-specific uptake by macrophage cells. *Adv. Mater.* **19,** 3163–+ (2007).
136. Darvishi, B., Farahmand, L. & Majidzadeh-a, K. Stimuli-Responsive Mesoporous Silica NPs as Non-viral Dual siRNA / Chemotherapy Carriers for Triple Negative Breast Cancer. **7,** 164–180 (2017).
137. Mauriello Jimenez, C. *et al.* Porous Porphyrin-Based Organosilica Nanoparticles for NIR Two-Photon Photodynamic Therapy and Gene Delivery in Zebrafish. *Adv. Funct. Mater.* **1800235,** 1–12 (2018).
138. Wang, D. *et al.* Synthesis of Self-Assembled Porphyrin Nanoparticle Photosensitizers. *ACS Nano* **12,** 3796–3803 (2018).

139. Xu, Z. *et al.* Colorimetric Determination of Polyamidoamine Dendrimers and their Derivates using a Simple and Rapid Ninhydrin Assay Colorimetric Determination of Polyamidoamine Dendrimers and their. **2719,** (2008).
140. Vivero-Escoto, J. L., Lyles, Z. & Vega, D. L. Multifunctional porphyrin-based polysilsesquioxane nanoparticles with improved loading capacity and phototherapeutic effect. *Photodiagnosis Photodyn. Ther.* **12,** 340 (2015).
141. Lucky, S. S., Soo, K. C. & Zhang, Y. Nanoparticles in photodynamic therapy. *Chem. Rev.* **115,** 1990–2042 (2015).
142. Wang, Z., Ma, R., Yan, L., Chen, X. & Zhu, G. Combined chemotherapy and photodynamic therapy using a nanohybrid based on layered double hydroxides to conquer cisplatin resistance †. *Chem. Commun.* **51,** 11587–11590 (2015).
143. Reisch, A. & Klymchenko, A. S. Europe PMC Funders Group Fluorescent Polymer Nanoparticles Based on Dyes : Seeking Brighter Tools for Bioimaging. **12,** 1968–1992 (2017).
144. Saxena, V. & Sadoqi, M. Enhanced photo-stability, thermal-stability and aqueous-stability of indocyanine green in polymeric nanoparticulate systems. *J. Photobiol. B Biol.* **74,** 29–38 (2004).
145. Rodriguez, V. B., Henry, S. M., Hoffman, A. S., Stayton, P. S. & Pun, S. H. Encapsulation and stabilization of indocyanine green within poly(styrene-alt-maleic anhydride) block- poly(styrene) micelles for near-infrared imaging. **13,** (2008).
146. Zheng, C. *et al.* Biomaterials Indocyanine green-loaded biodegradable tumor targeting nanoprobes for in vitro and in vivo imaging. *Biomaterials* **33,** 5603–5609 (2012).
147. London, U. of. Treatment of Primary Breast Cancer Using PDT. *NCT02872064* Available at: https://clinicaltrials.gov/ct2/show/NCT02872064.
148. Chu, Z., Zhang, S., Yin, C., Lin, G. & Li, Q. Designing nanoparticle carriers for enhanced drug efficacy in photodynamic therapy. *Biomater. Sci.* **2,** 1419–1425 (2014).
149. Gavrilov, K. & Saltzman, W. M. Therapeutic siRNA : Principles, Challenges, and Strategies. *Yale J. Biol. Med.* **85,** 187–200 (2012).